# ON THE QUANTIFICATION AND CONTROL OF INTERNAL ENERGY IN ENERGETIC RADIATION INTERACTION WITH PAHS

*A thesis submitted*
*in partial fulfillment for the degree of*

**Doctor of Philosophy**

*By*

**VINITHA M V**



**DEPARTMENT OF PHYSICS**

**INDIAN INSTITUTE OF SPACE SCIENCE AND TECHNOLOGY,**

**THIRUVANANTHAPURAM-695547**

**JUNE 2020**

*To My Mother and Father*

# CERTIFICATE

This is to certify that the thesis entitled "**On the quantification and control of internal energy in energetic radiation interaction with PAHs**" submitted by Vinitha M V, to the Indian Institute of Space Science and Technology, Thiruvananthapuram, in partial fulfillment for the award of the degree of **Doctor of Philosophy**, is a bonafide record of the research work carried out by her under my supervision. The contents of this report, in full or in parts, have not been submitted to any other Institute or University for the award of any degree or diploma.

Dr. Umesh R Kadhane
Associate Professor and Head
Department of Physics
Indian Institute of Space Science and Technology
Thiruvananthapuram-695547
Kerala, India

Place: Thiruvanathapuram
June 2020

# DECLARATION

I hereby declare that this thesis entitled "**On the quantification and control of internal energy in energetic radiation interaction with PAHs**" submitted in partial fulfillment of the Degree of "**Doctor of Philosophy**" is a record of original work carried out by me under the supervision of **Dr. Umesh R. Kadhane**, and has not formed the basis for the award of any degree, diploma, associateship, fellowship, or other titles in this or any other Institution or University of higher learning. In keeping with the ethical practice in reporting scientific information, due acknowledgments have been made wherever the findings of others have been cited.

Thiruvananthapuram

Vinitha M V

June 2020

SC16D006

# ACKNOWLEDGEMENTS

share the credit of the quantity of work I could do as part of my research with them. I always have good scientific and nonscientific chats with Gowrisankar, Supriya, Vismaya and Minnu. With Veena and Narendra Singh, I had science discussions during my PhD days. I would like to thank to Soumya, Fayaza, Anupama and Namitha for their valuable affection. Other friends from outside IIST, Surya, Sarath, Rakesh, deserves special mention. They inspired me to pursue a research career. I wish to thank few of my college teachers, Geetha Miss and Vijoy sir, Vijayan sir and Joseph sir who always been an encouragement and moral support for me to move ahead with my research carrier.

Words cannot express the gratitude to my mother whose understanding, prayers and innumerable sacrifices has made this work possible. My sister Vijitha has always been an inspiration to me, especially during the difficult phases of my research. Despite her busy schedules, she often found time to talk to me and took good care of me during these days. After all, I am indebted to the Almighty for giving me the health, wisdom and strength to pursue my passion without fail.

# TABLE OF CONTENTS

# LIST OF TABLES

# LIST OF FIGURES

# CHAPTER 1. INTRODUCTION

Evolution of the universe is closely related to the interaction of matter with radiation. The forms of matter which can survive in the harsh interstellar conditions can finally materialize as the main composition of space. Isolated carbonaceous molecules like polycyclic aromatic hydrocarbons (PAHs) have been proposed as an important component of interstellar medium (ISM)[1,2]. When an isolated molecule interacts with energetic radiations, the absorbed energy is dissipated by radiative or nonradiative relaxation mechanisms. In case of smaller molecules, energy dissipation is mainly associated with nonstatistical dissociation from repulsive electronic state. When it comes to larger molecules like PAHs, excitation energy due to UV/visible radiation
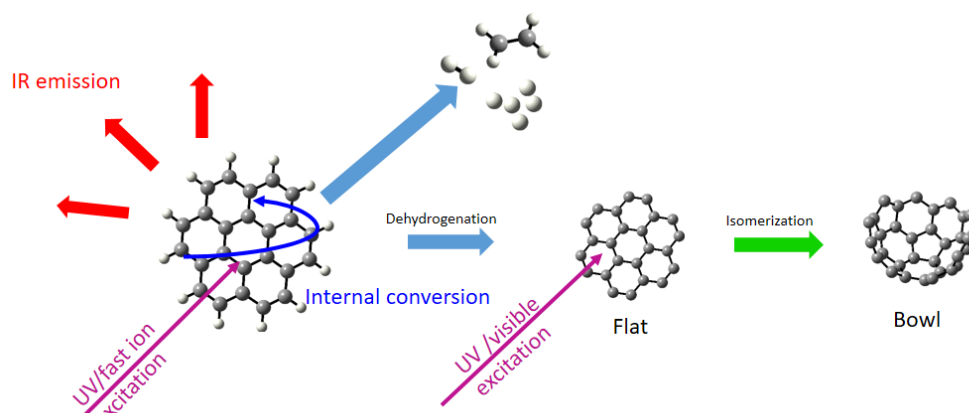


Figure 1-1: Illustration of chemical evolution of PAHs in the ISM under the influence of UV/visible photons or fast ions leading to (a) Emission of neutral molecules or (b) Complete dehydrogenation to form graphene. (c) Further electronic excitation of graphene upon UV/visible radiation interaction can lead to the formation non planar structures by the process of isomerization.

or fast charged collision is mainly stored to its rich vibrational modes, and it is digested by neutral evaporation, infrared (IR) florescence or structural rearrangements [3].

For more than thirty years, PAHs were identified as the carriers of ubiquitous IR emission bands, 3.29, 6.2, 7.7, 8.7, 11.3, and 12.7 μm associated with a wide range of interstellar environments in our local galaxy and other galaxies[1,2]. The IR fluorescence of PAHs is dominated in UV irradiated regions. It is explained by invoking strong internal conversion process, followed by rapid internal energy equilibration into various vibrational modes of PAHs resulting to IR cooling. If the internal energy is large enough, the molecule undergoes dissociations or isomerisations to form complex non-planar carbonaceous compounds in space[4] as illustrated in fig 1.1. Several laboratory studies have been devoted to address this topic.

Gas phase unimolecular dissociations are powerful laboratory tools to characterize excited electronic or vibrational state properties of the molecule. A lot of understanding about excited electronic state properties of smaller molecules in their neutral and cationic forms have already been obtained from gas phase unimolecular dissociation studies[5–8]. In case of larger molecules the energy flow from electronic to vibrational modes can be tracked with novel experimental techniques like pump probe photoelectron spectroscopy [9] and a good understanding of vibrational dynamics can be achieved by probing reaction kinetics of unimolecular dissociations. The main purpose of this work is to develop a comprehensive method to perform an investigation on statistical unimolecular dissociations of PAHs.

## 1.1    Introduction to PAHs

PAHs are intriguing quantum systems in molecular science, consisting of fused five- , six- or seven- membered carbon (C) aromatic rings with hydrogen (H) atoms located at the periphery. The simplicity of their structure reflects in the quantum states in their form of symmetry, which makes them often a model system to investigate and understand molecular quantum mechanics. As the name indicates, this family of molecules involve more than one carbon ring structure and hence, technically benzene does not qualify as PAH in spite of PAHs having most of their molecular properties common with benzene. The aromatic rings can be fused together in three ways giving three categories of PAHs namely polyaryls, ortho-fused PAHs and ortho- and para-

fused PAHs. In polyaryls, two rings are linked by a single bond (e.g. biphenyl), in ortho-fused PAHs two rings share a common C-C bond (e.g. naphthalene, azulene) and in ortho- and peri-fused PAHs three rings share a common C-C bond or a common C atom (e.g. pyrene and coronene). A schematic picture of different type of PAHs are given in figure 1.2.
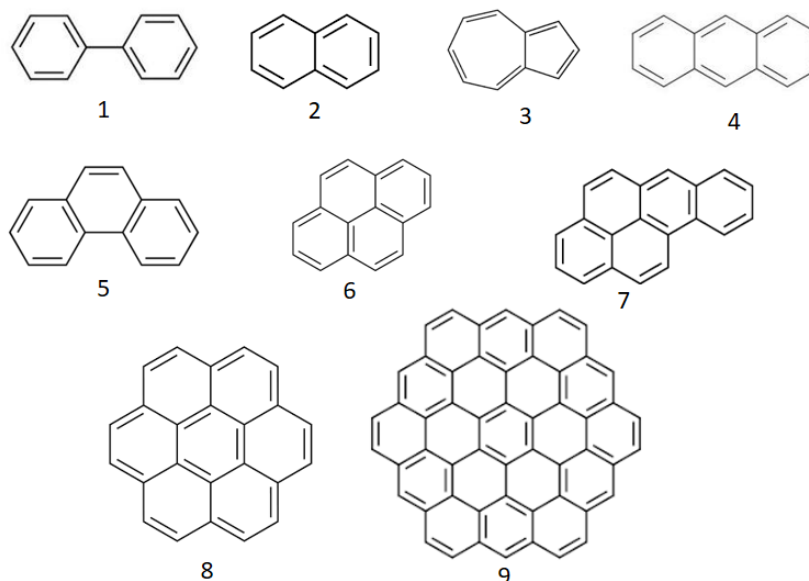


Figure 1-2: Examples of PAHs: 1) Biphenyl, 2) Naphthalene, 3) Azulene, 4) Anthracene, 5) Phenanthrene, 6) Pyrene, 7) Benzo(a) Pyrene, 8) Coronene, 9) Circumcoronene

The main feature of such a system is their high degree of electronic polarizability arising from delocalized $\pi$ and $\sigma$ electrons, which makes the system electronically resilient against harsh radiations. But, electronic delocalization is not perfect in PAHs, as is the case with benzene. The fusion of aromatic rings causes a perturbation in the delocalization of electrons of PAHs. This leads to the question of what stabilization energy comes from electronic delocalization for each of the PAHs. Huckel molecular orbital (HMO) theory is a simple, evergreen theory which can excellently give insight into the quantum behavior of hydrocarbons with delocalized electrons, aromaticity and delocalization energy etc. In simple HMO theory for pure hydrocarbons[10], *2p* atomic orbitals are linearly combined to molecular orbitals with energies given in terms of *α*, the Coulomb integral, a negative number equal in magnitude to the ionization energy of a carbon *2p*

orbital electron, and $\beta$, the resonance integral, a negative number expressing the interaction energy between two neighbouring atomic orbitals. HMO theory is based on complete neglect of multiple atom overlap integrals and is expected to yield only qualitative results. But advances in electronic structure theory, improved software and substantial improvement in computing power have made quantum structure calculations relatively easy and precise for larger molecules like PAHs. As an example, the highest occupied molecular orbitals (HOMO) of naphthalene ($C_{10}H_8$) calculated by density functional theory (DFT)[11] is shown in figure 1.3. This calculation was performed at B3LYP/6-31G(d) basis using the Gaussian09 suite[12] of programs.



Naphthalene          HOMO          HOMO-1          HOMO-2
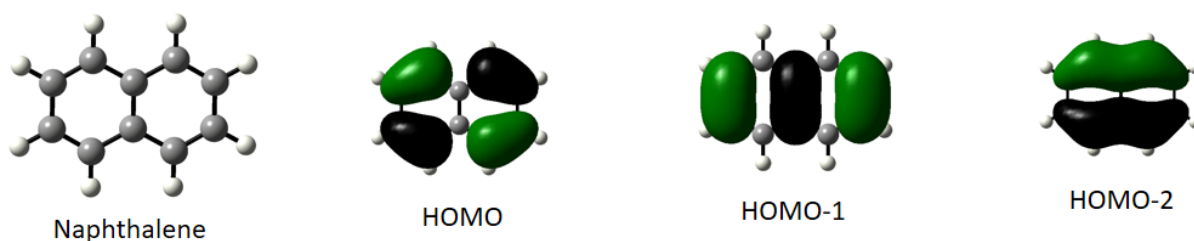
Figure 1-3: Three outermost occupied molecular orbitals of naphthalene.

## 1.2 Collective excitation in PAHs

The C-C backbone facilitates substantial delocalization of electrons in PAHs which in turn makes electron-electron correlation a very important factor in determining the quantum structure of the molecules. This gives rise to a very important and interesting phenomenon where, a molecule can have a manifold of multiparticle electronic excited states built on the ground electronic configuration. Such excitations are generally called as collective excitations. It can be understood as a phenomenon involving the simultaneous coherent motions of the loosely or less tightly bound electrons in an absorber at a frequency far above the spectrum of the single particle excitation[13]. Collective excitation is known to be associated with systems starting from nuclei to fullerene ($C_{60}$), metal clusters etc.[14]. Collective excited states were first discovered in nuclei[15] (proton-neutron oscillation) and were called giant dipole plasmon resonances (GDPR). The

4

energy of giant resonance varies from $\approx$ 2 eV in metal clusters to $\approx$20 MeV in nuclei. PAHs predominantly show two types of collective excitations, a $\pi$-$\pi$* resonance at about 7 eV and a 17 eV pi-$\sigma$* resonance, often called as plasmon resonance. Since most PAHs have their ionization potential of about 8 eV, the plasmon states are situated in the continuum and in the absence of a strong radiative decay channel, often cause autoionization in the molecule. We focus on such autoionising plasmon resonances here.

Graphite spectra are dominated by $\sigma$ and $\pi$ electron bulk plasmon at about 25eV[16]. Macromolecule, fullerenes ($C_{60}$) are basically closed hollow graphite shells, they should support plasmons nearby graphite plasmon. Using linear-response theory, Bertsch *et al*[17] have predicted the existence of giant plasmon resonance at 20eV in case of $C_{60}$. It is confirmed in fullerene molecules by photoionization experiments[18,19]. This is due to the fact that autoionization is the main relaxation channel of plasmon excitation. Interestingly, a double plasmon excitation is observed for fullerenes at about 40eV due to the excessive production of doubly charged fullerene parent ion in multiphoton ionization experiments[19]. The single and multiplasmon resonance in $C_{60}$ have also been observed in fast ion collisions and it is confirmed by plasmon model calculations[20,21]. In case of several PAHs, Ling. Y *et al*[22] have observed, first order plasmon resonance at about 17eV in the photoionization efficiency (PIE) curve as shown in figure 1.4, which is a similar phenomenon to the one observed for $C_{60}$. But the potential of higher order plasmon resonance is not investigated in case of PAHs.

Mishra *et al*[23] have observed that plasmon excitation in PAHs is strongly coupled to inner valence electrons, resulting in the emission of an electron with negligible kinetic energy. This process produces PAH$^+$ in excited electronic states, which will rearrange to ground electronic state on an ultrafast timescale by transferring energy from electronic degrees of freedom to nuclear ones. The ionization potential of PAHs is about 7-8eV, Therefore, PAH$^+$ are produced at higher and a localised internal energy (say 8-9 eV) as result of plasmon excitation. Internally excited PAH$^+$ can either undergo statistical thermal rearrangement or dissociation processes in extended time scales depending on the dissociation and isomerization barrier energies. It is now believed that ionized and dehydrogenated PAHs are responsible for various spectroscopic astrophysical observations. Therefore, it is of great interest to study ionization, fragmentation and isomerization processes in PAHs following plasmon excitation. One of the major objectives of

this work is to study statistical dissociation of $PAH^+$ produced by potential collective resonances excited upon collisional interaction with energetic radiations.
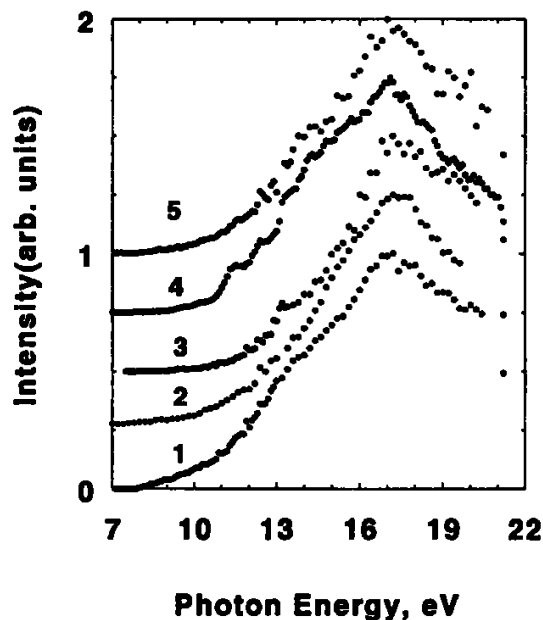


Figure 1-4: PIEs of (1) Phenanthrene, (2) Anthracene, (3) Fluoranthene, (4) Pyrene and (5) triphenylene without mass selection, in the photon energy range 7.0-21.2 eV range (showing plasmon resonance at about 17eV), as observed by Ling. Y *et al*[22]. Y axis is offset for individual molecules for clarity.

## 1.3      Unimolecular dissociations in PAHs

The dissociation of molecules is one of the fundamental processes in nature. The kinetics and dynamics of unimolecular dissociations are therefore of considerable interest in different fields like molecular science, biology, astronomy and environmental studies etc. Unimolecular dissociation can be broadly divided into two types, namely, statistical dissociation and non-statistical dissociation. Statistical dissociation is normally observed for large molecules particularly for aromatic hydrocarbons. They prefer an ultrafast electronic relaxation to long lived low lying electronic states after electronic excitations. This process is called internal conversion (IC). IC is followed by rapid equilibration of the excess internal energy among various vibrational modes of the molecule. This process is known as intravibrational energy redistribution (IVR). If

6

the available internal energy is higher than dissociation thresholds, molecule can open statistical dissociation channels. The rate of statistical dissociation is proportional to the number of microstates accessible to the molecule and it changes rapidly for a small shift in internal energy.

Smaller molecules prefer non-statistical dissociation. Their low lying electronic states are not usually bound states. Hence, there can be no vibrational coupling between low lying and high lying electronic states. Therefore, after electronic excitations, the evolution of electronic states cannot be expected for smaller molecules. So the only way to eliminate the electronic energy, which is absorbed by simple molecules is to undergo ultrafast dissociations from excited electronic state. This is known as non-statistical dissociations. Many heterocyclic ring molecules often follow non-statistical dissociation channels, because some of their low lying intermediate electronic states are dissociative in nature. Hence, they are less coupled to bound electronic states. Therefore, statistical and non-statistical dissociations are equally possible for such molecules. Several biomolecules belong to this category.
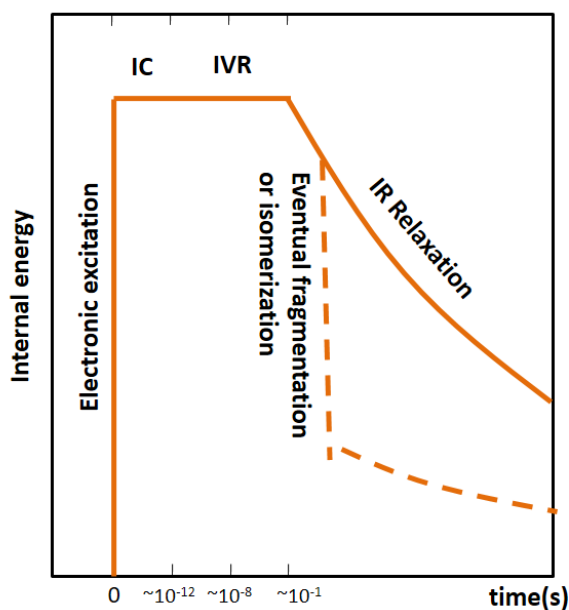


Figure 1-5: Schematic view of internal energy balance in a PAH molecule.

As mentioned earlier, PAHs mainly disintegrate by statistical dissociations. A theoretical description of dissociation of isolated PAH/PAH ions have already been given by many authors[24–28]. The unimolecular dissociation of PAHs includes four steps: 1) electronic excitation by interacting with high energy radiations like UV or fast ions, 2) IC, the absorbed energy being transferred from the electronic degrees of freedom to the nuclear ones, while the system recovers, at constant energy, in its low lying or ground electronic states, 3) IVR of the available energy among all vibrational states and either 4a) energy dissipation by IR emissions or 4b) isomerization/dissociation if available energy is above their thresholds. The eventual dissociations of PAHs/PAH ions have become an important topic in many investigations. PAHs/PAH ions disintegrate by eliminating H, $H_2$/2H or $C_2H_2$ particles. These steps are illustrated in the figure 1.5. In the first step, the energy is absorbed in the electronic degrees of freedom. The absorbed energy is transferred and redistributed to various vibrational modes of low lying electronic states in picosecond (ps) timescales in the subsequent two steps. If the energy is sufficiently large, the molecule will either evaporate atoms or molecules, or rearrange to different conformers in microsecond timescales.
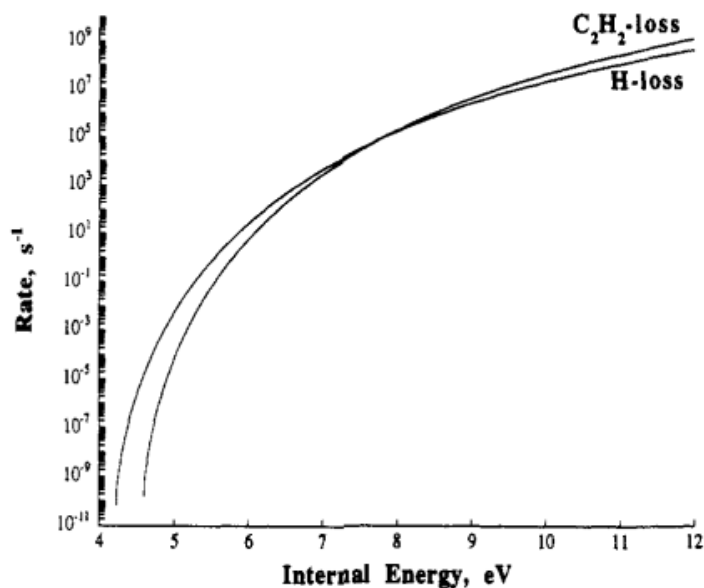


Figure 1-6: Rate constants of H loss and $C_2H_2$ loss of naphthalene$^+$ for a wide range of internal energies as calculated by Gotkis $et\ al$[27].

A complete simulation of each of the four steps described above is usually avoided by taking advantage of ultrafast IC to ground electronic states. Finally, it can be safely assumed that molecule explores the ground-state potential energy surface with an increase in internal energy, and may reach dissociative or isomerization channels. Therefore, dissociation rate-energy curve of PAHs is of considerable value in fundamental molecular science and astrophysics. A typical H loss and $C_2H_2$ loss rate-energy curve of naphthalene cation is given in figure 1.6. In this graph there is a specific energy window in which the dissociation process becomes too slow compared to IR emission. This allows one to establish the critical point energy of PAHs, which plays a crucial role in ascertaining the PAH size distribution for a particular astrophysical conditions. Moreover, the quantification of reaction kinetics of PAH dissociations helps to comprehend the molecular dynamics and progression of organic molecules in the universe. One of the few obvious methods to perform such measurements is with cations of PAHs, whereby the target molecule can be easily manipulated and detected experimentally. Several theoretical attempts have already been made to calculate the statistical dissociation parameters of simpler PAHs such as naphthalene$^+$ from the *ab initio* simulations[27–30]. These efforts cannot be applied to larger PAHs, because the computations become cumbersome due to complicated potential energy hypersurfaces. In this context, experimental measurements are of particular interest with which dissociation kinetics of larger PAHs can be targeted. A brief review on presently available experimental methodologies are given the next section.

## 1.4        Experimental methodologies to measure unimolecular dissociation

Handling neutral molecules, experimentally, is obviously a challenging endeavor. Physicist often prefer using ions instead. Particularly for the molecules like PAHs the structural changes from neutral to mono cation or mono anion can safely be ignored. Thus, the cationic form of PAHs brings in convenience of manipulations using electromagnetic fields and detection using standard single particle radiation detectors like channel electron multipliers (CEM) or micro channel plate detectors (MCP). Study of unimolecular dissociation requires one additional step in which the ions needed to be produced with specific internal energy. Molecular ions can be prepared by a number of well-established conventional techniques, and then heating can be achieved by collision activation or photoexcitations with a tunable laser. Experimentally, the ionization process itself brings out complications like the determination of residual internal

energy after ionization, formation of multiple conformations of the parent ion etc. Therefore, it is always desirable to produce the parent ion with negligible internal energy before subjecting it to a heating process[29–31]. A single VUV photoionization in combination with photoelectron spectroscopy is a commonly employed and physically adequate technique to investigate the dissociation process of PAH ions as a function of internal energy[25]. But it requires access to large synchrotron radiation source facilities and demands prohibitively low event rate to counteract false coincidences in the data. The time dependent evolution of molecular ion on longer time scales cannot be targeted with such weak signals. Therefore, a more comprehensive and efficient method needs to be developed to produce an ensemble of PAH ions at known and narrow internal energy distributions. One such method is demonstrated in this work.
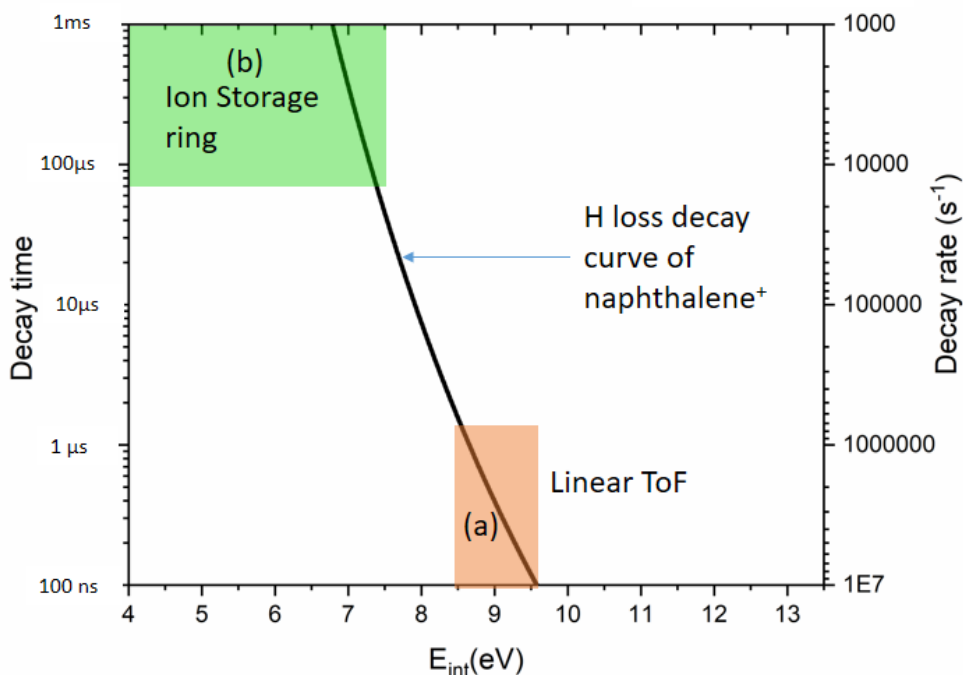


Figure 1-7: The time window accessible for (a) typical linear ToF spectrometer and (b) ion storage ring is demonstrated for H loss process of naphthalene[+]

The second stage of the experiment is the measurement of dissociation timescale of molecular ions in appropriate timescales. For this, molecular ions with known internal energy needs to be probed using standard facilities like time of flight (ToF) technique, ion storage rings or ion traps. In the former case, the available time window for detectable decay is usually limited

to first few microsecond (μs) and in later cases the decay mechanism can only be probed after tens of μs due to extraction uncertainties or orbit time period and moreover, the identity of the decay channel will be ambiguous in this techniques. The dissociation rate of H loss or $C_2H_2$ loss channels of PAHs varies in several orders of magnitude for a small shift in internal energy[27,28]. Therefore, a complete evolution of dissociation rates of PAHs for a wide range of internal energies cannot be measured using a single technique as shown in the case of the H loss dissociation channel of naphthalene[+] (see figure 1.7). Thus, a spectrometer covering a wide and continuous range of time scales, typically from few nanosecond (ns) to hundreds of μs will be most suitable to track dissociation process of PAHs. The high-resolution energy-ToF spectrometer technique, developed as part of this research can serve this purpose.

In summary, the timescale of statistical dissociation of molecular ion is strongly related to internal energy. Considering the fact that PAHs have a strong tendency for nonradiative settlement in the long lived lower electronic state via rapid IC after interacting with energetic radiations, a hot ensemble of PAH ions can easily be produced in the harsh conditions of ISM. This hot ensemble is a very interesting quantum system and needed to be observed in a suitable time window to be able to assess the quantum behavior of the system. This necessitates an investigation of dissociations on tens of μs and this has to be supplemented by a quantified energy transfer to the molecule. This thesis work is mainly exploring some unconventional aspects of internal energy quantification and measurements of statistical dissociation of PAHs on extended timescales.

# CHAPTER 2. EXPERIMENTAL SET UP AND INSTRUMENTATION

The investigations of ion-molecule or photon-molecule interactions are usually carried out using various mass analysers such as quadrupole or ToF mass analyzers. The main purpose of mass analyzers is the identification of fragment or intact ions and their relative contribution to the overall decay of the molecular ion in radiation interactions. When it comes to fundamental information like ionization or fragmentation states, we have to use recoil ion momentum spectroscopy so that complete kinematics of the fragmentation processes will be obtained[32,33]. These types of measurements are only effective for smaller molecules like $N_2$ and $O_2$, as they show larger momentum spreads due to fragmentation as compared to thermal momentum distributions. On the other hand, momentum distributions due to fragmentation of large molecules are comparable to the thermal effect, so it is difficult to assess the electronic states of reactant ion by recoil ion momentum spectroscopy. Moreover, large molecules often prefer statistical decays, spread over ns or longer timescales. It can be explored using electrostatic spectrometer configurations which employs timing analysis. ToF mass spectrometer is one such technique, which does mass analysis on the basis of ToF measurement. ToF spectrum is sensitive to the dissociation process happening in the extraction or acceleration regions of the spectrometer. Therefore, molecular dissociation occurring in the first few μs can be measured using standard ToF technique.

Time correlated mass spectroscopy is at the heart of all investigations carried out in this work. We have utilized and modified various features of ToF mass spectrometer in order to perform an extensive investigation on statistical dissociation of PAH ions produced by fast proton beam and ns second UV lasers. Proton induced dissociation of PAHs is investigated using a

standard two field ToF mass spectrometer. The details of the experimental setup is described in this chapter. As part of this thesis work, an energy correlated ToF mass spectrometer has also been developed with which molecular dissociations as slow as few millisecond (ms) timescales can be targeted. Details of the instrument are elaborated in this chapter.

## 2.1          Linear ToF mass spectrometer

A linear ToF mass spectrometer is one of the simpler mass analyzers in use. Its geometry usually consists of two electric field regions. The ions are usually produced in the first electric field region called the extraction region (ER) and they are extracted to the acceleration region (AR) wherein they are accelerated to a maximum energy towards the field free drift tube (FD). The ions with same mass to charge ratio ($m/q$) will drift inside FD region at a constant velocity to a distant detector kept at the drift tube exit. Hence, ions with similar $m/q$ will reach the detector at the same time. If the ion beam is pulsed, the time zero can be taken from the master clock for the pulsing system. A continuous beam can also be employed if an alternate start signal is obtained, for example, from the detection of associated outgoing electrons which takes very short time to reach their detector. The recoil ion detector is commonly CEM or MCP, and is capable of sub-nanosecond timing accuracy. Schematics of a two field linear ToF spectrometer and a typical ToF spectrum of Ar gas measured under proton impact are shown in figure 2.1 and figure 2.2, respectively. The overall time and hence, mass resolution is governed by various factors including, the timing inaccuracies due to electronics, thermal velocity spread of the target molecules, the relative volume of interaction *vis-à-vis* length of the ER, etc. A well-known two field configuration proposed by Wiley and McLaren[34] is commonly used to improve the mass resolution. This arrangement employs first order velocity and time focusing to compensate for the thermal spread and finite interaction volume. Often this is supplemented by either cooling the target using pulsed valve and supersonic jet expansion or by introducing the target in the reaction volume using a very large length to diameter nozzle/needle. The radiation beam size is also regulated to smallest possible diameter in order to reduce the size of the interaction volume.
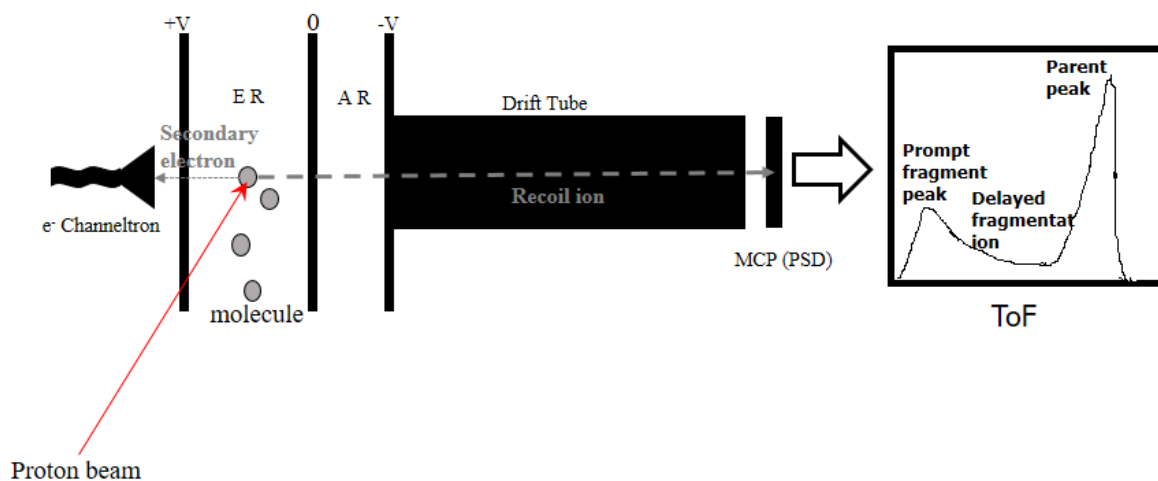
Figure 2-1: Schematics of linear ToF mass spectrometer, ToF spectrum illustrating distorted fragment peak due to delayed fragmentation is shown at the right end.
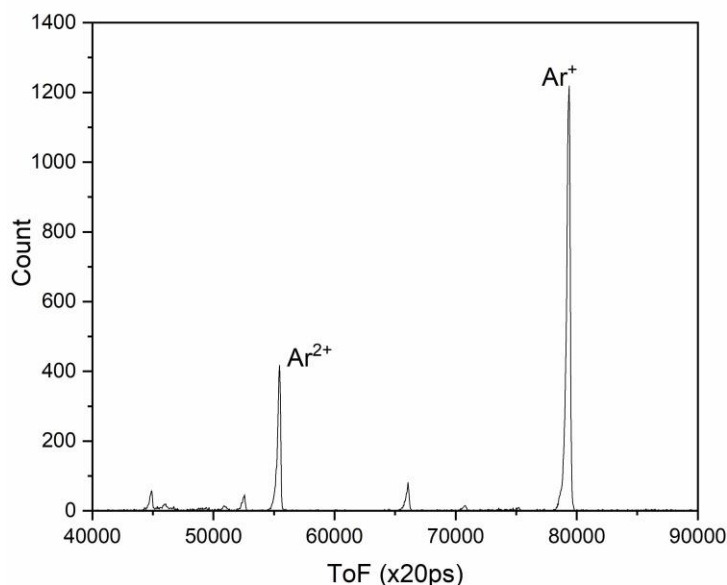


Figure 2-2: ToF spectrum of Ar gas measured under proton impact

In addition to mass analysis, ToF techniques have been intensely utilized in the past to study dynamics and kinetics of molecular dissociation. The study of dissociation dynamics is of considerable interest for small molecules. It is accomplished by combining the time information with the relative position of the recoil ions at the end of the drift tube. It helps to explore potential

energy curves/surfaces of higher electronic state from which dissociation would have occurred. Whereas, dissociation kinetics are very important to understand molecular dynamics of large molecules, especially for PAHs, because they often dissociate from ground or low lying bound electronic states by the advent of rapid IC (details are given in sec 1.3 of chapter 1). Therefore, the internal energy dependence of molecular dissociation is very useful to explore potential energy surface of ground electronic state of PAHs. It is noteworthy that fragments produced at the instant of ionization, for example: fragmentation by non-statistical channels, will be accelerated to maximum energies and appear as a clear and distinct peak at their right mass in ToF spectrum. Therefore, such fragment peaks are known as prompt fragment peaks. Whereas certain fragment peak in the ToF spectrum shows a tail extending from the prompt position (as illustrated in the ToF spectrum of figure 2.1). This is due to delayed dissociation in ER and AR of the spectrometer and the corresponding fragment ion is accelerated to lower kinetic energies and hence, lower velocities compared to prompt fragments. Such fragments arrive at the detector late and develop a tail to the prompt peak. This tail is useful to evaluate rate constants of such dissociations. It will be typically of the order of $10^7$-$10^5 s^{-1}$. Whereas the fraction of fragment signals detected by a standard ToF technique from slow dissociations (with decay rate $10^5$-$10^3 s^{-1}$) is usually very weak. Ample fragment signal from slow dissociations ($10^5$-$10^4 s^{-1}$) can be targeted using reflectron ToF[35]. This technique is usually employed to increase resolution in a ToF mass spectrometer in which a reflecting electrostatic field is employed at the end of the drift region to achieve second order energy correction. Measurements of slow dissociations can be performed with a reflectron ToF apparatus operating with partial correction, rather than for complete or no correction for the kinetic energy shifts of the daughter ions. In this work, we have developed a high resolution energy-ToF spectrometer, with much more refined electric field provided by a parallel plate analyzer, kept at $45^o$ to the drift tube end. This technique offers a high resolution energy analysis of incoming fragment ion in addition to its ToF measurement. Therefore, it helps to expand the observability of a standard ToF spectrometer from higher dissociations ($10^7 s^{-1}$) to lower dissociations ($10^3 s^{-1}$). The basic design of this instrument is adopted from the ion-neutral coincidence spectrometer, established at laboratory of Atomic and Molecular Collisions, University Paris-Sud XI[36,37].

## 2.2 Parallel plate energy analyser (PPA)

Parallel plate energy analyzer is a simpler electrostatic energy analyzer used to perform energy analysis of an incoming ion beam. It is designed based on fields in which particles are first retarded and then re-accelerated. A uniform field is created in PPA by applying a potential difference across a pair of plane parallel plates, as shown in figure 2.3. The particles enter the analyzer at an angle $\theta$ with respect to the entrance electrode and follow a parabolic trajectory inside the analyzer due to the electric field. The pass energy of PPA, $E/q$ is determined by the voltage difference between the electrodes divided by the geometrical constant $c$ of the analyzer

$$\frac{E}{q} = \frac{\Delta V}{c} \tag{2.1}$$

$$\text{Where, } c = \frac{8d \sin\theta (\cos\theta)^3}{R} \tag{2.2}$$

When the entrance angle of entering particles is 45°, first order focusing can be obtained in the plane of deflection as shown in figure 2.3(a)[38,39]. In that case, $d_1=0$ (as defined in eq. 2.3), *i.e.* entrance and exit slits are located in the single entrance plate. A second order focusing in the dispersion plane can be obtained for $\theta = 30^o$ [39]. In that case, $d_1 \neq 0$ and the entrance and exit slits are placed in a field free region as shown in figure 2.3(b), where both the bottom plates, entrance and exit slits are held at same potential. One drawback of a PPA is that the angular focusing only occurs in the plane of deflection (x-z plane of figure 2.2) and not in the perpendicular ($y$) direction. A point at the entrance slit is imaged as a line along the y-direction.

$$\text{Where } d_1 = \frac{L}{4} \frac{cos(2\theta) \, sin(\theta)}{(cos\,\theta)^3} \tag{2.3}$$

The energy spread of PPA is given by equation (2.4). The energy resolution is maximum for $\theta = 45^o$. The entrance angle optimized for our PPA design is 45°, which gives better energy resolution and reasonably good focusing conditions. The details of the PPA design are given in sec 2.5.1.3.
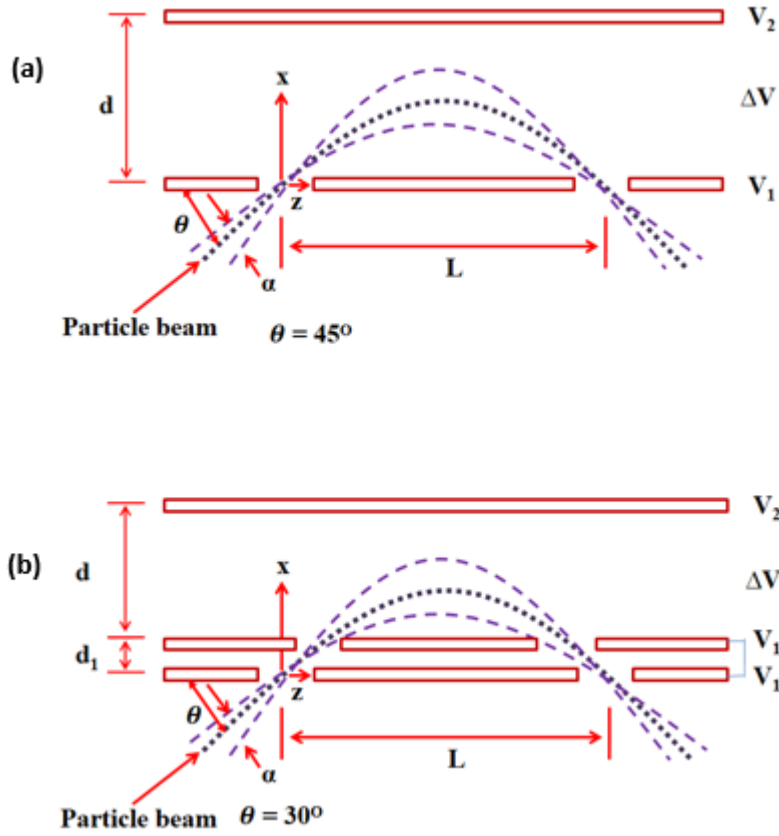
Figure 2-3: Diagrams of parallel plate analyzers at a) $\theta = 45^o$ or b) $\theta = 30^o$

$$dE \propto \cos(2\theta) \ d\theta \tag{2.4}$$

The maximum distance, $x_m$ that the beam enters the analyzer (in the x-direction) is given by the following equation,

$$x_m = d_1 + \frac{L \sin(\theta + \alpha)}{8(\cos(\theta + \alpha))^3} \tag{2.5}$$

$x_m$ is calculated to make sure that the beam does not hit the outer electrode. For $\theta = 45^0$, $x_m \approx \frac{L}{4}$.
Therefore, a plate separation of $d > \frac{L}{4}$ should be adequate.

17

## 2.3    Electron and ion detectors:

Detection of single particle has been important since the beginning of nuclear and atomic physics. Rutherford's alpha scattering experiment, cloud chamber, etc. are just a few examples. With the advancement of material science, it has become possible to enhance or amplify a single ion or an electron signal by a large gain of $10^6$ and hence convert it into an electrical signal which can then be processed by suitable electronics. Photomultipliers, CEM and MCP are few examples of such detectors. CEM or MCP are commonly used as electron or ion detectors of ToF mass spectrometers. Their basic working principle is explained in this section.

### 2.3.1    CEM

The CEM can be used to detect incoming ions or electrons and sometimes photons. As the particle strikes on the conical surface of the channeltron, it produces few secondary electrons as shown in figure 2.4. These electrons are accelerated toward the tail and strike the channel wall to produce few more electrons. It continues until it reaches the tail of the detector with a pulse of $\approx 10^6$ electrons. The potential difference between the cone and the tail of CEM is usually kept around 2kV, the cone voltage polarity is decided by the charge of incoming particle and the tail polarity is always kept positive with respect to the cone in order to drive the electron through. In this work, the CEM signals were employed to perform multicoincidence measurement in proton impact experiments.
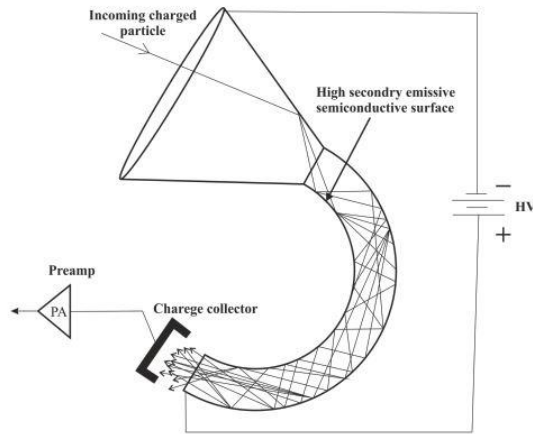
Figure 2-4: Schematics of a channel electron multiplier

*2.3.2*     MCP detector with Delay line anode (DLA)

The MCP is also commonly used to detect ions or electrons. It can handle higher count rate and has better timing resolution compared to CEM. MCP detector is a disk shaped with several numbers of micrometer sized diameter holes arranged like an array with individual hole is an electron multiplier. When a particle hits on the detector, each channel gives rise to an avalanche of electrons leading to an electron cloud at the back. Moreover, with the help of a Phosphor screen and CCD camera, a Wedge and strip anode or with DLA, one can measure the position of the ion impact on the MCP. This forms the basis of technique of Recoil ion Momentum Spectroscopy. MCP with DLA are used for position and time measurement of recoil ions produced in proton and photon impact experiments performed in this work. MCP with DLA (ROENTDEK model DLD 40) is a high resolution 2D-imaging and timing device for charged particle or photon detection at high rates with multi-hit capability. The linear active diameter is at least 40 mm. It consists of a pair of resistance matched (within 10 %) rimless MCPs in chevron (two MCPs mounted one top of each other) configuration, supported by a pair of partially metallized ceramic rings (1.5 mm thick, 65 mm outer diameter.) and a 2D-position sensitive DLA (helical wire pair). The detector operation requires two DC voltages for MCP front and back contacts and three voltages for anode body ("holder") and the helical wires. The details of the structure are shown in figure 2.5.
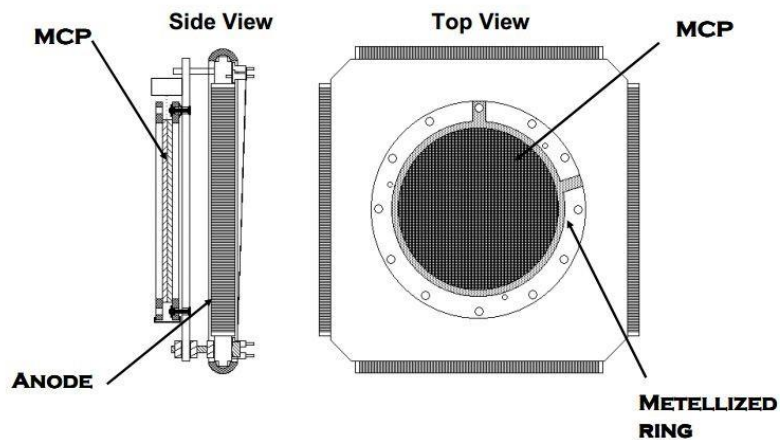
Figure 2-5: Schematics of MCP with DLA, figure adapted from Roentdeck DLD40 manual[40,41]

**Operation of DLA to perform position encoding:** Electron cloud from the MCP induces a differential signal on each delay line pair that propagates to the delay line ends where it is picked up by a fast differential preamplifier. By measuring the difference between the signal arrival times on both ends of the delay line, one can determine the position of ion impact in both *x* and *y* directions. Signal propagation time on the delay line is about 0.71 ns/mm. The sum of these

arrival times is constant for each event. Hence it can be used as an additional check for cleaning the data.
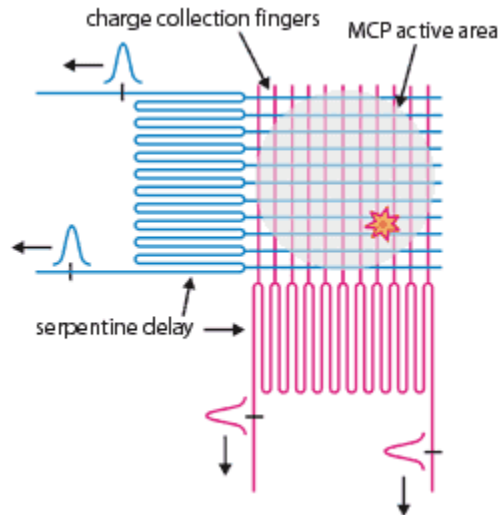


Figure 2-6: Schematics of DLA, adapted from Roentdek DLD40 manual[40,41].

2.3.3    Pulse processing and data acquisition system (DAQ)

A typical detector signal is shown in figure 2.7 (a). It is a very weak and fast pulse with an average pulse height of 2-10 mV and pulse width about 10ns. It cannot be transferred with a standard connectors and cables, has to be treated like an RF pulse. Therefore, very specialized cables are used in this experiments (RG 58 or RG 188 cables, both have 50 ohm resistance independent of its length[42]). This signal has to be checked with an oscilloscope, which should have a band width of at least about 200MHz and an input impedance of 50 ohm. The detector pulse is amplified with a timing amplifier which has a band width of a few GHz. Output signal of the amplifier will be typically about 100mV.
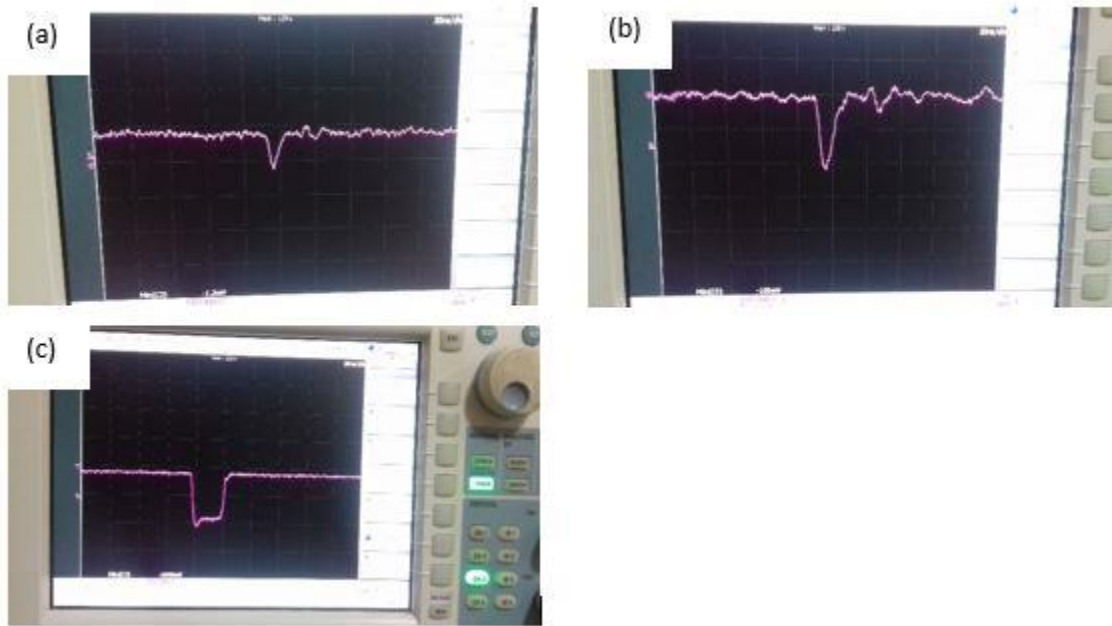
Figure 2-7: (a) A typical analogue signal from the detector, (b) Amplified signal, (c) NIM signal from CFD.

The detector signal is an analogue pulse, which can have variable amplitude depending on the impact position and nature of the source particle. Since our demand for time resolution is very high, we cannot use this pulse for time reference unless maxima or minima of the pulse is found. Therefore, all the detector signals are fed to independent constant fraction discriminator (CFD). This device electronically takes derivative of the pulse and finds zero, that will be maxima or minima of the analogue pulse and delivers negative logic pulse (NIM pulse) for time reference. The problem with CFD is that it will produce NIM signal for noise pulse also. So we must set a threshold in the CFD so that it will not generate a faithful time reference for noise pulses. Pulse width of the NIM signal is usually few tens of ns otherwise it may miss other delay line signals. This NIM pulses can be set to trigger on rising edge or falling edge.

Time difference between detector signal and reference signal is measured by time to digital converter (TDC). In some experiments signal and reference pulses are issued by two separate detectors. If reference pulse starts (stops) data acquisition, which is termed as common start (stop) mode. Depending on the mismatch between count rates of start and stop signal we

can choose mode of data acquisition. In proton beam experiment, the data is acquired in common stop mode due to very high count rate (>1kHz) of electron trigger. But, in laser experiment (in which master trigger of pulsed laser was the timing reference to TDC), we have chosen common start mode for data acquisition due to very low repetition rate (100Hz) of laser pulse. These TDC can count signal for indefinite time once it is triggered, there will be a time window of interest for every measurement. We can set a veto window, which can suitably be adjusted to cover useful time window of interest. This way it helps to keep useful information in first hit itself. For example, if we are using high voltage pulsing, then first few μs of the data will be high voltage noise pick up, which cannot be separated. In this case, first and second hit will only contain noise. In these circumstances setting a veto window to exclude noise pick up becomes very important. Veto is also used to avoid unwanted mass peaks to be recorded, reducing the data size to only useful data. The minimum time difference a TDC can measure with respect to a reference is the resolution of TDC, which is typically few tens of ps. TDC also needs minimum time to resolve two consecutive signals on the same channel, which is termed as pulse pair resolution. It is normally of the order of 10ns. Pulse pair resolution of TDC is decided by how rapidly timing pulses are generated and how fast it can be recorded by TDC. If more than one detector pulse is recorded on the same channel in the same event, then it is termed as multihit event. Finally the data is recorded in compressed format which is called as list mode.

## 2.4    Experimental arrangements for proton-PAH interactions

The proton collision experiment were carried out at the Low Energy Ion Beam Facility, Inter University Accelerator Centre, New Delhi, using an electron cyclotron resonance (ECR) ion source mounted on a high voltage deck. Proton beam (50, 75, 100, 125, 150 and 200 keV) were made to collide with PAH and nitrogen containing PAH (PANHs) isomer targets (azulene ($C_{10}H_8$), naphthalene ($C_{10}H_8$), quinoline ($C_9H_7N$) and isoquinoline ($C_9H_7N$). Target molecules were effusing from a needle placed perpendicular to the projectile beam path in the collision chamber. The base pressure of this chamber is maintained at $2 \times 10^{-8}$ Torr and was allowed to increase to a maximum of $2.6 \times 10^{-7}$ Torr with the gas load to achieve the single-collision condition. Target samples were obtained from Sigma Aldrich with 98 % purity. Since the vapor pressure of these targets are very high at room temperature, no heating was required for evaporation.

## 2.4.1    Experimental set up

A double field ToF mass spectrometer with a position sensitive MCP detector was employed for the detection of the recoil ion[43,44]. The ToF spectrometer, proton beam and a needle (effusing gas) were mutually perpendicular to each other. To avoid cross-contamination between the two isomeric target PAHs, a third molecule was introduced in the chamber between the study of two targets and its interaction with the proton beam is investigated. The schematics of the experimental setup is shown in figure 2.8. The ejected electrons from the interaction of the target with the proton beam were detected using a CEM that was kept below the interaction region. The neutralized projectile was detected by an alternate CEM, kept along the projectile path. Projectile ions were deflected away from this detector using an electrostatic deflector. The CEM for detecting the projectile is mounted in a small, well shielded box which has a rectangular slit of 1 mm opening. This box is attached up on a translational feedthrough which, makes the detector move in and out, *i.e.*, towards or away from the beam path.
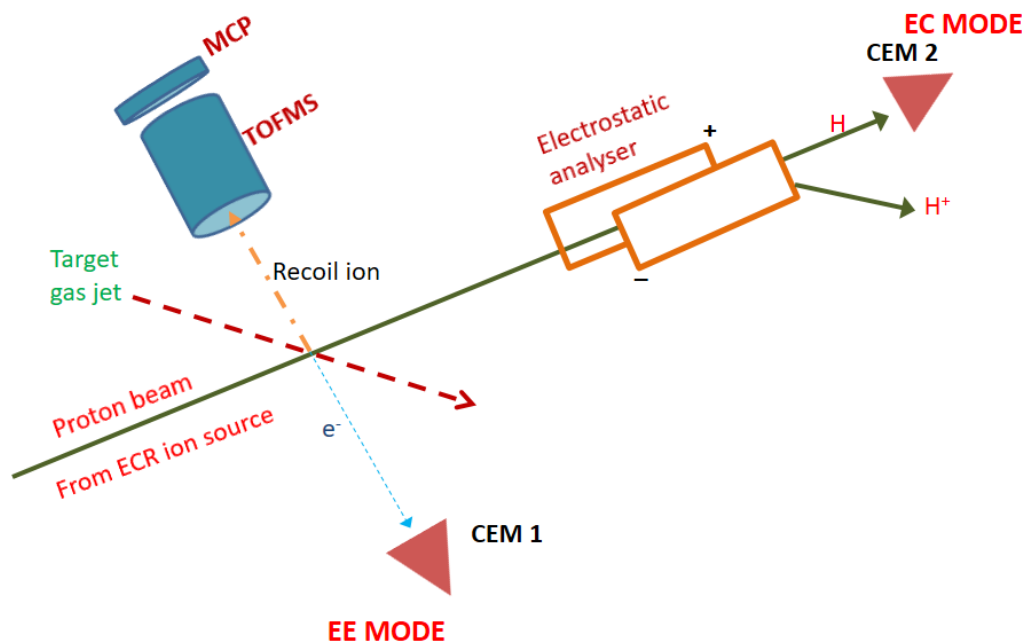


Figure 2-8:  Schematics of experimental setup.

24

### 2.4.1.1    Electron Cyclotron Resonance (ECR) ion source

Kiloelectron volt proton beam used in this experiment was produced from a Nanogan type ECR ion source, which is based on a fully permanent magnet design for radial and axial confinement of the plasma. ECR ion source can be described as a plasma reservoir for electrons, neutral atoms and ions, and the production of highly charged ions in it essentially occurs in a sequence of ionization steps caused by electron impact. The power from a 10 GHz ultra high frequency (UHF) travelling wave tube (TWT) amplifier is transmitted to the source through a rectangular wave guide and coupled to the plasma using co-axial coupling. The principle of ECR ion source operation has been described in great detail in the book by Geller[45]. Tuning the ion source parameters like gas pressure, microwave power, magnetic field strength, etc. vary the charge state distribution within the plasma. In the present case magnetic field can not be varied due to the permanent magnet design. When electrons leave the plasma through the loss cone of the magnetic mirror, ions can follow and were extracted by applying a maximum voltage of +30 kV between the ECR ion source and the extraction electrode. The ECR ion source, along with all its peripheral electronics, UHF transmitter and vacuum components placed on a 200 kV high voltage (HV) platform, can provide multiply charged positive ions with energies ranging from a few keV to a few MeV.

### 2.4.1.2    Electronics for data acquisition

As the proton beam interacts with a target molecule, it can cause ionization by electron emission or by electron capture from the molecule. The ejected electron and neutralized projectile signals are used as timing reference in OR mode for ToF measurement of recoil ions. Data is acquired in common stop mode. Figure.2.9 explains the electronic setup of the position-sensitive multihit detector system. The timing signals from each of the two ends of both the delay lines are taken to a differential amplifier. MCP front signal and projectile/electron CEM signal are taken to a fast timing amplifier. The amplified signals are then fed to CFD to discriminate the true signals from noise. The CFD gives fast NIM signals which are then fed to NIM to ECL convertor. This was necessary because the TDC used here could only take ECL inputs. The fast ECL outputs are taken to a TDC to start the data acquisition. A copy of projectile/electron NIM pulses from CFD are delayed (typically for 10μs) and taken to logical OR gate and its output is fed to TDC,

as a stop trigger. The TDC has a minimum timing resolution of 25 ps, with multihit pulse pair resolution of 10 ns. If ToF and position of recoil ions are measured with respect to electron signal, it is termed as electron emission mode. If ToF and position of recoil ions are measured with respect to neutralized projectile signal, it is called electron capture mode. Selective delays are added in the stop signals to give priority to the neutralized projectile for common stop. Electron signal detected along with neutralized projectile stop was used to study capture ionization mode. Data from the TDC is collected in list mode through a CAMAC crate controller and PCI-based I/O card to a computer. The data acquisition program is written in C language on Linux operating system. The data acquired is converted directly into ROOT specific format which could be used for calibration and preliminary analyses. Thus, we can check the events as they arrive.
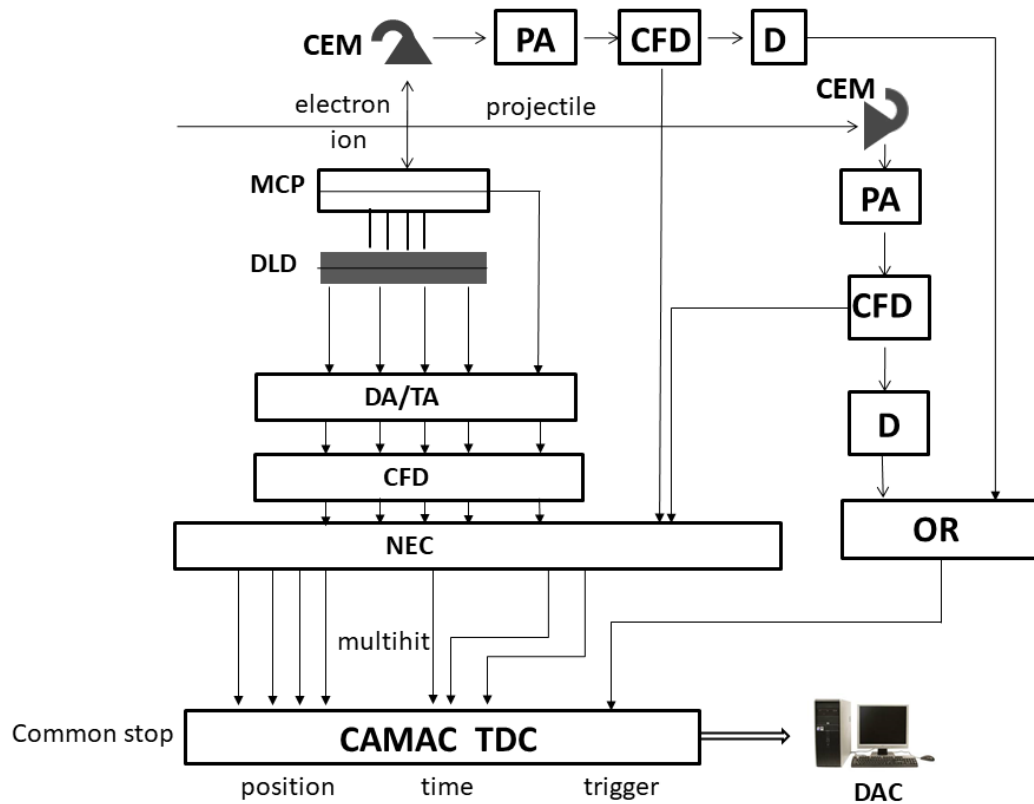


Figure 2-9 : Electronic setup of the position-sensitive detector system. The different short forms mean the following. DA: differential amplifier, CFD: constant fraction discriminator, TA: timing amplifier, PA: preamplifier, D: delay, NEC: NIM–ECL converter.

**2.5     Development of high resolution Energy-ToF spectrometer technique**

A high resolution energy - ToF spectrometer is developed to probe the dissociation time scales of PAHs in Atomic and Molecular Physics Laboratory, Indian Institute of Space Science and Technology. PAH cations are produced by allowing gas phase molecules to interact with low energy ns UV laser pulses. Various stages of the developmental work, full performance and unique capability of this new technique is explained in the following sections.

2.5.1     Experimental set up

3D schematics of the spectrometer is shown in figure 2.10. It consists of ER, AR, FD, PPA and position sensitive MCP detectors. The details of each section are described below.
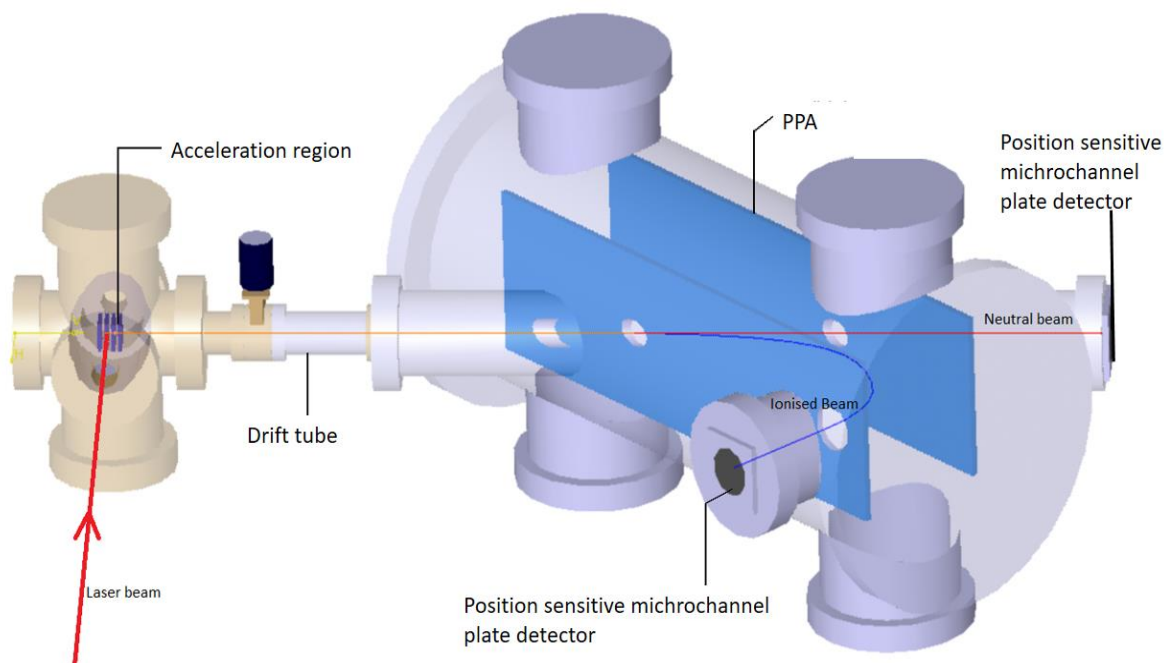


Figure 2-10: 3D schematics of high resolution energy-ToF spectrometer

2.5.1.1    Extraction region (ER) and acceleration region (AR)

Two electric field sections are employed to extract and accelerate ions. It is built using three metal plates of 3 mm thickness separated by 7 mm each. The first plate is biased to +3 kV, followed by +2.45 kV on the second plate and the last plate is at ground potential. Initially, the alignment between metallic plates was not precisely parallel and hole size was more than 1mm. It badly affected energy and ToF resolution. Hence a better hardware is built by precise machining. A hole of size, 0.7 mm is made on each of the plates and carefully aligned to get uniform field, precise alignment and narrow extraction from the interaction point. This way we could achieve very high ToF and energy resolution. Neutral PAH target vapor is allowed to effuse into the extraction region through a small nozzle (with the length to diameter ratio >50) at room temperature. The base pressure of the interaction chamber is maintained at $5 \times 10^{-8}$ mbar and is allowed to increase to a maximum of $9 \times 10^{-8}$ mbar with the gas load in order to minimize the interaction of multiple particle with a single laser pulse. A nanosecond pulsed laser is focused near to the first plate, which is at +3 kV (2 mm away from the plate), using a lens of focal length 30 cm. The focal point was very accurately aligned with the line of sight defined by the hole on the extraction and acceleration plates. Actual photograph of extraction and acceleration section is shown in figure 2.11.
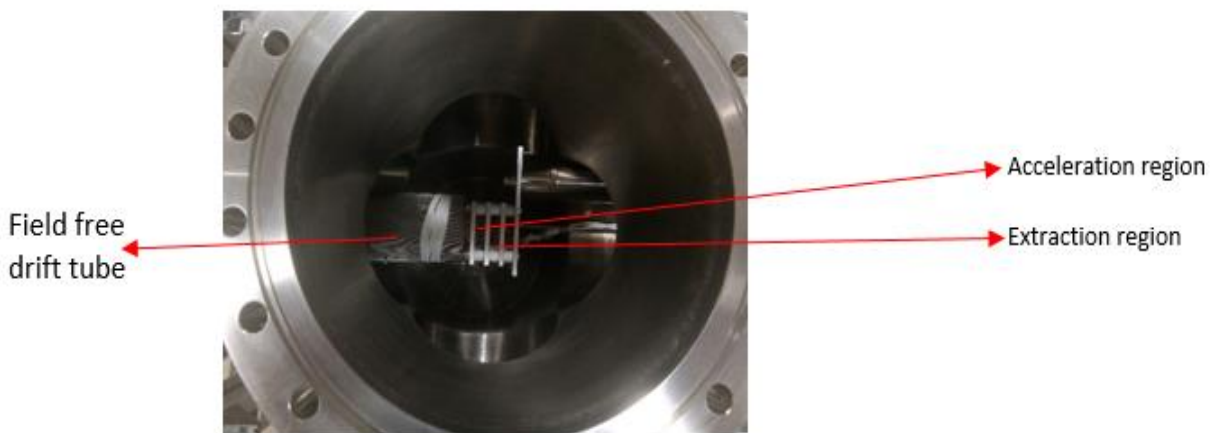


Figure 2-11: Photograph of extraction and acceleration region

## 2.5.1.2    Field free drift region (FD)

A metallic mesh tube is extended from the grounded plate of acceleration electrode up to the entrance plate of PPA. It serves as field free drift to the accelerated ion (see figure 2.11). Length of this tube is 780mm. Initial testing was done without this shielding tube, Therefore, the ion trajectory inside the FD was seemed to be disturbed by the acceleration field. It was one of the reasons of poor ToF resolution at the beginning.

## 2.5.1.3    Parallel plate analyzer PPA

The PPA is kept at $45°$ to the FD tube. The whole PPA assembly is enclosed in a cylindrical chamber, which is extended along the ToF axis as a drift tube for the passage of undeflected neutral particles (see figure 2.10 & figure 2.12). A position sensitive detector (PSD) with MCP and delay line anode is mounted on the end flange of this tube for detecting neutral particles. This detector is called a neutral detector. This chamber is maintained at $4 \times 10^{-8}$ mbar. The PPA assembly includes two metallic parallel plates of length 640 mm and breadth 200 mm, kept 138 mm apart. The first plate of PPA has an entrance hole of size 20mm. The second plate is biased to high voltage and has an exit hole of size 50 mm that allows the neutral fragment to cross the PPA and reach the neutral detector in line. The hole is covered with a fine nickel mesh for a uniform field. This arrangement is done to perform correlated measurement of ion and neutral fragments of a dissociation event. The ions entering into the energy analyzer are deflected to a parabolic trajectory, and the horizontal length traversed by the particle is proportional to its kinetic energy for a given biasing voltage. The energy dispersed ions cross the entrance plate as they complete their parabolic trajectory with a mean range of 500 mm through an exit hole of diameter 50 mm. After the exit, they are detected by a second PSD (ion detector) which is kept at about 20 mm away from the exit hole. Dimensions of the parallel plates are optimized to have field uniformity and energy resolution while limiting the size to practical dimensions. The field uniformity is achieved with the help of 13 uniformly spaced metallic frames, which are biased linearly with distances. The effective size of the detector (46 mm) helps in measuring ions with closely spaced energies while covering over 9% of the mean energy.

Initially, the full ion beam (beam size was typically 4 mm) was allowed to enter inside the analyzer through the entrance hole of PPA. It was aligned to the center of neutral detector by adjusting the position of interaction chamber and it was also taken care that beam could be easily deflected to center of ion detector. The large entrance hole of PPA is reduced to a tiny slit with width 1mm and length 1cm. This greatly improved energy resolution of the spectrometer to 1 in 430. The 2D schematics of the setup showing trajectory of ion and neutral beam as well as data acquisition system is shown in figure 2.12.
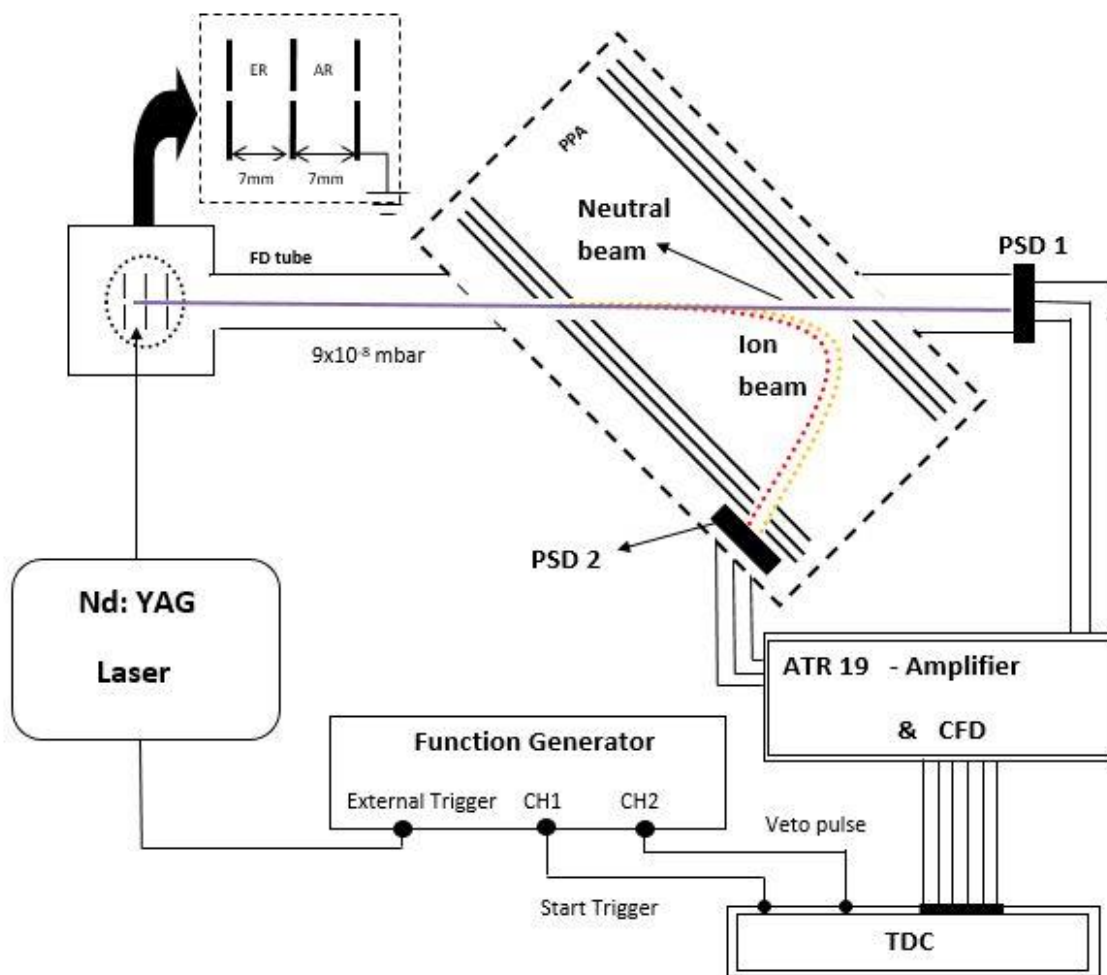


Figure 2-12: 2D schematics of the setup showing ion and neutral beam as well as data acquisition system.

2.5.1.4    Nanosecond tunable laser system

The laser used here is an OPO (Nd: YAG pumped OPO laser) based tunable one with wavelength regime UV to IR (225 to 2600 nm), Model: EKSPLA NT242P series. The laser has 10 mJ pulse energy, 100Hz pulse repetition rate, 5 cm$^{-1}$ line width, 3-6 ns pulse duration and a beam diameter 4mm.
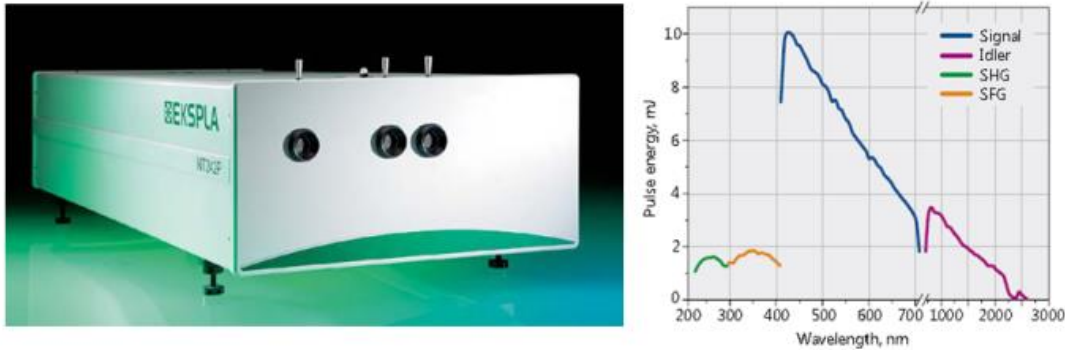


Figure 2-13: Nanosecond tunable laser system used in this experiment (left) and typical output pulse energy (right). Figures adapted from laser datasheet[46].

2.5.1.5    Timing sequence and data acquisition system

The output trigger pulse from the laser was used as the reference for the rest of the timing sequence as shown in figure 2.12. This pulse was multiplexed with the help of a function generator and its multiple outputs were used to trigger the laser power meter as well as the data acquisition system. The synchronization of the laser optical pulse with the logic pulse was ascertained using a fast photodiode and was found to have an overall jitter of 148 ps. Each PSD signals were fed to fast amplifiers and CFDs (ATR19 by Roentdek GmBH) to produce NIM pulses. These were used as stop pulses to measure ToF and position on five separate TDC channels. A fast TDC (model: Agilent Acquiris TC890) was used to convert these pulses into time duration with respect to the start trigger from the laser.

2.5.2    Functional testing of high resolution energy-ToF spectrometer:

The spectrometer can be operated in three possible modes, namely standard ToF mode (using neutral detector), high resolution energy-ToF mode (using ion detecor) and ion-neutral coincidence mode (using both detectors). Functionalities of all the modes are tested and verified as described in the following sections.

2.5.2.1    ToF spectrum recorded on neutral detector (standard ToF mode)

The spectrometer is tested using high power of 3rd harmonics (355 nm) of Nd: YAG laser. The typical pulse energy of $3^{rd}$ harmonics was about 23mJ. It helped to produce high ion count rate very easily. This was used for the preliminary testing of the spectrometer. A typical ToF spectrum measured for naphthalene using neutral detector is shown in figure 2.14.
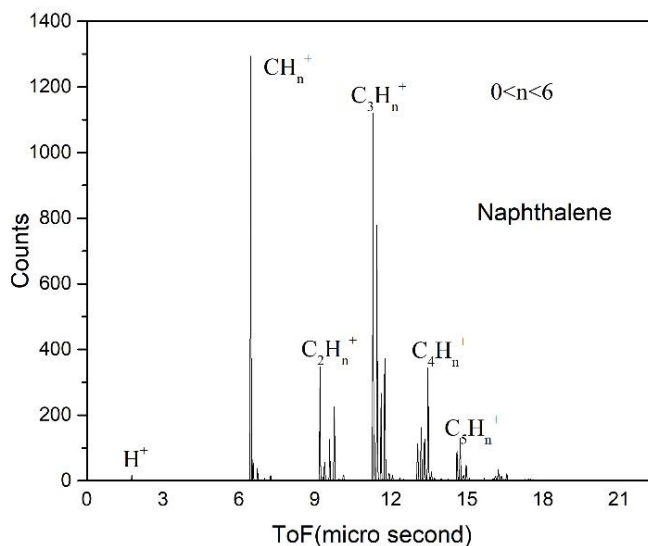


Figure 2-14: ToF spectrum recorded on neutral detector for 3rd harmonics of laser (355nm) with laser pulse energy is 23mJ.

The carbon clusters such as $C_mH_n^+$ ions (where 1<m<6 and 0<n<6) and $H^+$ were detected due to very high laser intensity. It was typically about $10^{12}$ W/cm$^2$ for third harmonics. At these higher intensities, the electric field of laser is commensurable to the molecular electric field. It

produces a deformed molecular electrostatic potential, which can reduce the electrostatic barrier of the electrons partially. It is indeed enough to reduce the binding energy of electrons. In this limit, electrons are ejected freely and atomic and molecular ions can be detected very easily. But our interest was to produce internally excited intact molecular cations of PAH. It was accomplished by using low UV laser intensities from OPO system. Therefore, further testing and investigation was performed using low energy (10μJ) UV (225-293nm) pulses.

## 2.5.2.2    Improvement of ToF resolution

A typical ToF spectrum recorded at the beginning for improper ER and AR regions are shown in figure 2.16 (a). Nonuniformity in the electric fields of ER and AR could have caused poor time resolution. The possible origin of such nonuniform field is discussed below.
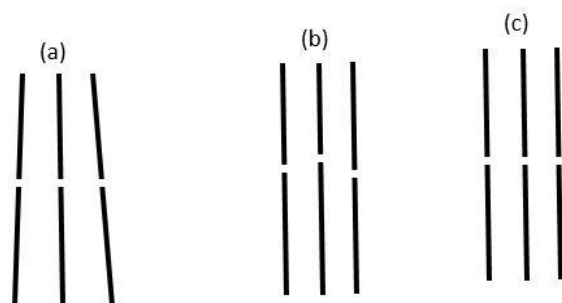


Figure 2-15: Schematics of extraction -acceleration region (not to scale)  (a) Electrode plates are not parallel, (b) holes are not aligned each other and (c) Perfect alignment

If the electrode plates are not parallel, a nonuniform field can setup across the gaps. Such a field can never guide ions along or parallel to ToF axis. The double field requirement adds to the complexities. This can severely affect the ToF resolution. Moreover, if the holes are misaligned, it can perhaps stop the ion beam from exiting the field regions. The initial testing was done with very poor ER and AR and it was very necessary to extract the ion beam from a particular interaction point. Such an arrangement is not favorable to perform high resolution measurements. The field uniformity was improved by aligning electrode plates parallelly and a narrow extraction of ions was ensured by reducing the aperture size (0.7mm) on the plates. Moreover, the entrance of FD tube was shielded from ER and AR fields using a grounded mesh

tube. This greatly improved mass resolution. The present value of mass resolution is 1 in 3000. One example of highly resolved ToF spectrum is shown in figure 2.16 (b).
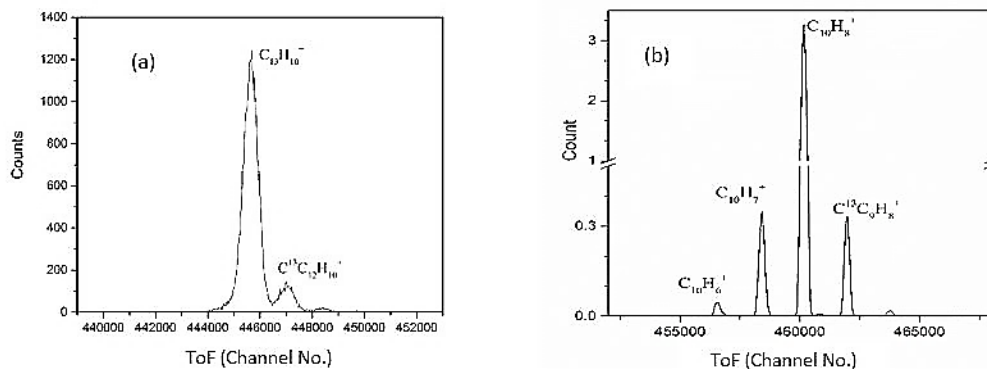


Figure 2-16: (a) Low resolution ToF measured on ion detector, with poor ER and AR (b) High resolution ToF measured on ion detector, after improving ER and AR of the spectrometer.

## 2.5.2.3     Energy selective ToF using PPA (High resolution energy-ToF mode)

A typical ToF spectrum recorded for fluorene by ion detector of PPA at 263nm is shown in figure 2.17. The relative yield of lighter fragments is observed to be very low compared to the intact parent ion and H-loss daughter ions. The smaller fragments are produced with very low yield because certain laser pulses can have very high energy and produce a catastrophic fragmentation of the molecular structure followed by the fragment absorbing one or two UV photons and getting ionized. However, the main focus of our study is on high mass region, where the dominant parent ($C_{13}H_{10}^+$) peak is followed by the isotope peak and preceded by H, 2H, and 3H loss channels. The mass resolution is about 1 in 3000 so as to clearly separate various H, 2H loss as well as isotopic peaks. In the ToF spectrum, the peak corresponding to the H loss channel is slightly broader than its parent ion. Moreover, the valley between the parent and H loss peak is filled with data points despite having good resolution (see H loss region of figure 2.17). It will be useful to check the 2D image of ion beam on the ion detector.
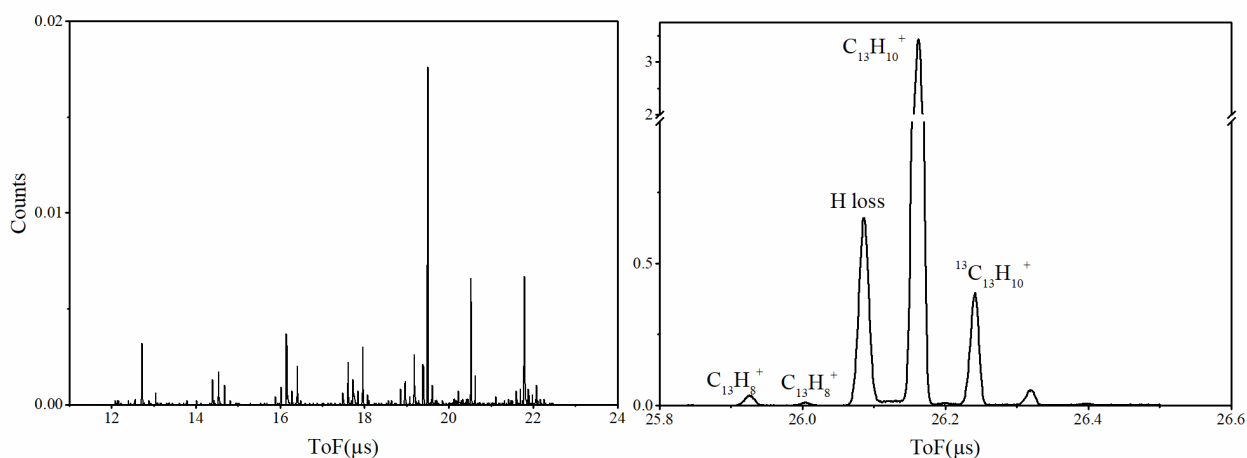
Figure 2-17: Energy selected ToF spectrum of fluorene

2.5.2.4    Image of ion beam on the ion detector

2D image of ion beam on ion detector was very interesting. It consists of a very strong peak having maximum horizontal range, always preceded by a distinct and weak peak along horizontal coordinate of the detector as shown in figure 2.18.
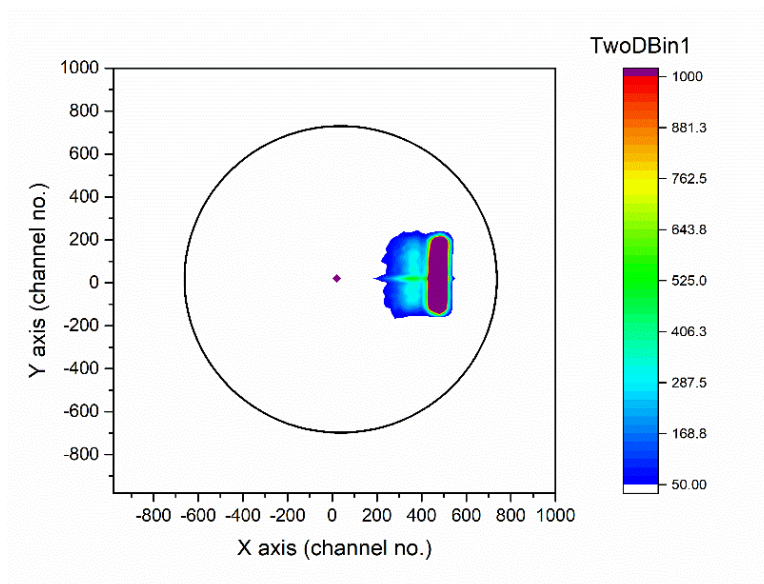


Figure 2-18: 2D image of ion beam on ion detector

The peak at maximum horizontal range will contain ions with maximum kinetic energy. It will be mostly parent ions and fragment ions produced just after the laser interaction. We suspected that low energy weak peak on the 2D image can from H loss dissociation after full acceleration. For more clarity, we plotted 2D image of parent and H loss fragment ion peak separately as shown in figure 2.18. (H loss fragment is identified from ToF spectrum). The complete procedure of energy correlated ToF analysis are given in the next chapter.
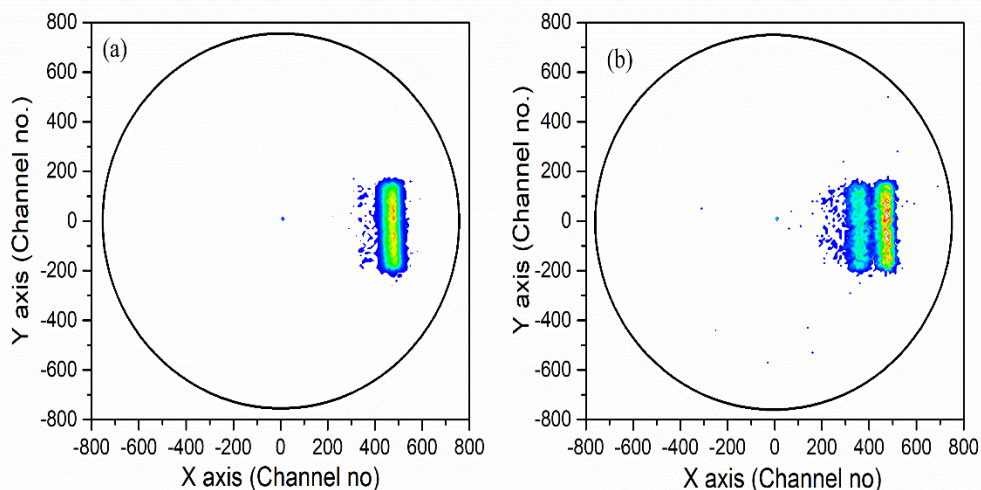


Figure 2-19: Mass selected 2D image of parent peak (a) and H loss fragment (b) ion peak.

### 2.5.2.5    Ion-neutral coincidence mode

During the preliminary testing we could record ion and neutral fragments in coincidence for H loss and $C_2H_2$ loss channels. This is illustrated for anthracene cations in figure 2.20. This mode of detection was not continued in this work, because, ion beam is directly shooted towards the neutral detector for the present configuration of the spectrometer. Therefore, the chances of false coincidences can be very high. We require low count rate to counteract the false coincidences. This can be achieved in future by carefully shifting the line of sight of the main beam away from the neutral detector.
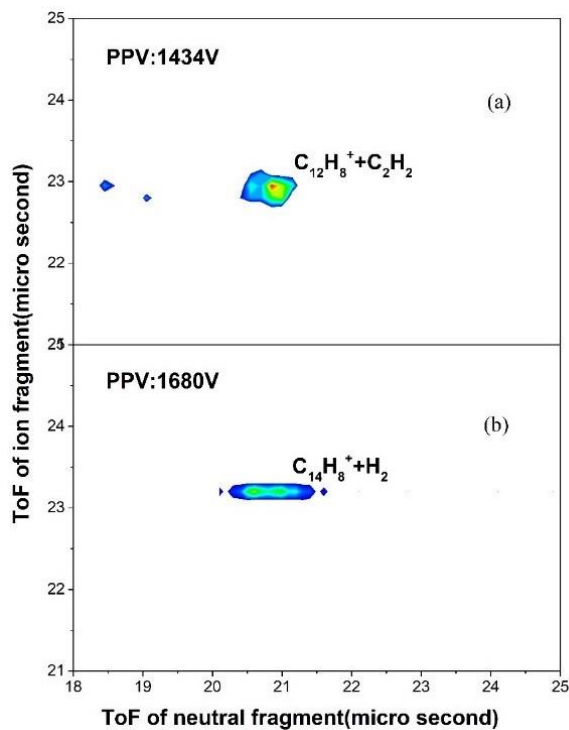
Figure 2-20: Neutral versus ion ToF coincidence map recorded for (a) $C_2H_2$ loss and (b) H loss channel of anthracene$^+$

## 2.6    Summary

The investigation of unimolecular dissociation requires complex mass spectrometric techniques. Sophisticated ToF mass spectrometers have been used in this work to measure time dependent dissociation processes of PAH cations. It is achieved with the help of complex arrangement of multiple detectors and fast signal processing. The signal processing and timing logic is embedded in the hardware, the timing information is retrieved after the post processing by putting conditions on coincidences in a suitable manner.  This requires very careful preparation and planning. Those details which influence our information are mainly mass resolution and position resolution in case of a PSD. In the case of energy correlated ToF mass spectrometer, position resolution is directly related to energy resolution. A very good quality mass spectrometer with mass resolution 1 in 3000 and energy resolution 1 in 430 is realised. The spectrometer has helped to quantify H loss emission rate of PAH ions at lower internal energy. The complexity of such an instrument is highlighted here. The details of the timing algorithm are of vital importance when the data is post processed. It will be described in the next chapter.

# CHAPTER 3. DATA PROCESSING AND ANALYSIS

Modern day pulse processing and data acquisition (DAQ) are very fast and can acquire a large quantity of data in short time. The time correlated measurements in ToF technique take advantages of that and acquire timing data in a multitude of ways. Typical ToF needs a reference signal and detection signal. The reference signal can either be taken from another detector or from a random or periodic pulse generator. A standard ToF measurement often acquires data with picosecond bin size. Moreover, a single trigger or a reference signal can produce multiple detections using multihit DAQ with data size ranges from hundreds of megabytes to several gigabits. In addition to the quantity of the data, the cross correlations in multihit signals and hence, multidimensional data makes the data processing very challenging.

The data analysis can be done using many different types of platforms. Some of them are specific to analysis like ROOT, Origin, Octave, Igor, etc and some of them are general purpose like Matlab, C++, and python etc. Careful planning and comprehensive understanding of the experimental scheme are needed to design a specific data analysis algorithm and a good computational programing skill are essential for the implementation of the same. In some special cases the data analysis itself is not adequate and it may require various types of simulations to assist in the analysis process. The data reduction, analysis and simulation carried out in this thesis work using Root, origin and C++ etc are described in this chapter.

## 3.1 Proton-PAH collision experiment

The high energy proton collision experiments with PAHs and PANHs was studied using a simple standard ToF mass spectrometer. Simpler PAH isomers namely, azulene ($C_{10}H_8$) and

naphthalene were used as the main targets of this study. Quinoline and isoquinoline were used as the targets to perform fast proton-PANH collision experiments. The recoil ion signals were detected using PSD (MCP with DLA) combined with secondary electron detection and neutralized projectile detection. They were used to generate various timing signals. These signals were recorded using a fast multihit TDC in common stop mode and the resulting data were stored in the list mode. Considering the high volume of the data (each file about 100 Mb), a customized ROOT program was used for the single and multihit analysis. The details of analysis and evaluation of various parameters are described in this section.

### 3.1.1 ToF of recoil ions under different target excitations
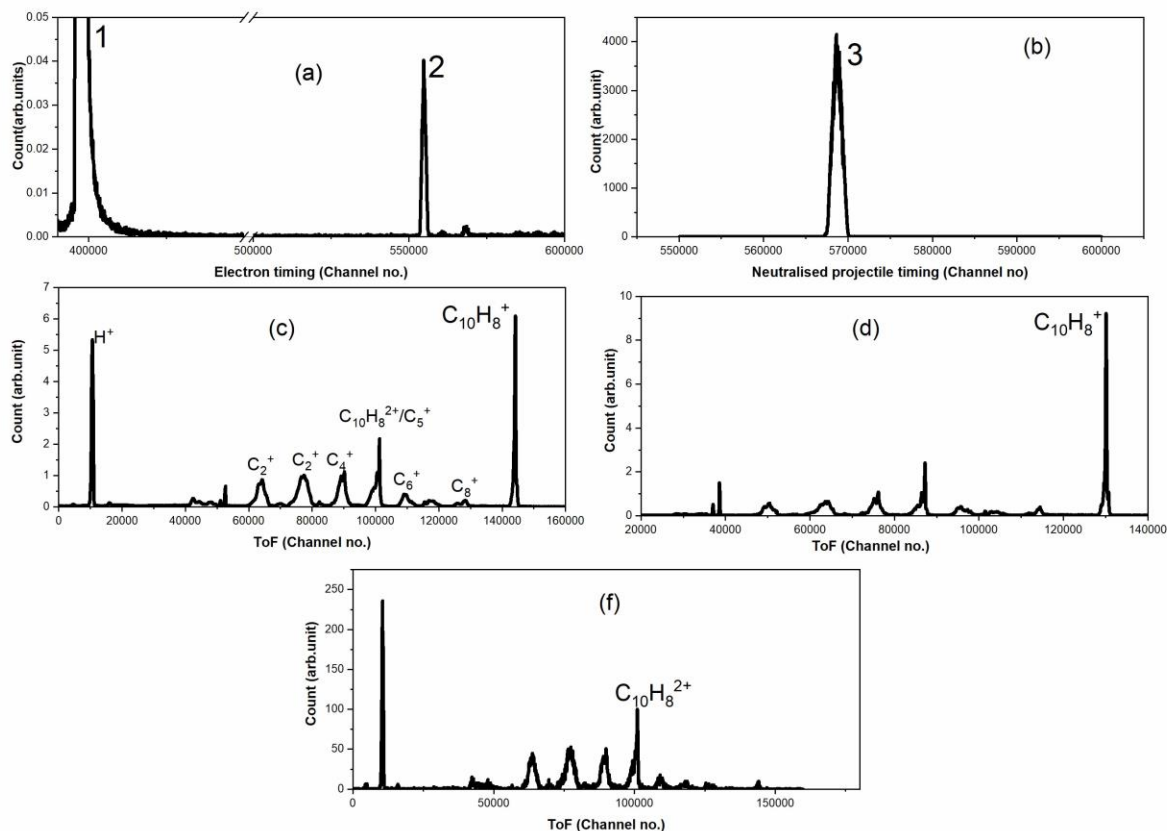


Figure 3-1: Time marker of (a) electrons, (b) neutralized projectiles and ToF of recoil ions produced in (c) EE (d) EC and (f) CI mode.

The intact or fragment ions from fast proton-PAH interaction were detected in coincidence with emitted electron, neutralized projectile or both. The ToF of recoil ions were measured using time markers of electron or neutralized projectile. The electron time marker is shown in figure 3.1(a). There are two timings in which electrons are detected and it is marked as 1 and 2 in figure 3.1(a). The electron timing 1, marks pure secondary electron production in proton-PAH collision. The ions detected in this event belong to electron emission (EE) mode and a naphthalene ToF spectrum recorded in this mode is shown in figure 3.1 (c). Whereas, the correlated detection of electron and neutralized projectile is marked by the 2nd electron timing as shown in the figure 3.1(a). This corresponds to capture ionization (CI) process. An example of ToF spectrum of naphthalene produced in CI event is shown in figure 3.1(f). Since, the target loses two electrons in CI events, no singly charged naphthalene ions were expected in this spectrum. The low intensity intact peak observed in this mode is due to chance coincidence. A typical neutralized projectile time marker is shown in figure 3.1(b). It can be used to separate electron capture (EC) events. An EC mode ToF spectrum of naphthalene is shown in figure 3.1 (d).

Different modes of target excitations, particularly EE and EC modes are of considerable interest in this work. A large fraction of internally excited singly charged naphthalene ions were expected to be produced in EE and EC modes by the advent of high cross section plasmon excitation and resonance electron transfer processes[47,48]. One of the important objectives of this work was to compare electronic relaxations of azulene and naphthalene in EE and EC processes. For this, excitations itself needed to be compared in these molecules before studying their dissociation or relaxation channels. The cross sections of EE and EC modes can be measured by normalizing the parent ion yield with respect to target and projectile densities and correcting for their detection efficiencies. But, the absolute values of target and projectile densities were not known to us to determine the absolute cross sections, though they were same in EE and EC processes. Therefore, we planned to measure the ratio between EE and EC cross sections for two molecules for the studied proton impact energies with the help of electron and neutralized projectile detection efficiencies. The procedures to estimate detection efficiencies of electron, neutralized projectile and recoil ion are explained in the following sections. The areas of intact and fragment ions from one dimensional mass spectra were often extracted and used for different analysis.

**Electron detection efficiency:** We have used double ionization yield produced in EC mode to deduce electron detection efficiency. Double ionization events are possible to be produced in EC mode along with the emission of an electron. The probability of double electron capture by the proton is expected to be negligible. Double ionization events are integrated for EC mode with and without electron detection. The area of double ionization peak with electron detection, $A_e^{++}$ is given by,

$$A_e^{++} = \sigma^{++}.N_t.N_p.\varepsilon_i.\varepsilon_p.\varepsilon_e \tag{3.1}$$

Where $\sigma^{++}$ is double ionization cross section, $N_t$ is target density and $N_p$ is projectile density and $\varepsilon_i$, $\varepsilon_p$, $\varepsilon_n$ are detection efficiencies of recoil ion, projectile and electron. Similarly, area of double ionization peak without electron detection, $A_{1-e}^{++}$ is given by,

$$A_{1-e}^{++} = \sigma^{++}.N_t.N_p.\varepsilon_i.\varepsilon_p.(1-\varepsilon_e) \tag{3.2}$$

We can calculate electron detection efficiency from equations (3.1) & (3.2),

$$\varepsilon_e = \frac{k}{k+1}, \text{Where } k = \frac{A_e^{++}}{A_{1-e}^{++}} \tag{3.3}$$

We have calculated detection efficiency, $\varepsilon_e$ for all projectile energies using equation (3.3). The mean value $\varepsilon_e$ measured is 0.102.

**Detection efficiency of neutralized projectile:** The projectile detection efficiency depends on the energy of the projectile and other external experimental parameters. We have deduced it with the help of background water peak obtained in EE and EC modes under the constraint of the target experimental condition and electron detection efficiency. The area of water peak, $A^{ee}$ determined from the EE mode recoil ion spectrum is given by,

$$A^{ee} = \sigma^{ee}.(N_t)w \ .N_p.(\varepsilon_i)w \ .\varepsilon_p \tag{3.4}$$

Where $\sigma^{ee}$ is the ionization cross section of water for a given projectile velocity. Similarly, the area of water peak measured from EC mode data, $A^{ec}$ is given by,

$$A^{ec} = \sigma^{ec}.(N_t)w \ .N_p.(\varepsilon_i)w \ .\varepsilon_p \tag{3.5}$$

Where $\sigma^{ec}$ is the electron capture cross section of water for a given projectile velocity. Therefore, the detection efficiency of neutralized proton for a particular proton energy is given by,

$$\varepsilon_p = \frac{A^{ec}.\sigma^{ee}}{A^{ee}.\sigma^{ec}} \varepsilon_e \tag{3.6}$$

The values of $\sigma^{ee}$ and $\sigma^{ec}$ are taken from previously published ionization and electron capture cross sections measured for water at different proton energies[49]. The detection efficiencies of neutralized projectile for different proton energies are listed in table 3.1. To avoid contamination from unneutralised main beam a fine slit is arranged in front of the neutral detector which has considerably reduced the detection efficiency.

Table 3.1: Proton projectile detection efficiency for different energy.

| Proton energy (keV) | Detection efficiency |
|---|---|
| 50 | 0.01933 |
| 75 | 0.02514 |
| 100 | 0.04616 |

| | |
|---|---|
| 125 | 0.03031 |
| 150 | 0.05511 |

**Detection efficiency of ion:** The ion detection efficiency of MCP detector is obtained using an empirical model reported in literature[50].The detection efficiency is characterized by the following polynomial

$$\log[\eta] = A + B\chi + C\chi_2 + D\chi_3 + F\chi_4 \tag{3.7}$$

Where, $A = -0.257$; $B = 0{:}161$; $C = -0{:}239$; $D = -0{:}0184$; $F = -0{:}3$; $\chi = log\ [E/M^{0.5}]$, where $E$ is energy of impact ion in keV, $M$ is mass of ion in a.m.u. and $\eta$ is detection efficiency. The detection efficiency of singly and doubly charged naphthalene ion for the MCP detector is estimated to be 0.25 and 0.57.

**Ratio between EE to EC cross sections:** Let $A^e$ be the total single ionization events produced in EE mode and $\sigma^e$ be the EE cross section

$$A^e = \sigma^e. N_t. N_p. \varepsilon_i. \varepsilon_e \tag{3.8}$$

Let $A^{ec}$ be the total single ionization events produced in EC mode and $\sigma^{ec}$ be the EC cross section

$$A^{ec} = \sigma^{ec}. N_t. N_p. \varepsilon_i. \varepsilon_p \tag{3.9}$$

Ratio between EE and EC cross section can be deduced for every proton energies using the following expression

$$\frac{\sigma^e}{\sigma^{ec}} = \frac{A^e. \varepsilon_p}{A^{ec}. \varepsilon_e} \tag{3.10}$$

### 3.1.2    Normalisation procedure to compare first hit data of azulene and naphthalene

The first hit proton impact data of azulene and naphthalene were extracted and normalized to the sum of singly charged parent ion, neutral H loss and neutral $C_2H_2$ loss yield. This was done partly because the neutral H loss contribution, though very small, was difficult to separate from the parent peak. Moreover, the H loss and $C_2H_2$ losses were statistical processes and their proportions can vary considerably due to the process of isomerization in the parent ions. All the one dimensional (1D) spectra shown henceforth are normalized by this procedure and multiplied by a factor of 1000 (arbitrary factor). In spite of totally separate normalization, the first hit yield of azulene and naphthalene were in very good agreement with each other as shown in figure 3.2. Moreover, some peaks overlapped exactly. The normalized first hit yield of azulene is subtracted from that of naphthalene as shown in figure 3.2 to elucidate this point further.
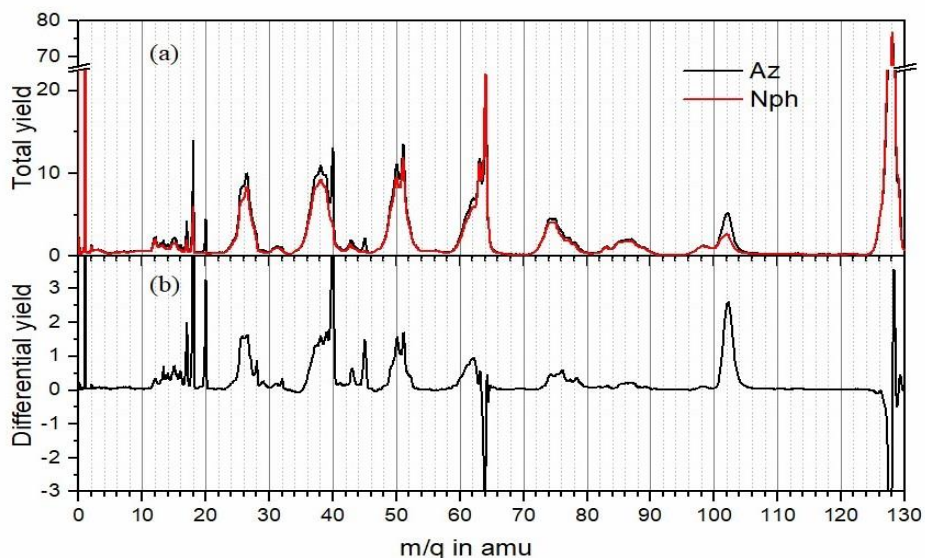


Figure 3-2: (a) Normalized first hit mass spectrum of azulene and naphthalene, (b) Differential yield of azulene measured by subtracting normalized first hit yield of azulene from that of naphthalene.

### 3.1.3    Normalization procedure for neutral loss channels

In the absence of an absolute normalization, the relative yield of neutral loss channels of azulene and naphthalene is estimated with respect to a standard peak appearing in the mass spectrum. The single ionization peak was chosen as the standard peak in case of EE and EC modes. We have measured the relative yields of H, $C_2H_2$ and $H_2$ loss channels of singly and doubly charged azulene and naphthalene ions with respect to their respective parent ion peaks for every projectile energy. Relative cross section of double ionization is measured by normalizing double ionization events with respect to single ionization peak. It is repeated for all projectile energies.

### 3.1.4    Double hit analysis

The use of a multihit time digitizer enabled measurement of as many as eight fragments from a given event in the TOF spectrometer, provided that their flight times differed from each other by more than 10 ns. Entire data was sorted for two hit events and then a 2D plot is made with first hit on the horizontal axis and second hit on the vertical axis. The second hit mass spectra of certain first hit channels namely, $H^+$, $C^+$ and $CH_3^+$ were plotted separately both for naphthalene and azulene (one example of $C^+$ channel is shown in figure 3.3).
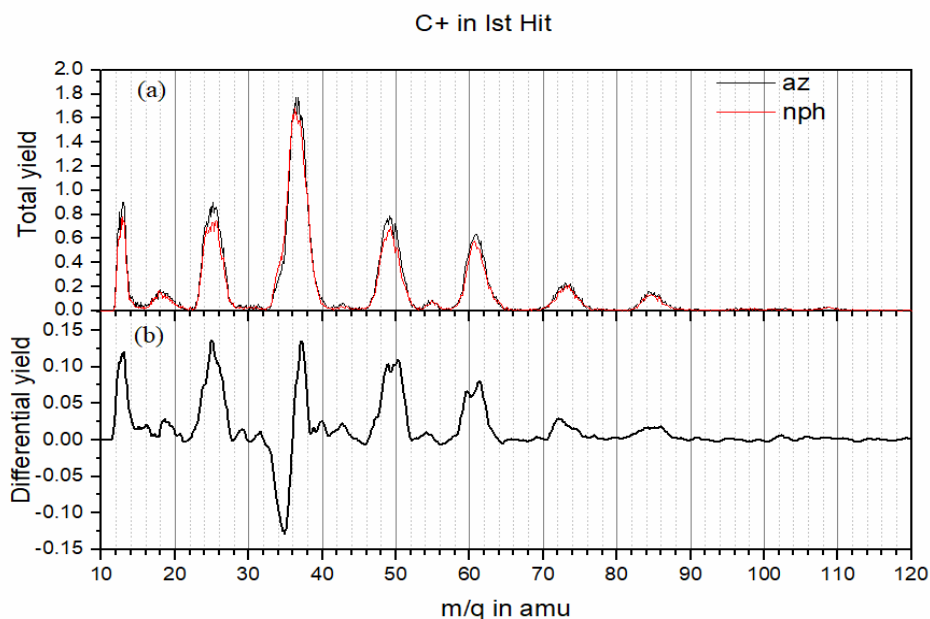
Figure 3-3: (a) Second hit ion yield produced for $C^+$ channel, (b) Differential yield of azulene measured with respect to naphthalene.

### 3.1.5    2D coincidence map for fragmentation channels

Multihit data can be used to carry out multidimensional analysis of fragmentation process. This gives us useful information about momentum distribution of fragmentation channels along ToF axis as shown below. The momentum component along the ToF axis, $p_z$ can be deduced from the measured ToF, $t$ of the fragment ion. A reference time, $t_0$ for each possible fragment ion was identified from the single hit ToF spectrum. The time difference between the measured and the reference values was used along with the ToF mass spectrometer parameters (ToFMS) i.e., geometry and fields to determine $p_z$, It is given by

$$p_z = m v_z = qE\,(t - t_0) \tag{3.11}$$

where $q$ is charge and m is mass of fragment ion and $v_z$ is the velocity component of fragment ion along ToF axis. $E$ is the extraction field of ToFMS. The momentum correlation of the fragmentation channels can be investigated using 2D coincidence map (first hit ToF versus second hit ToF). A typical 2D coincidence map plotted for the multihit proton impact data is shown in figure 3.4.
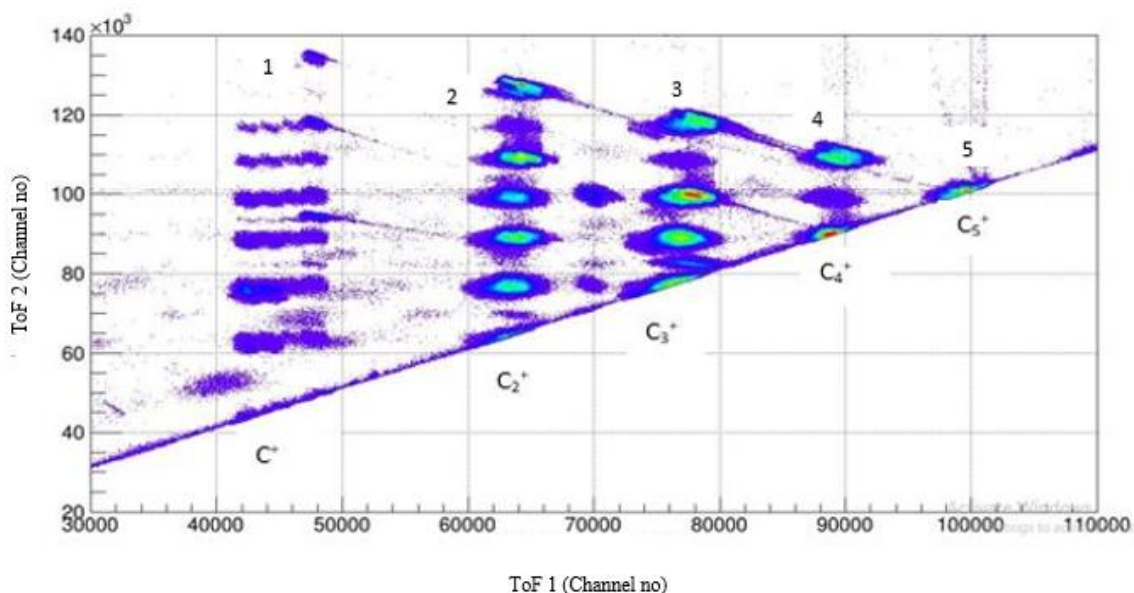


Figure 3-4: 2D coincidence map obtained for naphthalene, the binary fission channels are shown as 1. $C_9^+ + C^+$, 2. $C_8^+ + C_2^+$, 3. $C_7^+ + C_3^+$, 4. $C_6^+ + C_4^+$, 5. $C_5^+ + C_5^+$.

The islands with different slopes can be seen in the 2D map. Details of slope analysis for binary fragmentation channels are given below. We have identified important binary fragmentation channels of PAH dications and measured their kinetic energy release (KER). The detailed description of KER analysis is given in the next section.

**Slope analysis of two body fragmentation:** A multiply charged molecular ion AB with charge $q_1 + q_2$ fragmenting into A and B with charges $q_1$ and $q_2$ respectively, where A is the first fragment and B is the second fragment detected. In this two-body fragmentation process, the momentum along ToF axis of first fragment $(p_{z1})$ would be equal to momentum along ToF axis of second fragment $(p_{z2})$. Therefore, we can write

47

$$p_{z1} = q_1 E \ (t_1 - t_0) \tag{3.12}$$

$$p_{z2} = q_2 E \ (t_2 - t_0) \tag{3.13}$$

Where $t_1$ and $t_2$ are the fragment ToFs. We can deduce an expression for ratio between charges of fragment ions using expression (3.12) & (3.13).

$$\frac{q_1}{q_2} = -\frac{(t_2-t_0)}{(t_1-t_0)} = \text{slope of fragmentation channel} \tag{3.14}$$

Few 2-body fragmentation reactions and their slope in 2D correlation diagram is given below.

$$AB^{2+} \rightarrow A^+ + B^+ , \text{slope} = -1 \tag{3.15}$$

$$ABC^{3+} \rightarrow AB^{2+} + C^+ , \text{slope} = -2 \tag{3.16}$$

$$ABC^{3+} \rightarrow A^+ + BC^{2+} , \text{slope} = -0.5 \tag{3.17}$$
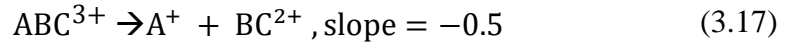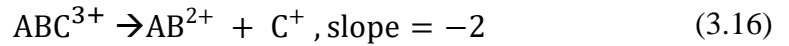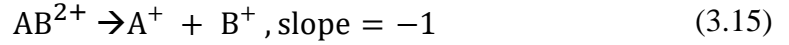
### 3.1.6    Measurement of KER release for binary fragmentation channels

We have done an event-by-event analysis of the 2-hit coincidence data to determine the three velocity components and hence kinetic energy of each fragment ion individually. The KER distribution was then obtained from the contributions of correlated fragment ion pairs. The velocity component parallel to the ToFMS axis, $v_z$ is deduced from the measured ToF, $t$ of the fragment ion (see equation 3.11). The other two components of the velocity, $v_x$ and $v_y$ were determined from the position of impact, $x$ and $y$ of the fragment ion on the MCP. The reference points $x_0$ and $y_0$ were determined for each event by taking the center of mass of the $x$ and $y$ position

of each pair of fragments detected in coincidence. The $x$ and $y$ components of the velocity is given by equations (3.18) and (3.19).

$$v_x = \frac{x - x_0}{t} \tag{3.18}$$

$$v_y = \frac{y - y_0}{t} \tag{3.19}$$

A typical example of KER distribution measured for one of binary fragmentation channels detected in case of naphthalene and azulene proton impacts is shown in figure 3.5.
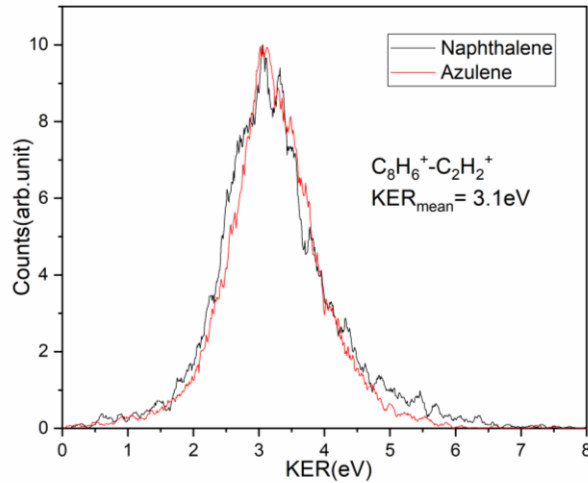


Figure 3-5: Kinetic energy release spectra of the $C_8H_6^+$-$C_2H_2^+$ fragmentation channel detected in proton impact data of naphthalene and azulene.

### 3.1.7 Multihit analysis to compare multifragmentation channels of azulene and naphthalene

The multihit data of azulene and naphthalene was first filtered and cleaned for EE mode and for various sum conditions on the PSD. The event record was obtained upto eight multihits. The fragmentation up to only third hit was processed, beyond which the positive counts were negligibly small. Typically for a projectile energy of 50 keV, about 76% events were pure single hit, about 19 % of pure double hit and less than 4% were triple hit. The exact percentage is strongly dependent on the detection efficiency which varied from about 45% for single carbon

fragment ion to about 20% for intact molecular ion. The data from all the five projectile energies were added together to improve the statistics of multi hit analysis. The branching ratios of multifragmentation channels was not estimated, because the detection efficiency is expected to vary considerably over the recoil ion mass and velocity.

## 3.2 High resolution energy-ToF spectrometer: data processing and analysis

The proton impact study of PAHs is carried out using an established experimental set up with very well understood and well characterized analysis algorithm. But as we combine the standard ToF technique with energy analyzer in order to develop a new experimental facility, the required data processing and coincidence logic had to be evolved in a unique manner. This section is dedicated to explain the data analysis methods used for the new experimental technique. The recoil ion ToF is produced with reference to the master trigger from nanosecond laser in common start mode. The laser pulse energy is recorded using a power meter, which is synchronized with respect to the master trigger of the laser. The repetition rate of laser system is 100Hz. Therefore, time duration for a single event is 1ms. We have enabled first the 100µs as the active time window of DAQ using of veto pulse of same frequency. The ToF spectrum measured for fluorene (at 263nm) and azulene (at 235nm) using ion detector with their mass calibration graph is shown in figure 3.6. The mass resolution is well beyond 1 in 3000 so as to clearly separate various H, $H_2$ loss as well as isotopic peaks. The heavy fragment loss channels, for example $C_2H_2$ loss channel (see figure 3.6 (a)), has an assymetric peak shape due to a large spread in the kinetic energy of fragment ions.

### 3.2.1 Laser intensity dependence on ionization and fragmentation channels

A well-known technique based on dependence of laser intensity on ionization and fragmentation yield was employed to check the corresponding *n*-photon processes. The laser pulse energy recorded in event by event mode was used for this analysis. Although, the average pulse energy was about 10 µJ, energy of laser pulse fluctuated between 1µJ and 30 µJ. The ion signals were sorted for a window of 1 µJ and the ion signals of interest within one energy window was integrated and normalized with total number of laser pulses recorded in the same window.

Slope of log-log plot of the ion yield against the laser intensity will be the number of photons involved in the process of ionization or fragmentation. Here we have shown a laser intensity dependence on ionization channel as well as H loss fragmentation channels of azulene and fluorene at 235nm and 263nm respectively. Though we have got a clear photon number in these examples, similar approach was failed to identify a clear $n$-photon process for certain other wavelengths.

The log-log plot of the ion yield against the laser intensity, individually for fluorene ion and its H loss channel at 263nm, is shown in figure 3.7 (a). The slope of the $C_{13}H_{10}^{+}$ data was found correspond to a 2-photon excitation, whereas the $C_{13}H_{9}^{+}$ yield clearly follows a 3-photon process. The nonlinear region of figure 3.7 is excluded from the analysis, because in this region, photoabsorption cross section can be drastically modified due to higher laser intensities. Similar 2 and 3-photon excitation process is identified for ionization and H loss fragmentation channels of azulene at 235nm as shown in figure 3.7 (b).
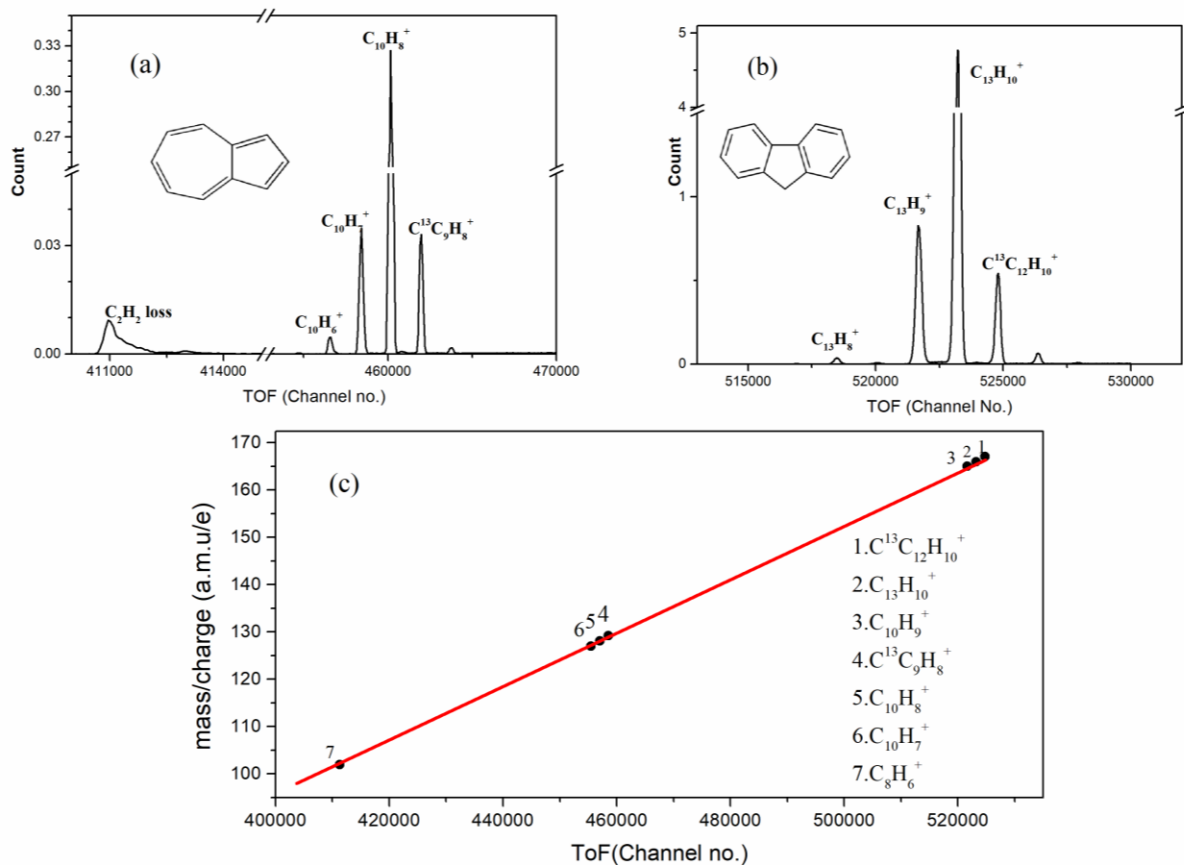
Figure 3-6: ToF spectrum of (a) azulene at 235nm and (b) fluorene at 263nm for an average pulse energy of 10μJ, (c) calibration plot.
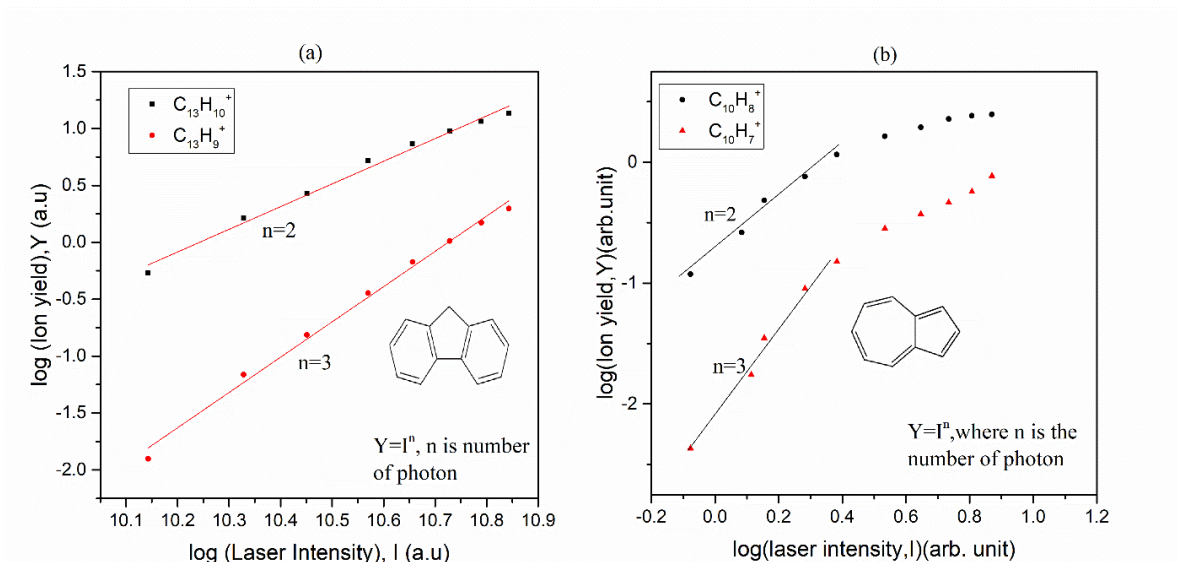
Figure 3-7: Intensity dependence of single ionization of and H loss fragment ion yield for (a) fluorene at 263nm and (b) azulene at 235nm.

## 3.2.2    2D coincidence map between ToF and horizontal position of ions

The 2D image of ion signal on the ion detector is shown in figure 3.8. The deflection voltage of PPA analyser is set to 1.6kV for this measurement. The ion signal is dispersed along horizontal coordinate of the detector. The full energy ions hit the detector at maximum horizontal coordinate and the low energy ions arrive the detector at shorter horizontal coordinates.
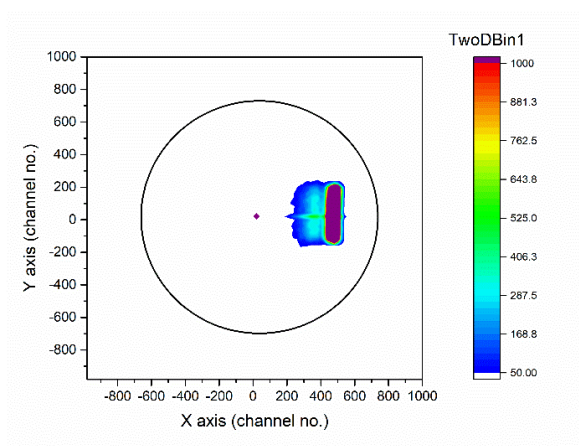


Figure 3-8: 2D image of the ion beam recorded on ion detector for fluorene at 263nm for a pulse energy of 10μJ.

53

A typical 2D correlation diagram plotted between ToF and horizontal position of important fragment ions are shown in case of azulene and fluorene in figure 3.9.
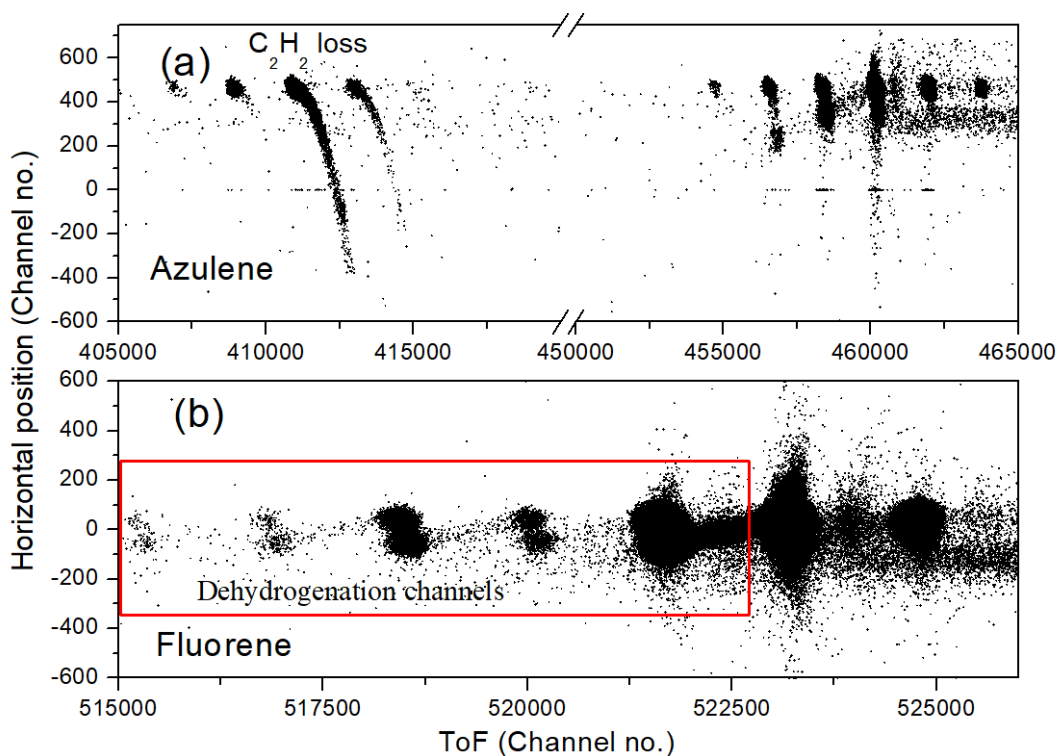


Figure 3-9: 2D spectrum of ToF versus Horizontal range recorded for (a) azulene (at 235nm) and (b) fluorene (at 263nm) for an average pulse energy of about 10μJ.

In two cases, parent ion peak is only having a single energy distribution. The 2D correlation diagram was rich in information particularly for dehydrogenation and $C_2H_2$ loss channels. They have very special features like tail (bands) connecting adjacent masses and spread towards lower kinetic energies. An intricate *Monte Carlo* (MC) simulation was carried out to understand the implications of various 2D features observed for different fragment masses. In the simulation, the complete trajectory of parent ion was reproduced for the electric and geometric configurations of the spectrometer by randomizing the dissociation for a particular decay rate. Initially, we eliminated the possibilities of energy spread by assigning zero spread in initial position and thermal velocity in such a way that possible energy or ToF spread can come in 2D due to the

dissociation occurring at various stages of the flight. The details of the MC simulation is explained for H loss fragmentation channel of fluorene$^+$ in the section 3.2.3.

### 3.2.3 Details of the MC simulation

The transit time and trajectory of parent ion inside extraction, acceleration fields, FD tube and PPA is simulated by solving differential equations of motions numerically for a time step of 10 ps for the full geometric configuration of the spectrometer. The time step is decided by the computational limits of the numerical calculations and the smallest random number that can be generated. Decay is handled by doing MC simulation for assigned decay rate in each time step. Once decay of parent ion is established, rest of the trajectory and flight time calculation is carried out analytically for daughter ion. Decay inside linear part (extraction, acceleration and drift tube regions) of the spectrometer can be easily handled. But decay in the 2D plane of PPA has to be done carefully, because flying daughter ions will be deflected to a new parabolic trajectory depending on its mass, location and velocity component of parent ion at the time of fragmentation. Therefore, if fragmentation occurs inside PPA, the fragment ion will fly along a new parabolic trajectory. We have estimated the range of horizontal deflection of each particles inside PPA using analytical equations and numerical methods, or both whichever is suitable for the context of fragmentation.

### 3.2.4 Results of MC simulation with zero spread in initial parameters

The simulation results of H loss of fluorene$^+$ with multiple decay constants ($10^4$–$10^7$ s$^{-1}$) are combined and plotted in figure 3.10. H loss fragment ions are seen to occupy different regions of the 2D spectrum depending on the region where the dissociation would have occurred during the flight.

Since the spreads in initial parameters are zero, we expected parent and fragment peaks will come with no spread in 2D correlation plot. As expected, undissociated parent peak appeared as a peak with no spread. But H loss fragment ions recorded in the simulation were occupying different region of the 2D plot depending on the location where they have formed. For the present experimental conditions, ToF of fluorene$^+$ is about 26.35 $\mu$s. It spends about 400–500 ns in the extraction region. Thus, if the decay constant lies between $10^6$ and $10^7$ s$^{-1}$, it will form a H-loss

peak with almost full energy as shown in the region "a" of figure 3.10. This decay is very close to prompt fragmentation. The substructure seen in region "a" pertains to finer decay dynamics in the ER. The second gap is the acceleration region and any decay in this zone will be seen as the
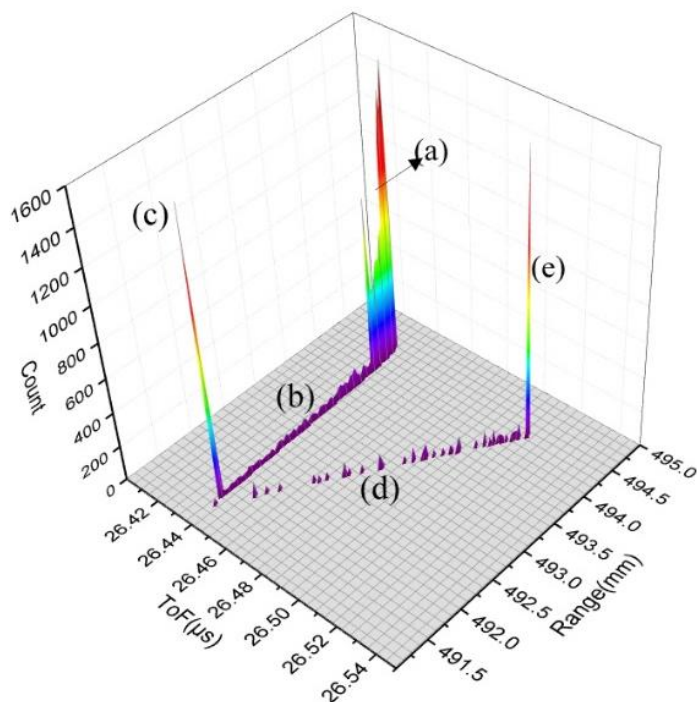


Figure 3-10: 3D colour map of ToF-Range diagram simulated by assigning zero spread for initial position and velocity of parent ion. This spectrum is simulated for multiple k values ($10^4$–$10^7$ s$^{-1}$). (a) high energy H loss fragment ion formed in the extraction region, (b) low energy H loss fragment ion produced in the acceleration phase, (c) low energy H loss fragment produced in the field free drift tube, (d) H loss decay inside parallel plate, and (e) unfragmented parent ion.

region "b." This is visualized in the 3D map as a bridge connecting prompt fragmentation and the peak in region "c". Region "c" is the peak corresponding to decay inside the field free drift tube, which demands that the decay constant should be of the order of $10^4$–$10^6$ s$^{-1}$. A line connecting low energy fragment and parent ion represents decay inside the parallel plate, which is shown in the region "d". Inside the parallel plate, the particle is continuously decelerating due to the strong repelling field. All the parent ions have a common trajectory. If a parent ion loses neutral fragment inside PPA, it deviates from the original path and follows a new and short trajectory depending on its current position and velocity conditions. The unfragmented parent ion (region "e") completes the original path, which covers a maximum horizontal distance and hence, the longest range. Therefore, the range of parent ion is the maximum limit any ion

can have. Those ions that dissociate inside the FD enter into the analyzer with the lowest KE and are deflected to the shortest trajectory. In ToF-KE spectrum, the ions fragmenting inside the parallel plate connects the low energy fragment ion and full energy parent ion with a straight line in the 2D diagram.

### 3.2.5  The MC simulation with finite spread in initial parameters

For a realistic comparison of experimental data, we must include all experimental artefacts and spreads in the MC simulations. Hence, the initial position and velocity of the ions are sampled from a Gaussian distribution generated by standard Box–Muller transform. This helps to generate initial values of position and velocity of ions from a Gaussian distribution with mean value $\mu$ and variance $\sigma^2$. The width of position distribution is assigned to be 50µm, to match with the estimated laser beam size along the direction of the extraction field, whereas the velocity spread is modelled using a directional thermal distribution with a width of 300m/s .This is because the geometric restrictions of the setup make the effects of other velocity components negligible. The MC code used to simulate the trajectory of parent ion implementing distributions of initial parameters is given in appendix A. The spectrum of the ToF and the horizontal range simulated for parent and fragment ions are in good agreement with the experimental measurements. The width of the parent ion peak observed in the ToF data of fluorene was 10 ns, which was reproduced in the simulation as well.

The ToF-range spectra simulated for various decay constants (k) along with a typical experimental 2D spectrum are shown in figure 3.11. The simulated ToF-range spectra are given in figure 3.11(a)–(f). The spectrum simulated for k = 100 s$^{-1}$ is given in figure 3.11(a). In this case, only the fluorene parent ion is present since the inverse of the decay constant is very long compared to the ToF of parent ion. The 2D plot shown in figure 3.11(b) is simulated for k = 1000 s$^{-1}$, with an average decay time of 1ms. This decay is slightly faster than the earlier one implying the finite probability of detecting fragment ions produced during the flight. Still the average decay time is 1 ms, which is far away from the ToF of parent ion. Therefore, the parent ion is dominating in the 2D plot though there are small number of events with decay inside FD and PPA.

For $k = 10^4$ s$^{-1}$ (see figure. 3.11(c)), the population of H loss regions is seen to be increased and the fragmentation is mainly located at the FD tube and PPA sections. As explained earlier, a thick belt is formed connecting low energy H loss fragment and parent ion, representing substantial fraction of decay inside PPA. Even the fast decays (decay inside extraction or acceleration regions) starts contributing to this particular decay rate. At $k = 10^5$ s$^{-1}$, with a mean decay time of 10 $\mu$s, which is about half of the parental ToF, the fragmentation is mainly located in the FD exit and the PPA sections. Therefore, the low energy H loss peak corresponding to FD decay and the belt region corresponding to PPA decay is densely populated (see figure 3.11(d)). In this decay time scale, there is a considerable possibility of fast decay. The H loss decay inside AR and even in the ER is observed, as shown in figure 3.11(d). Hence, for $k > 10^5$ s$^{-1}$, a large fraction of H loss decay occurs within the time window available to the spectrometer.
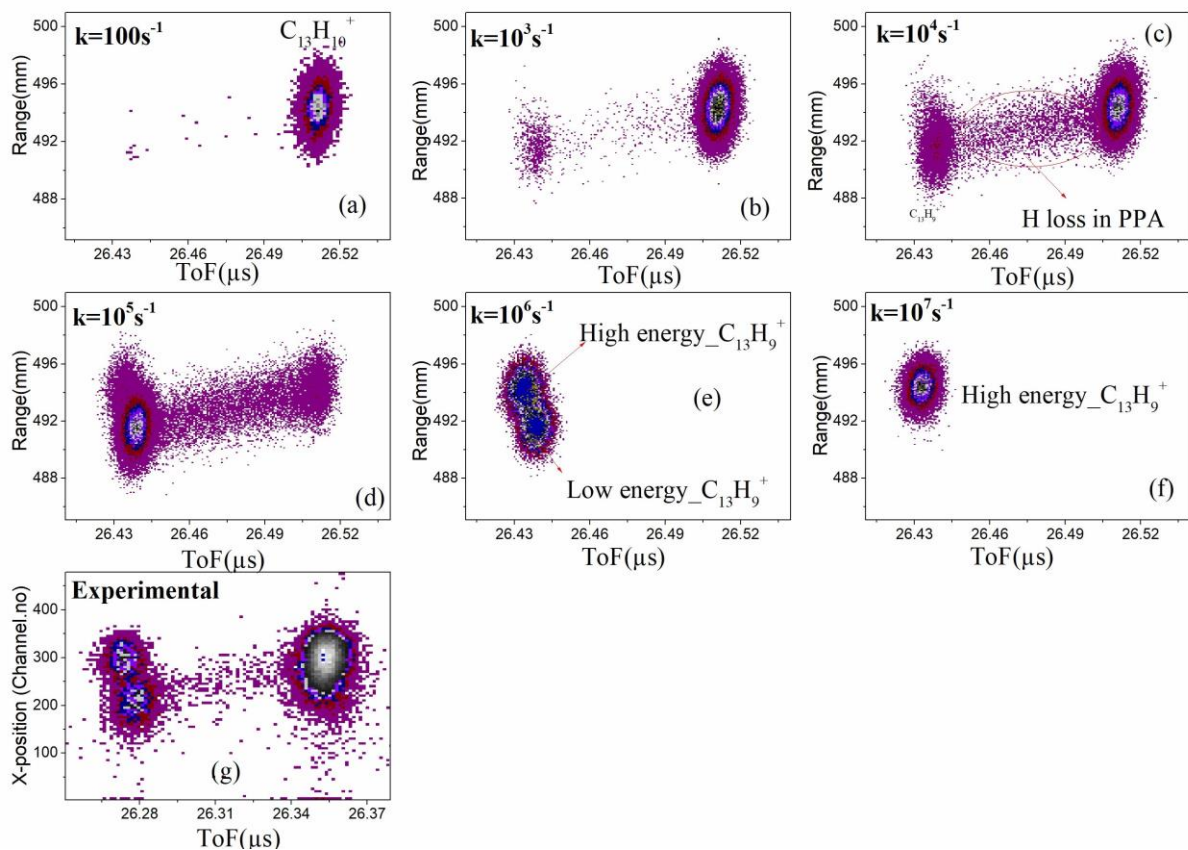


Figure 3-11: The ToF-range spectrum simulated for (a) k = 100 s$^{-1}$, (b) k = 1000 s$^{-1}$, (c) k = $10^4$ s$^{-1}$, (d) k = $10^5$ s$^{-1}$, (e) k = $10^6$ s$^{-1}$, (f) k = $10^7$ s$^{-1}$ for the experimental conditions, and (g) typical experimental 2D spectrum recorded for H loss channel of parent ion.

Faster decays are simulated with $k = 10^6$ s$^{-1}$ and $10^7$ s$^{-1}$, which are shown in figure 3.11(e) and 3.11(f), respectively. All the particles recorded in these two cases are H loss fragment ions, which is obvious due to short decay time assignments. For the former case, parent ion could be fragmenting just inside the drift tube, because as per electric field and mechanical configurations, fluorene ion takes about 700 ns to leave the AR. The decay in the ER and AR can also contribute to an average decay time of 1 μs. For this decay time period, the parent ion reaches the junction between acceleration and drift tube sections in which decays could be equipartitioned between the two regions. Therefore, top and bottom peaks in the ToF-range spectrum, representing fast and slow H loss decays, are almost equally populated for a k value of $10^6$ s$^{-1}$, as shown in figure 3.11(e). On the other hand, for the decay corresponding to k = $10^7$ s$^{-1}$ (see figure. 3.11(f)), only fast decay products (top peak) are visible. A typical 2D spectrum plotted using experimental data recorded for fluorene at 263 nm, with an average pulse energy of 10μJ is shown in figure 3.11(g).

### 3.2.6    Comparison of MC simulation results with experimental data

The 2D coincidence map for H loss channel of fluorene at 263nm is featured by full or high energy "fast H loss peak", low energy "slow H loss peak" and very weakly populated tail region connecting slow H loss peak and parent peak (see figure 3.12 (a)). The 2D coincidence pattern of the H loss channel measured in the experiment is reproduced in the simulation by combining two data generated at k=$10^6$ s$^{-1}$ and k=$10^3$ s$^{-1}$. This is shown in figure 3.12 (b).

It is very clear that two types of decay are involved in the experiment. Slow fragmentation populates parent peak and tail part. And, fast or microsecond range fragmentation populates two of the H loss fragment peaks. From the laser intensity dependence (see sec. 3.2), it has already been established that the 2-photon process produces the parent fluorene ion yield and 3-photon absorption produces H loss fragment ion yield. The Ionization energy of fluorene is 7.56 eV[30]. Therefore, ionization and very slow H loss can happen from 2-photon absorption at 263nm. The appearance energy of H-loss fragment ion in a single VUV photon ionization experiment of fluorene is about 12 eV[51]. Therefore, fast or microsecond H loss decay can definitely be expected from 3-photon absorption at 263nm.
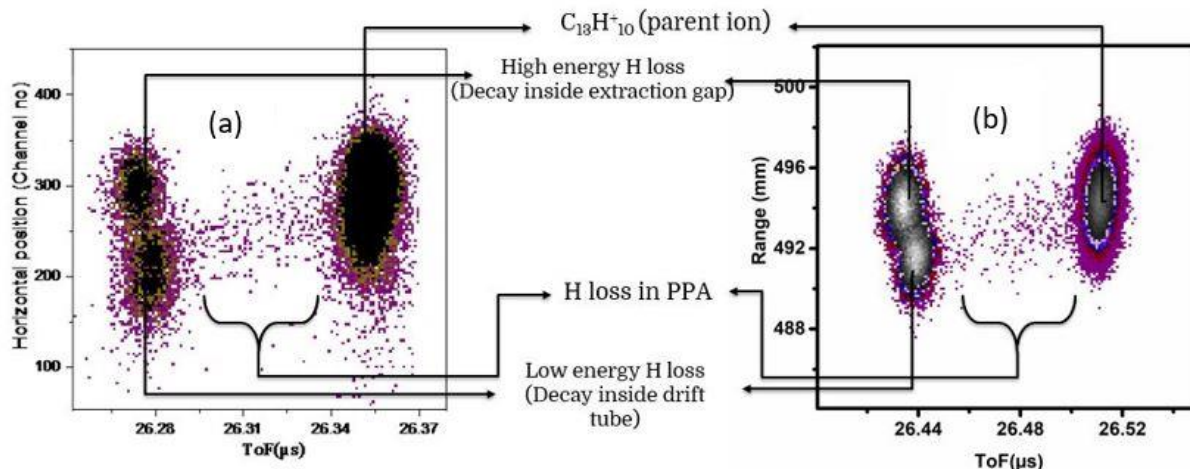
Figure 3-12: (a) 2D coincidence plot of fluorene measured at 263nm for an average pulse energy of 10 μJ, (b) 2D coincidence spectrum simulated for fluorene for two rate constants $k=10^3 s^{-1}$ and $k=10^6 s^{-1}$.

### 3.2.7 Range spectrum of H loss decay for a range of wavelength

Every populated region in the 2D graph points to a narrow or wide range of decay constants. If there is a large spread in decay constant, 2D landscape would be very complex. If only a selected region is populated, it directly implies a relatively narrow range of decay constants and hence, very narrow range of internal energy distribution (IED). It also appears that H loss populated area is eventually shifting for a change in excitation wavelength. It is demonstrated with the help of the horizontal range distribution of H loss fragment ion with respect to excitation wavelength (see figure 3.13).

It should be noted that the range of decay constant has to be really narrow to cause such an apparent and systematic shift in the H loss population as a function of wavelength. This implies that molecular ions are produced with a very narrow IED in the 3-photon excitation processes. It will be discussed in detail in the following chapters.

60
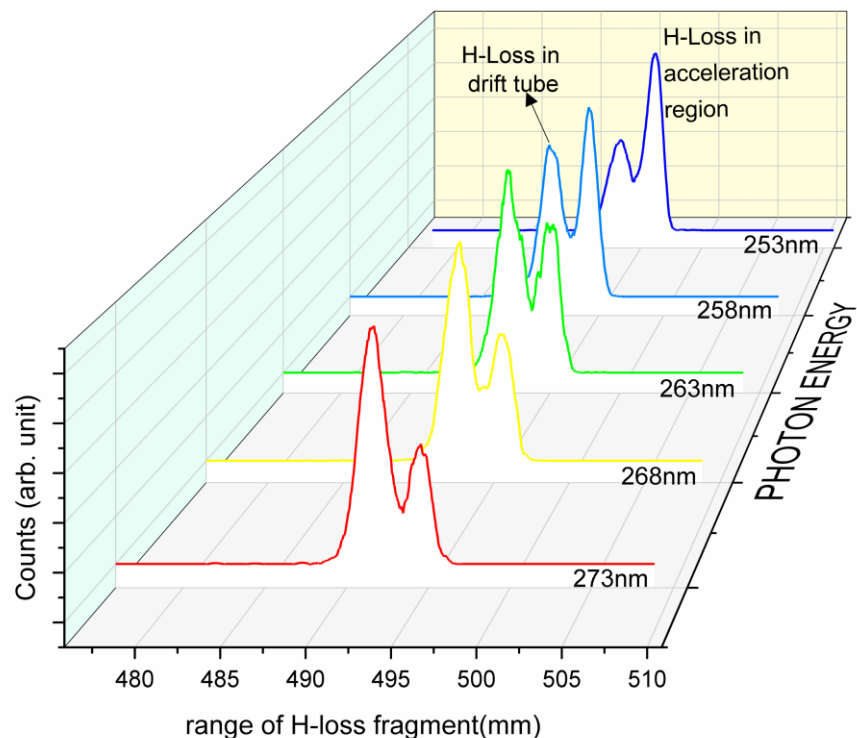
Figure 3-13: Distribution of H loss fragment ion along horizontal axis of PPA for 253-273nm.

3.2.8      Evaluation of H loss rate constants

The relative yield between fast H loss peak and slow H loss peak or tail and slow H loss peak (whichever is highly populated) can be reproduced in the simulation by assigning an appropriate decay constant in the MC simulation. For example, in case of the fluorene data at 263nm, the tail region is very sparsely populated as shown in figure 3.12(a). Therefore, we reproduced the relative yield between slow and fast H loss peaks along the horizontal range in the simulation for a decay rate of $7.5 \times 10^5 \, \text{s}^{-1}$ (See figure 3.14).

The 2D coincidence map of the H loss channel of fluorene$^+$ measured at 293nm is shown in figure 3.15(b). The main features of the H loss coincidence pattern of fluorene at 293 nm are a very strong fast H loss peak followed by a very weak slow H loss peak and tail band. It was clearly identified that in case of fluorene at 263nm, the H loss process is driven by 3-photon

61

absorption. Such a clear *n*-photon process is not identified for the H loss channel of fluorene at 293 nm. This implies that a
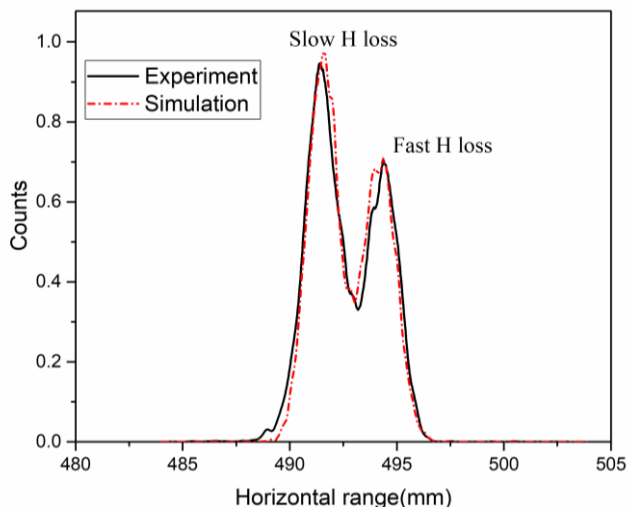


Figure 3-14: The distribution of H loss fragment ions along horizontal range is measured in the experiment for fluorene at 263nm. It is reproduced in the simulation for a decay constant of $k = 7.5 \times 10^5$ s$^{-1}$.

significant fraction of the H loss fragment ions could be produced from a higher order photon process at 293 nm (more than 3-photon). This can strongly populate fast H loss peak as observed in the 2D coincidence pattern (see figure 3.15(b)). The H loss fragment ion produced from 3-photon absorption can become very slow at 293 nm and can weakly populate the slow H loss peak and tail band. A very broad internal energy ensemble has to be expected if we consider H loss from multiple excitation process in terms of photon number. Therefore, we consider H loss from a single, 3-photon excitation process. In case of slow H loss dissociation from a 3-photon process, the decay rate is identified from the relative population of tail region in comparison to the slow H loss yield. The measured relative yield of tail with respect to slow H loss yield is reproduced in the simulation for a decay rate of $10^4$ s$^{-1}$. It may be noted that tail region can also be contaminated from collision induced dissociation at the used level of background pressure. It can influence the relative yield of tail and hence, the decay rate measurement.
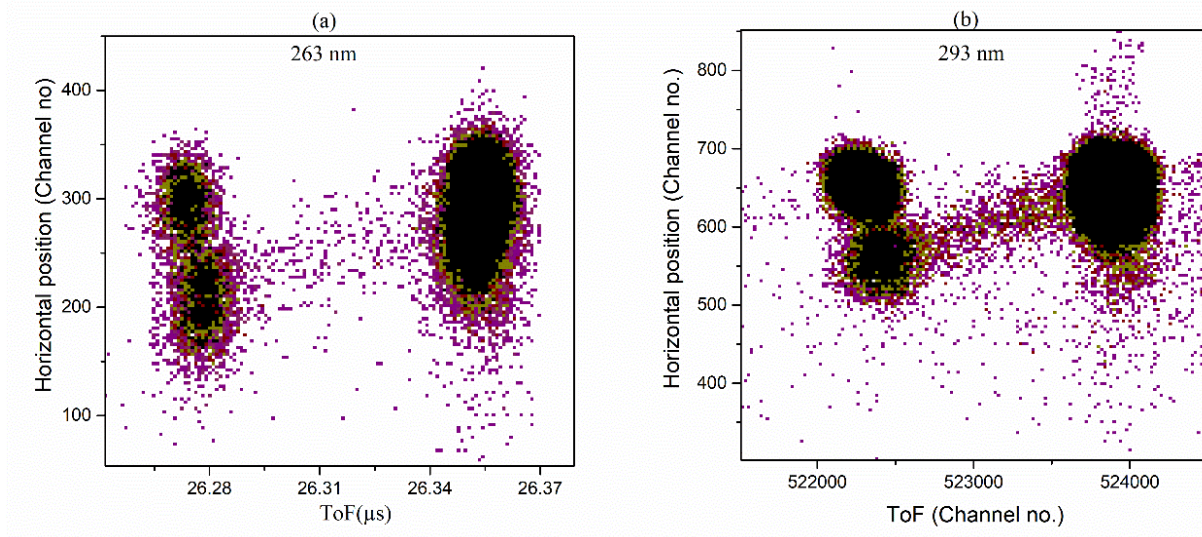
Figure 3-15: 2D coincidence pattern of the H loss channel measured for fluorene at (a) 263 nm and (b) 293 nm.

### 3.2.9     2D coincidence pattern: $C_2H_2$ loss channel

The 2D coincidence pattern of $C_2H_2$ loss of azulene$^+$ measured at 235 nm with an average pulse energy of 10 μJ is shown in figure 3.16 (a). There is a long tail starting from the full energy $C_2H_2$ loss peak and extending in the direction of decreasing kinetic energy. The 2D data is simulated with multiple decay constants in order to obtain all the possible decay features of $C_2H_2$ loss from azulene$^+$ as shown in the figure 3.16 (b). Since the acetylene is a heavy fragment, it can carry maximum kinetic energy (KE) proportional to its mass. A residual fragment ion loses a large fraction of the KE if it is fragmented just before or after full acceleration. Such fragment ions are deflected into a shorter parabolic trajectories and miss the detection by the position sensitive detector. Hence, our present 2D measurement may lose the information about slow acetylene loss happening just before or after full acceleration. But the fast decay, i.e decay during extraction and acceleration can be studied from the 2D coincidence pattern measured in the present experiment. It is shown in the figure 3.16 (b).
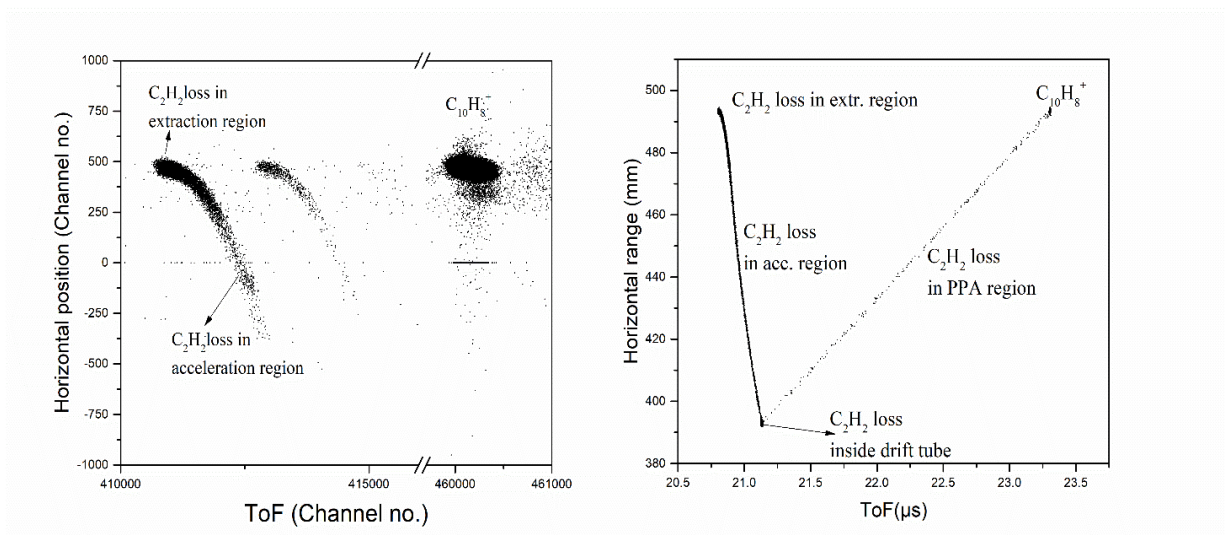
Figure 3-16: (a) 2D coincidence map measured for acetylene loss channel of azulene for 235nm, (b) 2D map simulated with multiple decay constants to obtain all the possible decay features of $C_2H_2$ loss from azulene$^+$.

### 3.2.10   2D coincidence pattern: $H_2/2H$ loss channel

A unique capability of this coincidence technique is that it can distinguish between sequential hydrogen loss (2H loss) and molecular $H_2$ loss. It can be recognized from the 2D pattern of the 2H and $H_2$ loss channels. The possible coinicidence patterns of sequential H loss were reproduced in the simulation by randomizing H loss decay twice in the MC code. The details are given in the following section

### 3.2.10.1    MC simulation for sequential H loss

The sequential H loss decay is handled in the present MC programm by repeating the simulation for second H loss with a newer rate constant after the first H loss decay. If two successive decays are completed, the rest of the trajectory and flight time calculation is carried out for the daughter ion analytically. The 2D coincidence maps were simulated for different sequential H loss processes to see all the possible decay features. This is demonstrated in case of azulene as shown in the figure 3.17 & 3.18 .
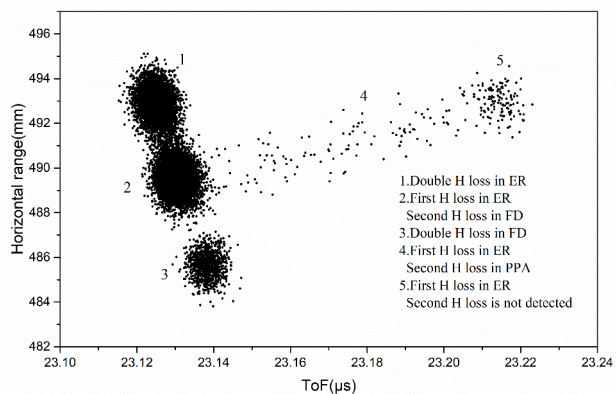
Figure 3-17: 2D coincidence map simulated with multiple sequential H loss rates to obtain all the possible decay features of 2H loss from azulene$^+$.
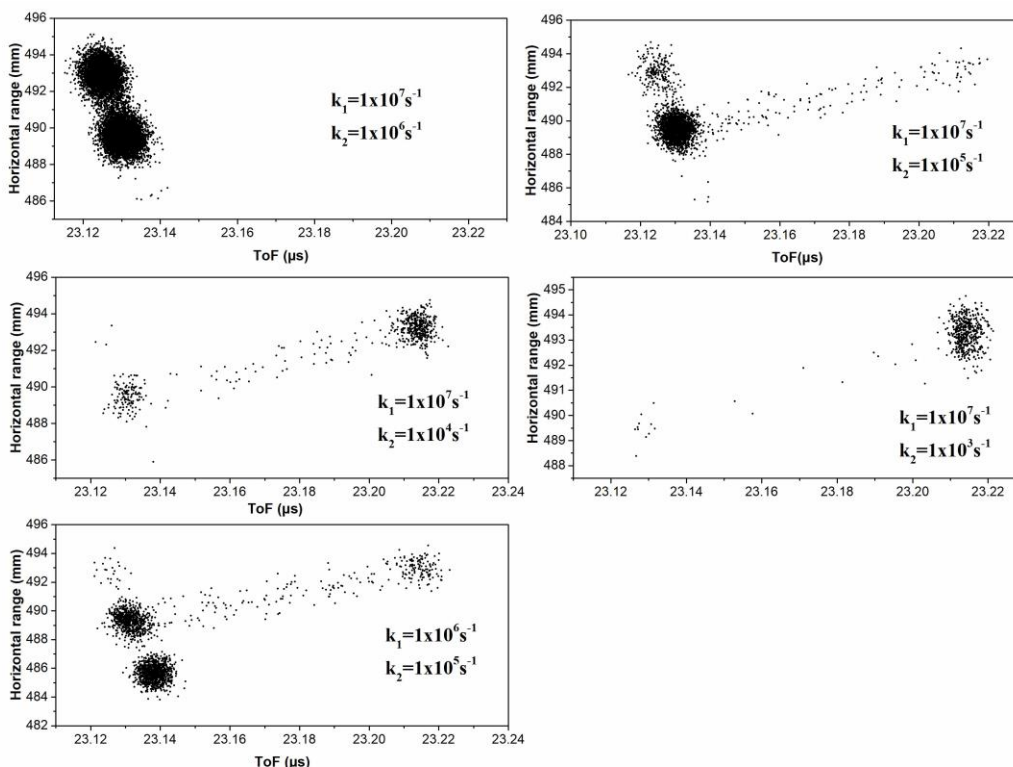


Figure 3-18: 2D coincidence map simulated for sequential H loss decay of azulene with $k_1$ as the first H loss decay rate and $k_2$ as the second H loss decay rate

3.2.10.2    2D coincidence pattern: $H_2$/2H loss channel of azulene at 280 nm

The coincidence pattern of single and double H loss measured for azulene at 280 nm is shown in figure 3.19. The laser intensity dependence of fragmentation yield at $m/q=127$ and $m/q=126$ were   showed that these were 4-photon processes. It was discernable from the 2D coincidence pattern that two types of decays were involved in the fragmentation peak at $m/q=126$. The sequential H loss decay (with $k_1= 10^7$-$10^8$ s$^{-1}$ and $k_2=10^4$-$10^3$ s$^{-1}$, suggested by possible coincidence patterns simulated for 2H loss) and very fast $H_2$ loss decay (with $k=10^7$-$10^8$ s$^{-1}$).
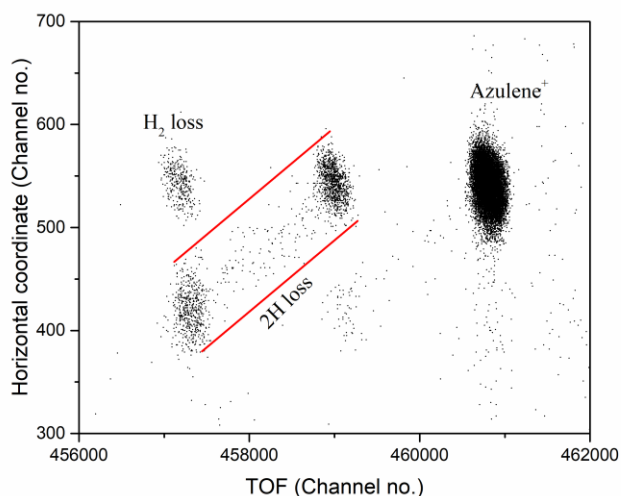


Figure 3-19: 2D coincidence pattern of $H_2$/2H loss channels of azulene measured at 280nm

3.2.10.3    2D coincidence pattern: $H_2$/2H loss channel of naphthalene at 225 nm

The 2D coincidence map measured for dehydrogenation channels of naphthalene at 225nm is shown in figure 3.20. The laser dependency of fragmentation yield at $m/q=127$ and 126 showed that, these were 3-photon processes. The possible 2D pattern of sequential H loss was completely missing in the 3-photon process at 225nm. Therefore, the fragmentation at $m/q=126$ is a single type, $H_2$ loss, with rate constant of $k=10^6$s$^{-1}$. It was clear from the primary analysis that $H_2$ loss was the favorable channel at 3-photon excitations and sequential H loss can dominate at high energy excitations due to higher order photon processes.
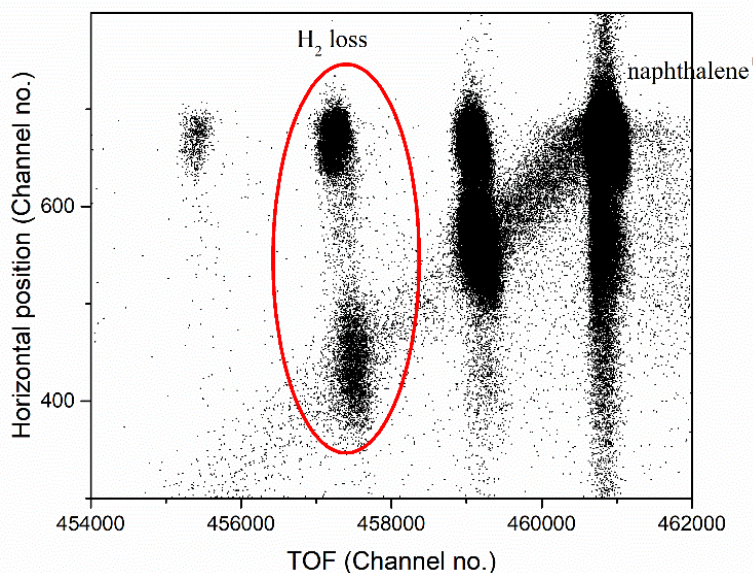
Figure 3-20: 2D coincidence pattern of $H_2$ loss channels measured for naphthalene at 225nm.

## 3.3    Summary

The data acquired using a non-conventional ToFMS is usually multidimensional. When we perform data analysis, the quality of data can be improved by putting specific conditions in terms of coincidence, matching and timing etc. Here the entire experimental work is done based on timing of nanosecond order pulses with picosecond accuracy, finally the information is converted into mass, change in kinetic energy, decay time details etc. The recorded raw data is converted to physically useful information with the help of a complex data reduction and analysis procedure. For example, here we have used coincidence as the data reduction logic for proton-PAH collision.

This analyzed data is separately checked with collisional theories. But in case of energy correlated ToF technique, the data analysis itself is done with the help of a simulation. Very advanced platforms and tools like ROOT, C++ were used for data reduction and analysis. Thus, the analysis described here ends up in giving a lot of useful details or predictions like detection efficiencies, relative cross section/intensities of reaction/fragmentation channels, structures of intermediate and product ions and decay time details of dissociation process etc. These results are then converted into useful physics information about the molecules with the help of physics models or comparison with theory. This is elaborated in the coming chapters.

# CHAPTER 4. PLASMON MEDIATIED ISOMERIZATION IN PAHS

## 4.1    Introduction

The ion-molecule collision process is well understood and well-studied for various molecules. In such collisions, two aspects dominate the energy loss mechanism, namely, the cross section of energy loss and the amount of energy loss by the projectile. Considering the Coulombic nature of the interaction, the energy deposition is very strongly dependent on the projectile velocity and impact parameter. Thus, the ionic particle deposits a very broad distribution of energies and this distribution changes very rapidly as a function of projectile velocity[52–55]. PAHs are also expected to experience the same energy deposition as other molecules[48,52,53] but ion-PAH collisions are known to be dominated by the collective excitations[47]. It offers a unique mechanism which leads to a constant but broad energy deposition (typically width of plasmon resonance for PAHs is about 7-8 eV) to the target irrespective of the projectile velocity[21,47,56]. The average energy of this excitation can often be much larger than the first ionization potential of the target molecule[57]. Like any conventional energy loss mechanism in ion-molecule collisions, the cross section of plasmon excitation is influenced by the projectile velocity[47]. The main feature of this excitation is the constant energy loss, weakly dependent on projectile velocity. This behavior in conjunction with large excitation cross sections (due to generalized oscillator strength much greater than one)[17] implies that collective excitation in ion-PAH collisions can be made used to assess various excited state dynamics of PAH cations.

The average energy loss of plasmon excitation in PAHs is 16-17eV[22]. It has already been demonstrated  that the plasmon excitation involves the coupling of the deposited energy to the

inner valence electron and the electron can be ejected with very minimal kinetic energy[23]. Therefore, the PAH cations are produced in an excited electronic state and the excess electronic energy is converted to internal energy by an ultrafast IC. It will result in a fast IVR and statistical dissociation. This dissociation process can proceed over tens of microseconds for the available internal energy expected from plasmon excitation. The main purpose of this work was to investigate plasmon mediated dissociation in azulene ($C_{10}H_8$) and naphthalene ($C_{10}H_8$) while interacting with a fast proton beam (50keV-150keV). The details of experimental setup are given in sec 2.4 of chapter 2 and data reduction and analysis procedures are explained in sec 3.1 of chapter 3.

The work reported in this chapters is twofold. First, to understand how the plasmon excitation affects the two isomers and second, to look for evidences of higher order plasmon excitation process. Since the amount of energy deposited is known, the interpretation of the possible effect is expected to be simple.

## 4.2    Analysis and discussions

A typical mass spectrum obtained for azulene and naphthalene in EC mode under 75keV proton impact is shown in figure. 4.1. Each spectrum exhibits singly and multiply charged parent ions $C_{10}H_8^{q+}$ (q=1, 2, 3), their evaporation products (H/$H_2$ or 2H/$C_2H_2$ loss) and energetic fragment ions of lower masses. Some of the impurity peaks like $H_2O^+$ from the background, $Ar^+$ at $m/q$=40 and $Ar^{2+}$ at $m/q$=20 are also present (Ar gas was used for calibration) in all the mass spectra. Single ionization is the prominent channel which is followed by double ionization. $C_{10}H_8^{3+}$ peak is observed with negligible yield as compared to single and double ionization peaks. The evaporation channels, being gentle fragmentation pathways (as the associated momentum release is negligible) manifest as narrow peaks. $C_{10}H_7^+$ (H loss), $C_{10}H_6^+$ (2H/$H_2$ loss) and $C_8H_6^+$ ($C_2H_2$ loss) are the main evaporation products of $C_{10}H_8^+$, which appears at $m/q$=127,126,102 respectively. These represent low energy fragmentation channels of PAHs. In the dication region ($m/q$=64) large intensity narrow peaks are blended with broader peaks. The former represents dication species while the broad peaks are singly charged mass fragments. The dominant dication dissociation products are $C_{10}H_6^{2+}$ (2H/$H_2$ loss), $C_8H_6^{2+}$ ($C_2H_2$ loss) at $m/q$ = 63 and 51, respectively. In contrast to the monocation decay, we discern that the 2H/$H_2$ loss is dominant

unlike the H loss that is quiescent. This cannot be explained by any conventional energy loss mechanism associated with the ion-molecule collision. We attempt to explain this by invoking the plasmon model. This is discussed later in Sec 4.8. Various broad peaks of fragment ions $C_mH_n^+$ (0 < m < 9, n is uncertain) are visible in the mass spectrum. They can be produced by energetic fragmentation of multiply charged parent species. The excess kinetic energy released in the process broadens the mass spectrum. For estimating the area associated with each high intensity narrow peak the contribution from the broader background peaks is carefully subtracted. The mass spectral resolution in the EC mode is superior to that in the electron emission (EE) mode. This is because there is a jitter in the start trigger of the EE mode due a spread in energy and direction of the emitted electrons.
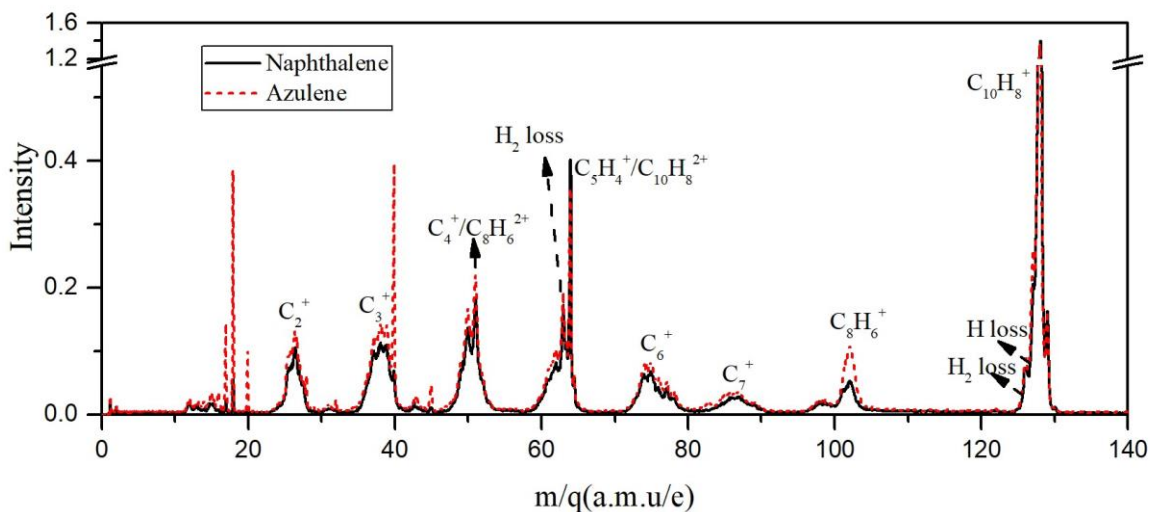


Figure 4-1: Mass spectrum for 75-keV proton energy in EC mode showing monocation and dication evaporative products and energetic fragment ions for azulene (dashed line) and naphthalene (continuous line). Axis breaks should be noted.

The similarity between the mass spectra of azulene and naphthalene is noteworthy. Considering the structural difference in the two molecules, one can expect very different yields of the fragments even if identical internal energy is deposited. Almost identical fragment yields are obtained except at the $C_2H_2$ loss peak. There is an apparent non-similarity with the intact dication and associated $2H/H_2$ and $C_2H_2$ loss peaks which as shown later, also happens to have some underlining quantitative similarity. Most significantly the masses between 95 to 100 a.m.u

are exactly overlapping in the two targets but the peak at $m/q$=102 is drastically different. These very primitive observations directed us to look for possible role of isomerization provided one can explain the origin of specific points like excess acetylene loss of azulene[+] in comparison to naphthalene[+].

## 4.3    Electron emission and electron transfer cross sections in intermediate proton-PAH collisions

It was important to understand the excitation mechanisms of the two molecules, before comparing their specific dissociation channels. Therefore, we tried to check whether the relative cross sections of electron emission and electron capture processes are the same in the two molecules. If they are the same, then the relative enhancement of any dissociation channels would suggest internal dynamics of the molecule. On the other hand, if the relative cross sections of the two isomers are distinct, further comparison of fragmentation channels becomes laborious.

In the absence of absolute normalization, only the relative cross sections in EE and EC modes could be estimated using measured monocation intensities. Since EE and EC mode data were collected in OR mode, target and projectile densities were the same for the EE and EC processes. Hence, using the detection efficiencies of the emitted electron and neutralized projectile, the ratio of absolute cross sections could be obtained.  Figure 4.2 shows ratios of EE to EC cross sections for azulene and naphthalene as a function of proton energies. The figure demonstrates that these ratios vary in a manner that is identical for both the molecules within error bars. Major sources of error are the uncertainties in the electron and projectile detection efficiencies. 150 keV data had lower reliability due to very low capture cross sections.

The collective excitation is the dominant energy loss mechanism governing electron emission in PAHs for the investigated projectile velocity regime. It can be identical for both molecules. On the other hand, the electron capture cross section depends on several factors like velocity and binding energy matching conditions.  In naphthalene, it is observed that ionization and capture cross sections are changing differently in different directions in the studied proton energy region[47]. The change in the EE cross section is gradual in contrast to the case of the EC cross section that decreases rapidly as a function of proton energy. This implies that EE and EC

71

cross sections will evolve independently. Hence, it is highly unlikely that two different molecules have the same ratios of absolute cross sections unless their respective absolute values are equal. The two target molecules considered here are planar with identical bond nature and same hybridization, and they are likely to have very similar electron density distribution. Thus, it follows that the electronic energy loss mechanisms, which are solely a function of the electron
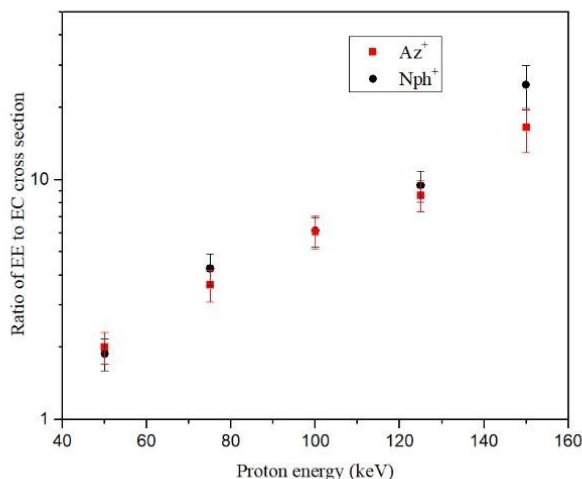


Figure 4-2: Ratio of EE to EC cross sections as a function of proton energy for azulene$^+$ (az$^+$) (solid circles) and naphthalene$^+$ (nph$^+$) (solid rectangle).

density distribution, are identical in the two molecules under consideration. Hence, the structural difference in azulene and naphthalene is a minor aspect as far as the electronic energy loss mechanism is concerned, however, later dynamics heavily depend on individual structures.

## 4.4    Low energy dissociation channels of azulene$^+$ and naphthalene$^+$ in EE and EC modes

The characteristic feature of fast proton- PAH collision is the production of large single ionization yield in µs timescales. H loss, $H_2$/2H loss and $C_2H_2$ loss channels are the major statistical dissociation processes of the parent ion. Therefore, their relative yields measured using a ToF spectrometer will only be dependent on the total energy content of the parent ion. In the case of EE mode data, the relative yield of $C_2H_2$ loss channel of azulene$^+$ and naphthalene$^+$ shows no dependence on impact energy, thereby implying a very similar excitation (see figure 4.3 (a)). It is an evidence of plasmon mediated ionization and dissociation of the molecules[47]. Conversely,

the relative yield of the $C_2H_2$ loss channel of azulene as well as naphthalene slowly decreases for an increase in proton velocity in EC mode. Although resonant or quasiresonant electron transfer is known to dominate in the EC mode, it is accompanied by small amount of localized electronic energy loss[47,48]. Energy transfer via localized electronic energy loss has been known to decrease for an increase in projectile velocity. This is corroborated with the behavior of the $C_2H_2$ loss channel being observed for an increase in impact energy. In EE as well as EC modes, the relative yield of acetylene loss is higher for azulene compared to naphthalene (See Fig. 4.3 (a), 4. 3(b)). Ostensibly, this indicates that the dissociation from azulene$^+$ is to a larger extent compared to naphthalene$^+$. The same approach was tried to expand to H and 2H/$H_2$ loss channels of isomeric monocations. But a quantitative collation of H/2H or $H_2$ loss channels was not possible for the target molecules as the fitted peaks had large uncertainties.
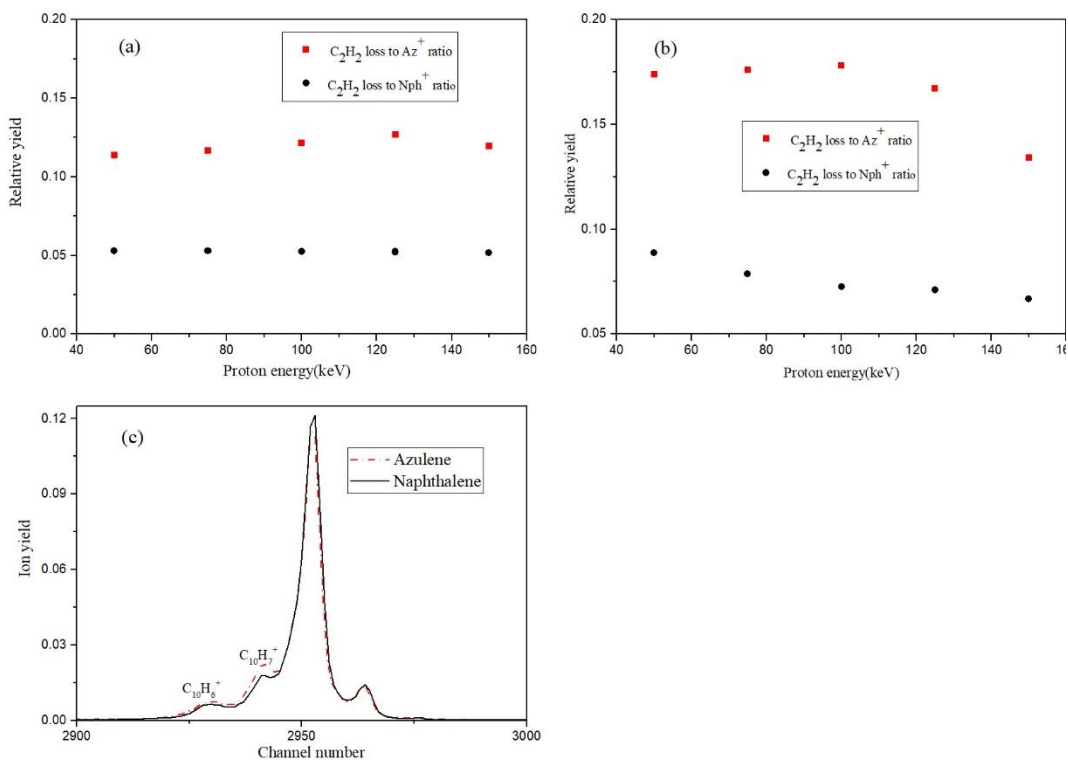


Figure 4-3: Proportion of $C_2H_2$ loss with respect to azulene$^+$ (solid square)/ naphthalene$^+$ (solid circle) in EE mode, (b) Proportion of $C_2H_2$ loss with respect to azulene$^+$ (solid square)/ naphthalene$^+$ (solid circle)

in EC mode, (c) Azulene$^+$ (dashed and dotted line)/naphthalene$^+$ (continuous line) peak showing better resolved (less resolved) H loss peak for azulene$^+$ (naphthalene$^+$).

A comparison of the relative yields of H, H$_2$, C$_2$H$_2$ loss species in EE and EC modes with the photodissociation break-down curves of naphthalene$^+$ by West *et al* [25], establishes that the internal energy of parent ion is needed to be around 8-11 eV in order to have a detectable dissociation yield at the microsecond time scale. Further, Gotkis *et al.*[27] have estimated the dissociation rate constants of naphthalene$^+$ for the H and C$_2$H$_2$ loss channels in this internal energy range. As the acetylene elimination is faster than H loss in the present internal energy regime, we anticipate that the loss of C$_2$H$_2$ occurs considerably within the acceleration region of the ToF spectrometer. Hence, the product ion is accelerated to maximum energy and appear as a clear peak in the mass spectrum. On the other hand, the dissociation time scale of H loss would be comparable to the time spent in the acceleration region leading to the respective product ion getting accelerated to lower energies and filling the valley between $m/q = 127$ and 128. Had this been due to poor resolution of the spectrometer, it would have affected the 2H/H$_2$ loss peak as well. On the contrary, we were able to fit the 2H/H$_2$ loss peak in spite of lower statistics. In case of the H loss peak in azulene, we find that it is resolved better in EE and EC modes as shown in figure. 4. 3(c). This could be attributed to higher decay constant of H loss in azulene$^+$ compared to naphthalene$^+$. All the aspects reinforce the fact that azulene$^+$ in general has higher decay constant compared to naphthalene$^+$. This can be explained by excess internal energy available to azulene$^+$ or the difference in the Arrhenius parameters or in combination of both.

## 4.5    Azulene$^+$ to naphthalene$^+$ rearrangement in EE mode

Collective excitation is the major energy transfer mechanism in PAHs in the studied proton impacts and a low energy electron is emitted as a result of autoionization[23,47]. The average energy retained in the molecular ion after autoionization is about 8-10eV which is converted to internal energy of the PAH ion by ultrafast IC. The molecular cation rapidly follows various reaction pathways at such high internal energies to be able to influence the microsecond time scale of ToF spectrum. In case of azulene$^+$ for the above mentioned internal energies, cationic rearrangement to naphthalene$^+$ is already reported[28,31,58].

To this end, Jochims *et al*[59] have applied thermal rearrangement schemes (Scott mechanism[60] and Dewar-Becker mechanism[61]) for neutral azulene and naphthalene to their ionic equivalents. Dewar and co-worker[61] have proposed that the Scott mechanism is a rather high energy pathway for neutral isomers. Hence, among the two schemes in a which neutral molecule isomerizes, Lifshitz *et al.*[58] have concentrated on the Dewar-Becker mechanisms for ionic systems and carried out DFT and coupled cluster calculations to figure out the potential energy profile of the ionic isomerization. They have suggested two interconversion pathways between azulene$^+$ and naphthalene$^+$ in which norcaradiene radical cation played a central role. Dykov *et al.*[28] have demonstrated the significance of norcaradiene-vinalydiene mechanisms (please refer section 3 of reference 28) among the six cationic rearrangement pathways between azulene$^+$ and naphthalene$^+$. The same authors have calculated the isomerization barrier energy to be ~3.1 eV for azulene$^+$ as it transforms to the stable isomeric ion naphthalene$^+$ through the norcaradiene-vinalydiene mechanism. In addition, they have proposed the isomerization energy to be around 0.8eV. Lifshitz *et al.*[58] have concluded that the isomerization barriers of the two alternate pathways lies below the dissociation limit of $C_2H_2$ loss (4.44ev) of azulene$^+$. Dykov *et al.*[28] have carried out an extensive calculations to determine isomerization and dissociation rate constants of azulene$^+$ and naphthalene$^+$ for a range of available internal energies (5-13eV).

The energetics of the present experiment compels to invoke isomerization processes. But the quantitative information can only be obtained from more energetically complete photodissociation studies. Lifshitz *et al*[31] have carried out a photodissociation experiment with $C_{10}H_8^+$ isomers and evidenced isomerization between them. They regulated the photon energies given to azulene$^+$ and naphthalene$^+$ in such a way that both the isomeric ions dissociate at the same rate. The difference in the photon energy given to the two isomeric ions was found to be equal to the predicted isomerization energy. A schematic diagram representing their energy scheme of isomerization is shown in figure.4.4. Unlike their experiment where the deposited energy was varied in order to keep the decay constant the same, we have no control over the deposited energy. In our experiment, the average energy loss associated with the plasmon excitation is 16-18eV. The ionization energy of azulene is about 0.8eV less than that of naphthalene[62]. Hence, it is possible for azulene$^+$ to have an available internal energy in the range of 8.6-9.6eV. But naphthalene$^+$ can have available energy in the range of 7.8-8.8eV. As per Dykov's RRKM calculations isomerization rate constants of azulene$^+$ to become naphthalene$^+$

would be $10^6$ to $10^8$ s$^{-1}$ and the reverse isomerization rate constants are of the order of one or two magnitude less for the available internal energies. The dissociation rate constants of azulene$^+$ and naphthalene$^+$ are calculated to be $10^5$-$10^7$ s$^{-1}$ by the same group for the same available internal
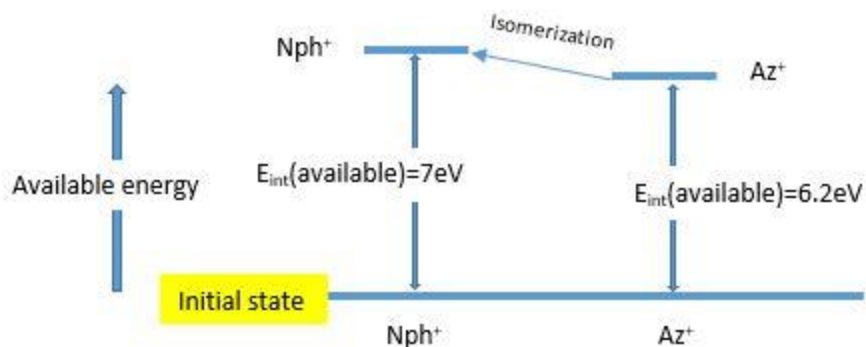


energies, which is rather slow compared to the rapid isomerization of parent ions[28].

Figure 4-4: Energetics of photodissociation studies carried out by Lifshitz *et al.*[31] for azulene$^+$ and naphthalene$^+$.

The slow dissociation of azulene$^+$ is appeared to be influenced by its fast isomerization dynamics. It is highly deductive that the isomerization process can invest excess internal energy to the azulene parent ion, which can speed up the later evaporation processes. Thus, the faster H/$C_2H_2$ loss of azulene$^+$ resulted in an excess yield of $C_8H_6^+$ or resolved $C_{10}H_7^+$ peak in the mass spectrum of azulene in comparison to that of naphthalene. We proposed complete energetics of ionization and isomerization following the plasmon decay of $C_{10}H_8$ isomers as shown in figure.4.5. The similar isomerization is likely to occur in other PAHs as well. In the photodissociation study of $C_{14}H_{10}^+$ isomers, Lifshitz *et al.*[63] have observed that the dissociation competes with the isomerization. Therefore, a clear effect of isomerization on dissociation process cannot be accessed in these isomeric PAH ions.
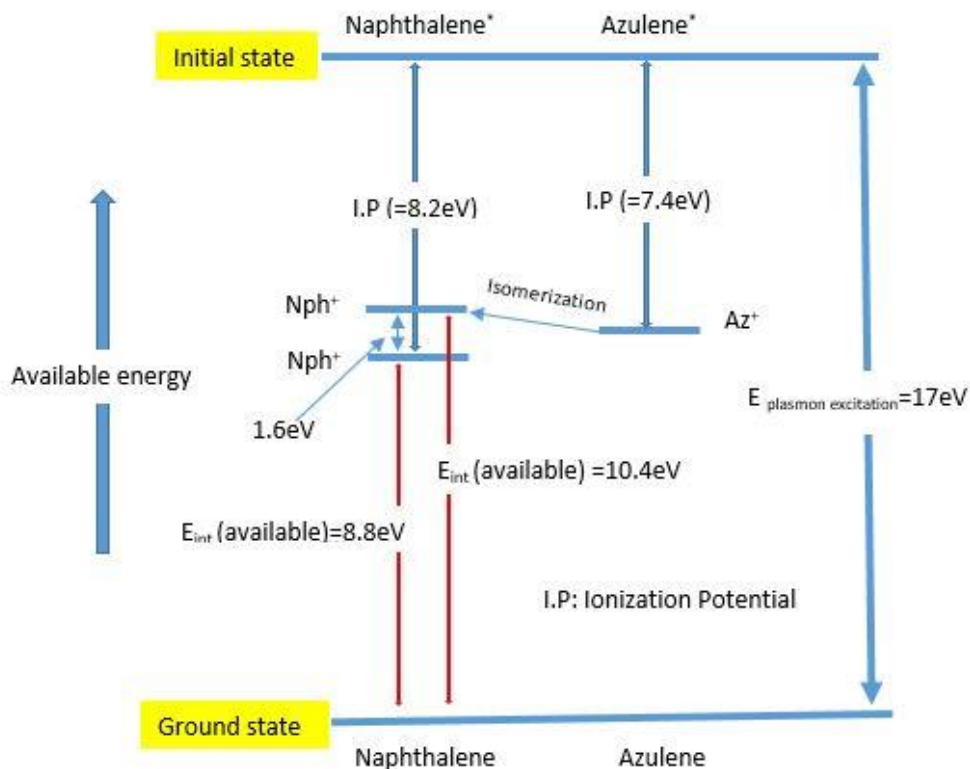
Figure 4-5: Schematic diagram showing energetics of plasmon excitation in naphthalene and azulene and deexcitation via ionization and various statistical processes. It is demonstrated that internal energy available for azulene[+] is about 1.6eV larger than that for naphthalene[+]

## 4.6    Double ionization of $C_{10}H_8$ isomers for EE mode

The intact dication and its neutral loss channels are observed to be superimposed on broad monocation fragments. The relative yield of intact dication and its neutral evaporation channels are measured by carefully subtracting monocation fragments from narrow dication peaks. This analysis was limited to EE mode since the statistics on dication products was insufficient in EC mode. The acetylene and 2H or $H_2$ eliminations are the relevant evaporation channels for $C_{10}H_8^{2+}$. The relative yields of dication and dication fragments were normalized with monocation yield are plotted separately for two targets as a function of proton energy as shown in figure. 4.6 (a) and 4.6 (b). Although the trend of fragment yield is similar in both the targets, their magnitudes are different. The relative yields of the dication species exhibit a decrease with increasing proton velocity for both the targets. Unlike the0020monocation, a doubly charged ion is produced when

a projectile encounter a target at lower impact parameters. Thus, double ionization cross section and energy loss can be very sensitive to proton velocities. However, when the intact dication and its fragment yields were added together, we find that the total yield is identical for both the targets at every energy, as can be seen from figure 4.6 (c). This signifies that the mechanisms by which the original dications are being generated in naphthalene and azulene are similar in terms of energy loss as well as cross sections. This demonstrates that the original excitation mechanism is equivalent in both the molecules.
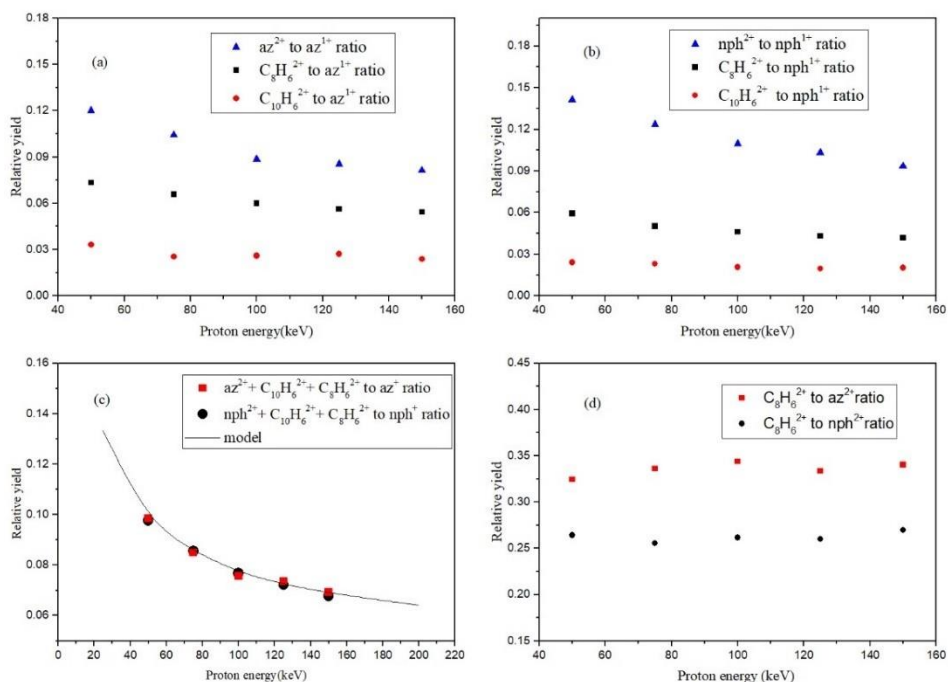


Figure 4-6: Proportion of (a) azulene$^{2+}$/$C_8H_6^{2+}$/$C_{10}H_6^{2+}$ with respect to azulene$^+$, (b) naphthalene$^{2+}$/$C_8H_6^{2+}$/$C_{10}H_6^{2+}$ with respect to naphthalene$^+$ in EE mode, (c) Proportion of total dication yield (including those which had decomposed in the acceleration region) with respect to respective monocation yield for azulene (solid square) and naphthalene (solid circle) in EE mode and double to single plasmon cross section is calculated using multiplasmon resonance model and shown as line plot, (d) Proportion of $C_2H_2$ loss of azulene$^{2+}$ (solid square)/naphthaalene$^{2+}$ (solid circle) with respect to their parent cation

It is discerned that the relative yield of $C_2H_2$ loss in comparison to total dication yield is constant over the studied projectile velocity regime as displayed in figure 4.6 (d). The similar trend is observed for 2H/H$_2$ loss channel as well. This demonstrates that original dications are

produced in a similar excitation mechanism for all the projectile velocities studied here. Plasmon assisted constant energy transfer mechanism has already been established for PAHs while interacting with fast protons. But it is very unlikely that single plasmon excitation causes double ionization in naphthalene, as it would require at least 21eV energy[62]. It is therefore, imperative to propose double plasmon model for double ionization of PAHs. This model is already been successfully applied to explain large single as well as double ionization cross section observed in fullerene in fast heavy ion collisions[20,21,56]. Here we have used double plasmon model to predict the double ionization cross section of naphthalene and azulene for a range of proton energies.

## 4.7 Plasmon excitation model to predict double ionization cross sections in PAHs

Plasmon excitation is known to play an important role in target molecules having high degree of electronic delocalization when interacting with fast ion beams. The plasmon excitation model is essentially a perturbation theory and it is valid only for distant collisions accompanying small momentum and energy transfer. For distant collisions, collision times will be large compared to the period of the excitation and the interaction becomes adiabatic. In adiabatic collisions, the target electrons can be treated as harmonically bound charges with a characteristic frequency $\omega$. The energy transfer, $\Delta E$ from a projectile ion with charge $Z_1e$ and velocity $v$ to a PAH target at an impact parameter $b$ is calculated by the dipole approximation[64] using the following expression.

$$\Delta E = \frac{2Z^2 e^4}{mv^2 b^2}\left[\xi K_1^2(\xi) + \frac{1}{\gamma}\xi^2 K_0^2(\xi)\right] \tag{4.1}$$

Where, $\xi = \frac{Eb}{\gamma\hbar v}$ and $K_0$ and $K_1$ are modified Bessel functions. The effective number of plasmon excitations at an impact parameter b is given by

$$N(b) = \int \frac{\Delta E\, f(\varepsilon)d\varepsilon}{\varepsilon} \tag{4.2}$$

Where, $\varepsilon = \hbar\omega$, is the plasmon excitation energy. In order to evaluate Eq.(4.2) we can approximate the oscillator-strength distribution $f(\varepsilon)$ as a Gaussian function normalized to reproduce the oscillator strength, the width, and other known parameters of the resonance. The integrated oscillator strength is approximted to be the total number of inner valence electrons of the target molecule, which is 40 for $C_{10}H_8$. The width of the plasmon resonance for PAHs is considered to be 7eV, which is obtained from the broad ionization peak observed at the plasmon resoncance using synchrotron radiation source[57].

The probability of excitation of plasmon to the $n^{th}$ state is

$$P_n(b) = \frac{[N(b)]^n exp[-N(b)]}{n!} \tag{4.3}$$

And finally the cross section of plasmon excitation to the $n^{th}$ state is given by,

$$\sigma_n = 2\pi \int b P_n(b) db \tag{4.4}$$

We have estimated double to single plasmon cross section for all proton velocities and it is compared with the double to single ionization yield measured in the experiment. It is given in figure 4.6(c). The calculated cross section of double plasmon excitation matches very well with the relative cross section of double ionization observed in the experiment. Hence, the second ionization of $C_{10}H_8$ due to the double plasmon resonance would be feasible and certain energy ($\approx$13eV) could be left to the molecule for further dissociation. Though in the present work we have no quantitative measure of energetics of plasmon excitation, we investigated if such a model is invoked what all possible secondary effects the target molecule would have experienced. One such effect is discussed in the next section.

## 4.8     Double plasmon energetics and dissociation channels of the dication

As mentioned earlier, H loss is completely suppressed in the decay of $C_{10}H_8^{2+}$ (See figure. 4.7). Holm $et\ al.$[65] have calculated dissociation energies for neutral losses as a function of charge state

of the parent ion for five PAHs including naphthalene. The dissociation energies for neutral losses remain nearly constant with respect to the charge state of the parent ion. Applying their result to the present work, the monocation and dication dissociation energies for neutral loss are expected to be equivalent. In photoionization break down curves for naphthalene[+], West *et al.*[25] have observed that H loss completely falls off at photon energy around 21eV, and here onwards $2H/H_2$ loss
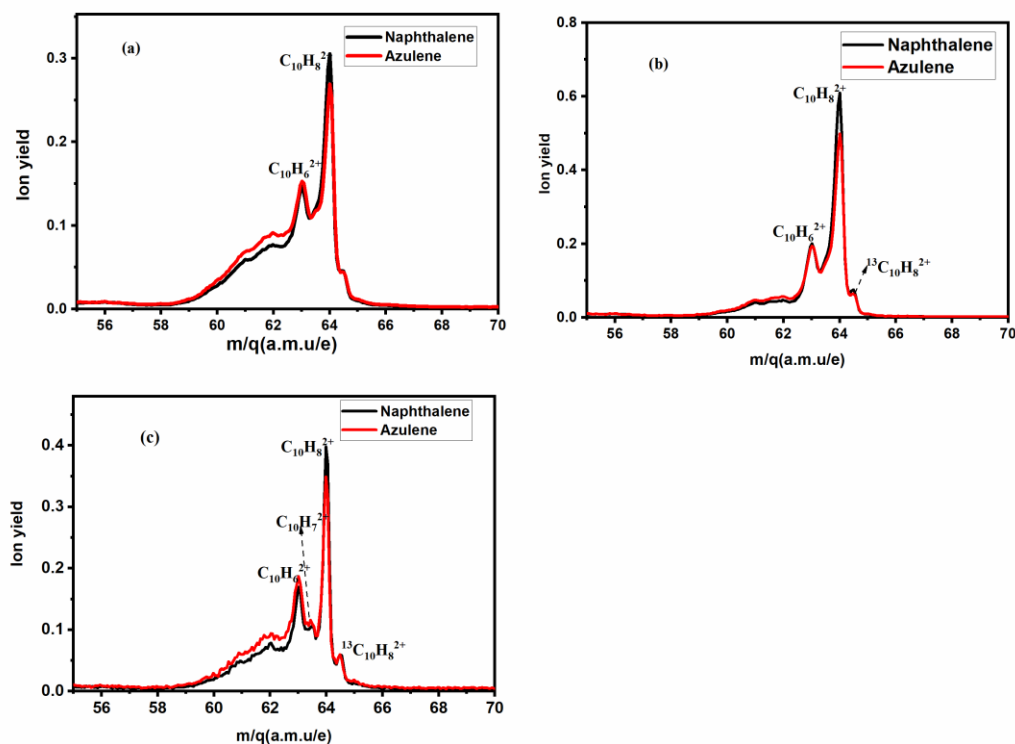


Figure 4-7: Mass spectra for naphthalene and azulene for the mass range 55-70 a.m.u, showing 2H/H2 loss is dominated over H loss in dications for (a) EE mode, (b) EE mode with finer position cut at the centre of position sensitive detector to avoid energetic fragmentation channels, (c) EC mode.

peaks. In this context internal energy available for intact photoion is approximately 13eV. Dyakov *et al.*[28] have calculated branching ratios of various decay pathways of $C_{10}H_8^+$ for a range of internal energies (5-13eV).They found that major H loss pathways peak at lower internal energies, whereas $2H/H_2$ loss peaks around 13eV. In view of these energetics, the present

observation of H loss suppression and $2H/H_2$ loss dominance implies that the internal energy available to $C_{10}H_8^{2+}$ is approximately 13eV. Now if we reconsider our previous deduction regarding the possibility of double plasmon resonance, then the energy difference between double plasmon excitation and double ionization matches strongly with the expected energy range where $2H/H_2$ loss peaks and H loss is suppressed. Thus, the two sets of observations viz. (i) dication having uniform yields for statistical dissociation channels irrespective of proton velocity, and (ii) complete suppression of H loss from the dication, and a strong agreement with double plasmon exciatation model, highly suggests that a fixed energy loss mechanism such as the double plasmon excitation is the likely origin of dication production.

## 4.9    Summary

It is hardly surprising that plasmon excitation play a major role in the single ionsiation of PAHs. Several studies in the past have demonstrated this aspect conclusively. What is of significance is the utilization of the energy post excitation by PAHs. Here again the coupling of plasmon excitation to inner valence electrons has been identified. Thus, a good amount of excess energy post ionisation is left in the molecular cation in the form of heat leading to statistical dissociation. We demonstrate an intriguing way the plasmon assist in isomerization of PAHs. This is of value due to the role of isomerization in the evolution of PAHs in the ISM and in flames. Further investigation unraveled the role of double plasmon excitation in the formation of hot dications. The scheme was quantified with the help of a plasmon excitation model and experimental evidences like suppression of atomic H emission from the dications. Considering the abundance of energetic protons in cosmic rays particularly in the shock waves of supernovae implies that such single and double plasmon excitation must have significant bearing on the final population of PAH species. In light of these new findings, it is essential to explore the phenomenon of plasmon excitation in PAHs in more details.

# CHAPTER 5. FORMATION OF CARBON CLUSTERS FROM MULTIPLY CHARGED PAHS

## 5.1    Introduction

The multi coincidence data collected in the proton-PAH experiment is rich in information regarding favored dissociation channels. Such details shed light on the intermediate structural transformation/ isomerization of multiply charged PAH cations. Apart from being useful in understanding the molecular dynamics, such details are valuable in understanding the role of PAHs in various radiation environment like the ISM. PAHs in the ISM are expected to undergo sequences of isomerisation and dissociation to produce complex molecules while interacting with energetic ions in the stellar wind or absorbing UV photons from stars. Often the isomerisation dynamics of neutral naphthalene/azulene is directly applied to monocations. But at higher charge states the molecular dynamics becomes more complex and interesting[65]. But such effects are very rarely studied in the past.

In this context a multi parameter- multi coincidence measurement of the fragmentation products is quite informative. Such analysis is often used in the case of multiply charged di or tri atomic molecules to understand their breakup mechanism and associated physics of the molecular dynamics. Due to the small size of the molecular ions, the momentum information of the fragment ions is very much discernible. In the case of larger molecules, such possibilities are less. Usually the kinetic energy release (KER) in the fragmentation process leaves its effect in the form of

elongated islands in the first hit versus second hit ToF spectra. Using these islands, it is possible to evaluate the KER release if the fragmentation is binary. The slope of the island gives the ratio of the charge states of the separating fragments. Apart from the identification of the dissociation patterns and the KER sometimes the island gives additional information in the case of statistical dissociation processes. An elongated tailing feature appearing in the 2D correlation spectrum connecting the fragment island to the parent ion mass is useful for measuring the dissociation time scale of metastable decay[66]. If there are more than two fragments involved, such multi hit analysis is also useful to identify if the dissociation process is sequential or concerted.

In this chapter we try to look deeper into the multihit data and identify important fragmentation channels. Interesting similarities are observed in the fragmentation cross sections. Most commonly studied channels are not dealt with in detail here, to avoid repetition. Very unique dissociation channels in single collision conditions are identified and demonstrated. We mainly focus on the emission of $H^+$, $C^+$ and $CH_3^+$ as the first hit fragment. The former two channels signify the violent multifragmentation while the later one is a statistical fragmentation channel which is often ignored due to its relatively low yield compared to $C_2H_2^+$ emission. But, in view of the recent proposition highlighting the role of methylenation as one of the PAH expansion mechanism in ISM and flame chemistry[67,68], we took a closer look for this channel, which led to an interesting insight into the process.

## 5.2    Computational details:

Statistical decay of PAHs tends to produce larger ionic fragments which can isomerize in to their own stable structural configuration. Moreover, multiply charged ions are produced with substantial amounts of internal energy to assist in crossing various transition state barriers of a dissociation process in ion-PAH collision (please refer sec 4.7 & 4.8 of chapter 4). As the intact ion of PAH eliminates a small neutral or ionic fragment like $CH_3^+$ or $C_2H_2^+$, smaller as well as larger fragments can be formed at larger vibrational energy. For PAHs in general and for naphthalene and azulene in particular, many of their large fragments themselves have been of interest separately. Hence, a great amount of literature on the spectroscopic studies of carbon clusters with $C_nH_m$ clusters (n < 10 and m <8) is available. We have used existing information on carbon clusters and carried out quantum structure calculations to identify the possible conformers

of $C_9$ and $C_7$ fragments formed in the proton interaction. Various structural conformers were computationally optimized using DFT. The B3LYP with 6-31G(d) basis, incorporated in the GAUSSIAN 09 package, was used for the calculations of $C_{10}H_8$ ions[12]. The basis set, cc-pVDZ was used to predict the total energy of $C_9H_5^+$ as well as $C_9H_5^{++}$ structures. The ground state energy was the only measure used to compare various conformations of a given ionic species.

## 5.3 Results and discussions

### 5.3.1 First hit analysis of low mass fragmentation channels:

The first hit yield of azulene and naphthalene are shown in figure 5.1. In spite of totally separate normalization, a very good match between the mass spectrum of the two targets is observed. In fact, some peaks can be seen to overlap exactly. The acetylene loss channel of azulene$^+$ ($m/q$=102) shows about 60% excess yield compared to naphthalene due to its fast isomerization. This is discussed in detail in chapter 4. On the other hand, approximately 12% excess yield in azulene is observed for all the rest of the fragments mainly originating from multiply charged cations. The excess yield of azulene at $C^+$ to $C_5^+$ peaks indicates that azulene
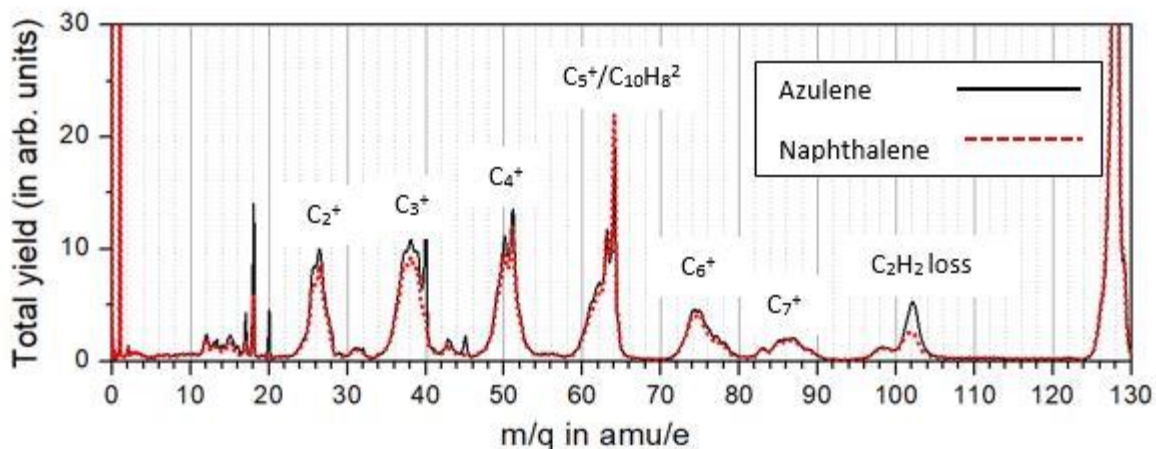


is relatively less.

Figure 5-1: The single hit mass spectra of naphthalene and azulene for 50 keV proton impact. Each mass spectrum is normalized with respect to the area of the singly charged parent ion peak.

stable under fast proton impacts. The isomerisation energy, even if it is available is not enough to influence such violent multifragmentation of multiply charged parent ions. The peak at $m/q=98$ has exactly the same cross section for the two isomers. The same conclusion can be drawn for the $C_7H_n^+$ fragment ions. The excess yield of naphthalene at $m/q=64$ is due to the stability of naphthalene$^{2+}$ compared to that of azulene$^{2+}$. The triply charged azulene and naphthalene ion is found at very little yield. The peak at $m/q=45$ in azulene spectrum is due to acetone impurity since it was used for cleaning the system before loading azulene. Similarly, the sharp peaks at $m/q=20$ and 40 are due to the Ar atoms in the background, which is used for calibration

### 5.3.2    Coincidence analysis for double hit data:

A 2D plot is made with first hit on the horizontal axis and second hit on the vertical axis for azulene as shown in the figure 5.2. The correlation patterns are found to be identical for the two of the isomer targets. The 2D correlation spectrum shows a rich structure with several islands, some with practically no momentum correlation features and some with even signatures of metastable decay in the extraction field of ToFMS. The featureless broad islands represent violent multifragmentation of multiple ionization channels, with more than two fragment ions being produced in a concerted manner. The islands with $H^+$ as the first hit are the most prominent channels.
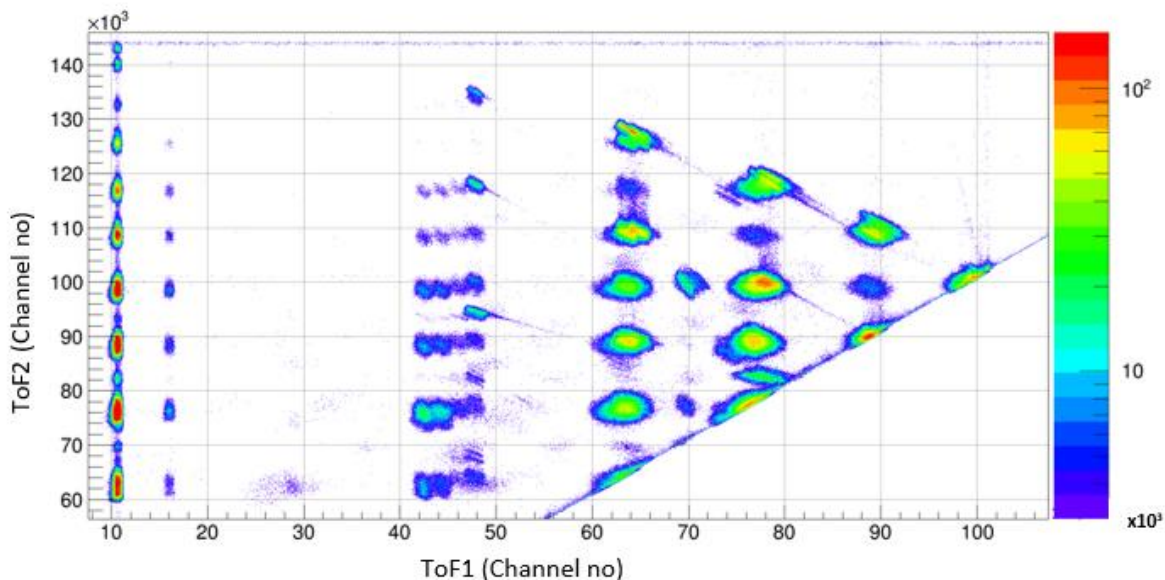
Figure 5-2: 1st hit versus 2nd hit 2D spectrum of azulene.

We have focused only on a few first hit channels namely the $H^+$, $C^+$ and $CH_3^+$ regions in the present study. Though the decay of highly charged parent ions of azulene and naphthalene is of great interest, we start with simple binary fission channels of parent dications,

$$C_{10}H_8{}^{x+} \quad \rightarrow \quad C_nH_m{}^{y+} + C_{(10-n)}H_{(8-m)}{}^{(x-y)+} \tag{5.1}$$
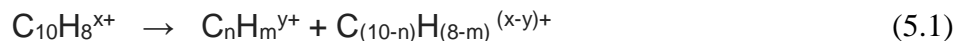
The most prominent amongst these are when n=8, 7 and 6 for the reaction (1), n=5 may also be present but it is difficult to separate from the effect of pulse pair resolution. There are a relatively low number of events with n=9. Fragments with n=8 and n=7 are observed to be metastable within the present extraction timescale whereas n=6 is a fast decaying process. A clear correlation is observed between the carbon numbers of the two fragments for all the binary channels. As one goes from n=9 to 6 the decay process shifts from hydrogen conserving channels to more dehydrogenation channels (See figure 5.3.).
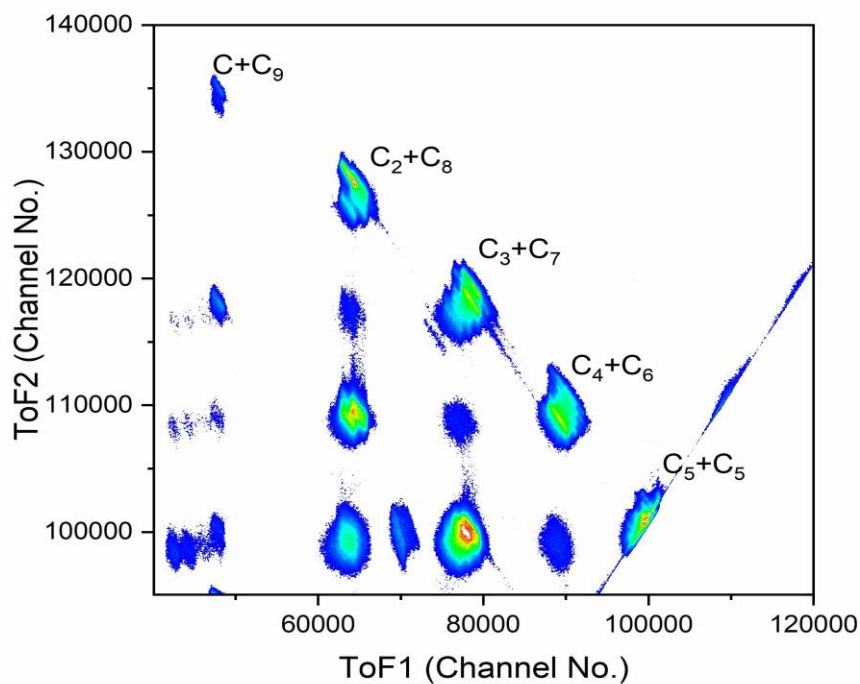
Figure 5-3: 1st hit versus 2nd hit 2D spectrum of azulene showing carbon conserving binary fission channels.

### 5.3.3 KER spectra for binary dissociation channels of $C_{10}H_8^{2+}$ isomers

The diversity of the 2D fragmentation pattern suggests that the potential energy surface is rather complex. Here, we have focused on a few simple two-body break-up channels of doubly charged transient naphthalene and azulene ions. The time and position data obtained during the proton impact experiment were analyzed on an event-by-event basis to determine the KER spectra of a few binary fragmentation channels. The KER spectra of a few fragmentation channels are displayed in figure 5.4.
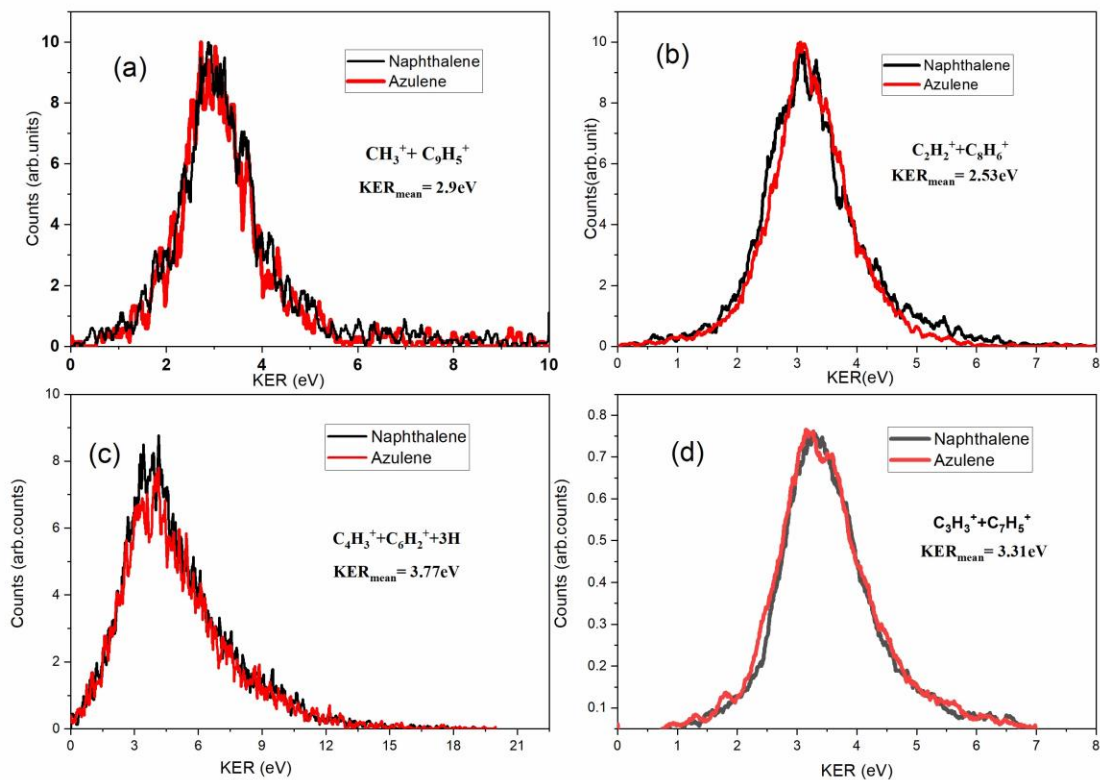
Figure 5-4: KER spectra of (a) $CH_3^+ + C_9H_5^+$ (b) $C_2H_2^+ + C_8H_6^+$ (c) $C_4H_3^+ + C_6H_2^+ + 3H$ (d) $C_3H_3^+ + C_7H_5^+$ fragmentation channels.

There are two type of fragmentation processes. In a type 1 process, the potential energy is increasing continuously along the reaction coordinate until the dissociation limit is reached as shown in figure 5.5. This type of reaction requires very little rearrangement in the transition state and is characterized by a negligibly small reverse activation energy. A parent ion with excess internal energy, fragmenting in type 1 surface, will partition the energy to all the degrees of freedom. The probability of distributing a given energy into kinetic energy of a fragment is determined by the density of states of the fragments. Since the density of vibrational states rises dramatically with increasing ion internal energy, the probability of distributing energy into kinetic energy of fragments will decrease rapidly with increasing kinetic energy release. Therefore, the KER spectrum of type 1 will be centered close to zero and has an exponential tail towards higher energies.

A type 2 fragmentation process is characterized by a substantial atomic rearrangement, a tight transition state and a high reverse barrier. Therefore, the KER distribution is shifted to a

nonzero value, which is equal to the reverse barrier height. It is noteworthy that the position and shape of the KER distribution is determined not only by the shape of the potential energy surface but also by the dynamic effects that occur as the products separate. All KER spectra listed here for dication fragmentation channels are centred around 2-4 eV. These fragmentation channels results in to charged fragments. It can be the Coulomb repulsion between the charged fragments that gives rise to very large KERs in these reactions. It is substantiated by the fact that KER values increase as one goes from $C_9H_3^+ + CH_3^+$ channel to $C_7H_5^+ + C_3H_3^+$ channel, because of the possible reduction of the intercharge separation in transient ions for the later channels.
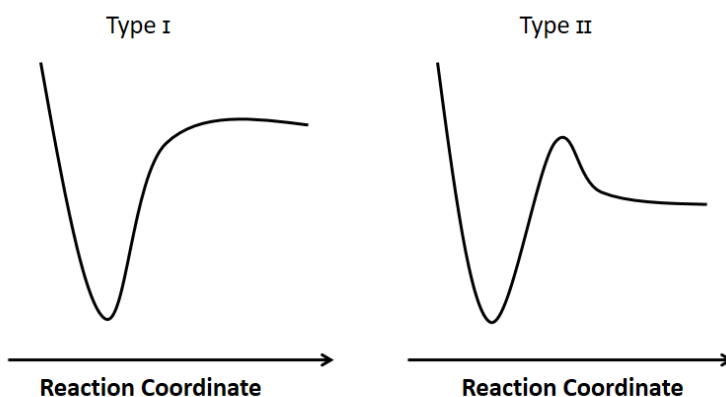


Figure 5-5: Schematic drawings of two potential energy profiles. Type I and Type II potential energy surfaces, as explained by Laskin and Lifshitz[69].

KER distributions of binary fragmentation channels are very similar for naphthalene and azulene. It mainly shows that the potential energy profile of the precursor ion is common to both isomers. It encourages to propose a fast isomerization of doubly charged azulene and naphthalene to a common intermediate isomer before fragmentation. Leach *et al*[70] have proposed an isomerization pathway for azulene$^{2+}$ and naphthalene$^{2+}$ to a common intermediate isomer prior to fragmentation as shown below.
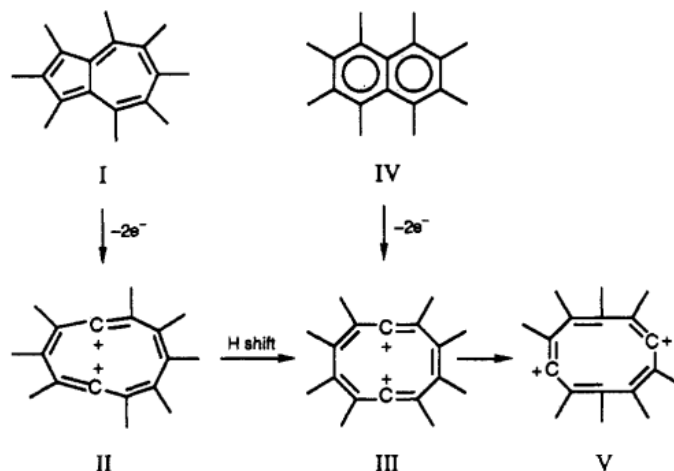
This involves rupture of the transannular bond in azulene (I) by loss of two electrons to form structure II, followed by 1,2-hydrogen shifts to structure III which is directly accessible from naphthalene (IV) by breaking its transannular bond. Maximum separation of the two positive charges would follow by further H shifts to a structure such as V. It can also be proposed that further rearrangements like H migrations, bond breaking, and eventual recyclization will be common for two of the isomers to achieve configurations leading to the observed dissociation products with the same KER.

### 5.3.4    Binary dissociation of $C_9H_7N^{2+}$ isomers

We have unraveled the certain fragmentation channels of the nitrogen containing aromatic isomers quinoline and isoquinoline in collision with an intermediate velocity proton beam. The 2D ToF correlation spectra are similar for the two isomers. Contrary to the expectation based on past single ionisation experiments and prevailing understanding, we observed for the first time that loss of $HCNH^+$ is by far the most preferred fragmentation channel of dications of quinoline and isoquinoline (see figure 5.6). $HCNH^+$ is observed to be an important ion in the ionosphere of Titan and was recently detected in the ISM. This encourages further investigation of $HCNH^+$ loss channels of PANHs in collision with fast heavy ion.
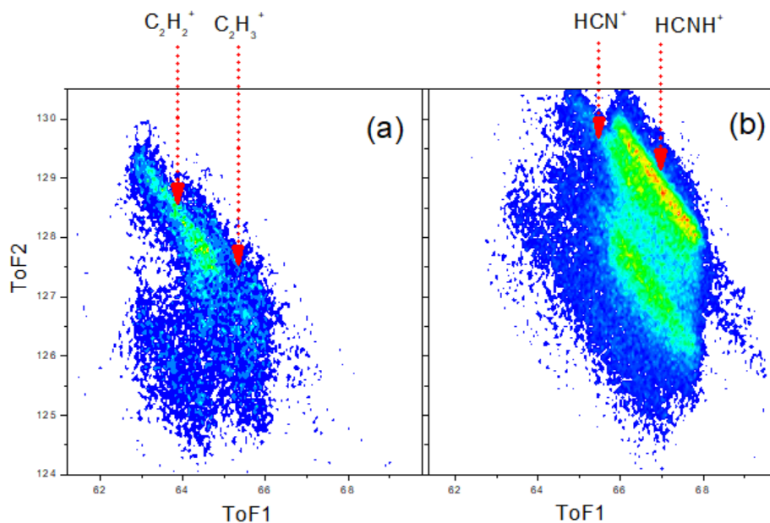
Figure 5-6: Binary decay channels of (a) naphthalene and (b) iso-quinoline dications in collision with 50 to 150 keV proton beam. Iso-quinoline shows very strong HCNH$^+$ emission compared to other channels.

KER spectra of HCNH$^+$ loss and HCN$^+$ loss channels of quinoline$^{2+}$ and isoquinoline$^{2+}$ is shown in figure 5.7. It is compared with the C$_2$H$_2^+$ loss channel of naphthalene and azulene dications. The HCNH$^+$ loss channel and the C$_2$H$_2^+$ loss channel have similar KER distributions. But the KER spectrum of the HCN$^+$ emission channel is shifted to lower values. It implies that HCN$^+$ is formed from an extended intermediate structure which can have larger charge separation. Therefore, the reverse barrier due to Coulomb repulsion can be reduced. The barrier energy to produce such an extended isomer from compact structures like quinoline or isoquinoline will generally be high. It results in lower intensity for the HCN$^+$ emission channel. But HCNH$^+$ is likely to be formed from compact structure so as to have higher Coulomb barrier. It is instructive to investigate the energetics of HCNH$^+$ and HCN$^+$ emission channels of doubly charged C$_9$H$_7$N in a photodissociation experiment.
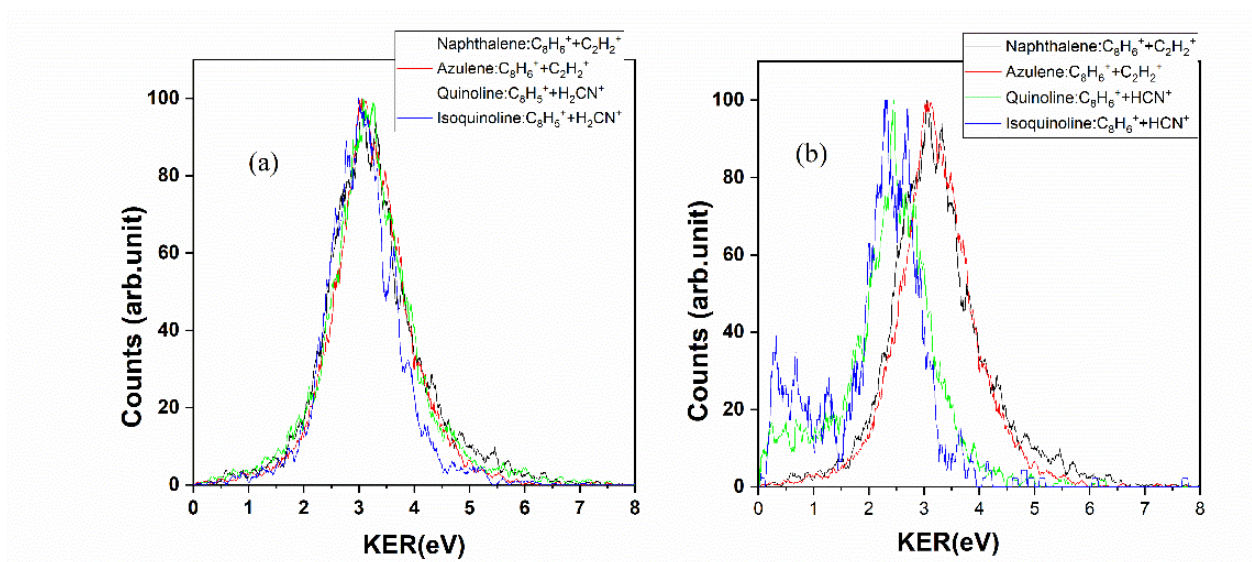
Figure 5-7: KER spectra of important fragmentation channels of azulene$^{2+}$, naphthalene$^{2+}$, quinoline$^{2+}$ and isoquinoline$^{2+}$.

### 5.3.5    H$^+$, C$^+$, CH$^+$ and CH$_3^+$ emission channels of multiply charged PAH isomers

### 5.3.5.1    H$^+$ coincidence
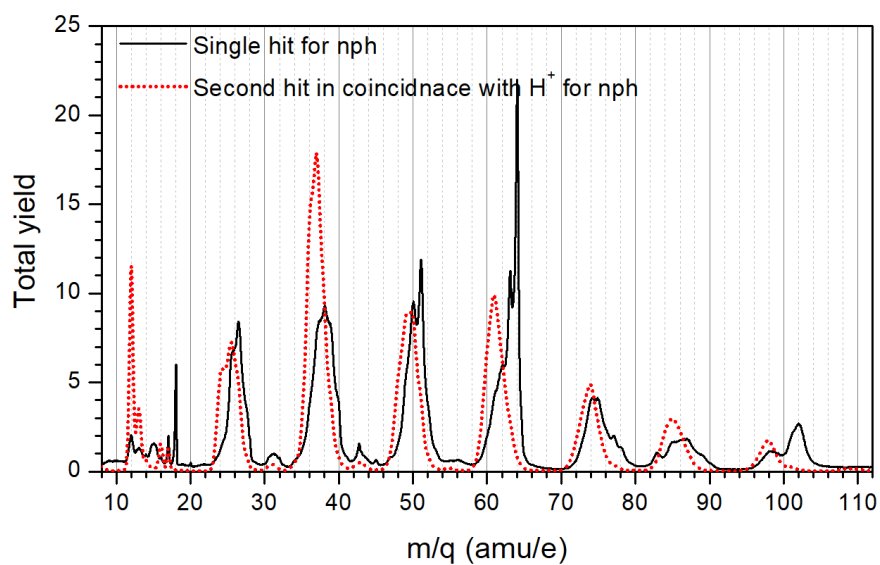


Figure 5-8: Comparison of single hit mass spectrum of naphthalene with second hit spectrum of H$^+$ channel for the same target.

The elimination of $H^+$ from the molecule is always observed with substantial amount of multi fragmentation. Considering the relatively high detection efficiency of the $H^+$ ejected from the target, we observe a very strong correlation with all other smaller mass fragments. Figure 5.8 shows the comparison of pure single hit mass spectrum with second hit mass spectrum obtained in coincidence with $H^+$ in first hit. Two major observations can be made immediately, none of the sharp peaks are present in the second hit mass spectrum of $H^+$ channel and the yields of low carbon containing fragments is substantially more than the corresponding yield in the single hit spectra. Particularly so for $C^+$ and $C_3^+$ and $C_5^+$. The former effect is due to the fact that the ion detected here is a result of fragmentation of multiply charged cation with $H^+$ as one of the fragments and hence, will correspond to some spread in the initial energy leading to broader peaks. The single hit spectra will contain mainly singly charged partner events like mono or dication of parent and their neutral evaporation fragments appearing as sharp feature due to very small KER. In addition, those multifragmentation events where only one of the product ions was detected due to less than unity detection probability will also appear in the single hit spectra. From later observation, it is clear that emission of $H^+$ in a multi fragmentation event favors the formation of odd carbon number low mass fragment with much more probability than the heavy carbon clusters. Such a behaviour is typical to carbon clusters due to their oscillating binding energies[71]. This combined with the fact that there is no clear momentum correlation observed in the $H^+$ and $C_n^+$ mass fragments indicate that $H^+$ is predominantly produced from very highly charged parent ions with charge state greater than three, undergoing a violent concerted multi fragmentation.

A comparison of the second hit mass spectrum recorded along with $H^+$ ions for both naphthalene and azulene is presented in figure 5.9. As far as n=6, 7 and 8 are concerned, there is no difference between azulene and naphthalene. All other $C_n^+$ channels of azulene shows more yield by about 12 % than naphthalene. We attribute this to come from the inherent high energy structure of azulene in comparison to naphthalene. Another very interesting observation is the presence of super dehydrogenated azulene or naphthalene monocations as shown in figure 5.10. For the first time, we report here the possibility of losing all the 8 hydrogen atoms from azulene/naphthalene in a single interaction. The system prefers to lose 2, 6, 7 or 8 hydrogens with at least one of them emitted as proton. Such super-dehydrogenation and the fact that 3,4 and 5 H loss is not favored requires detailed investigation of molecular dynamics and will be of great

significance to astronomical understanding of atomic and molecular Hydrogen population in the ISM.
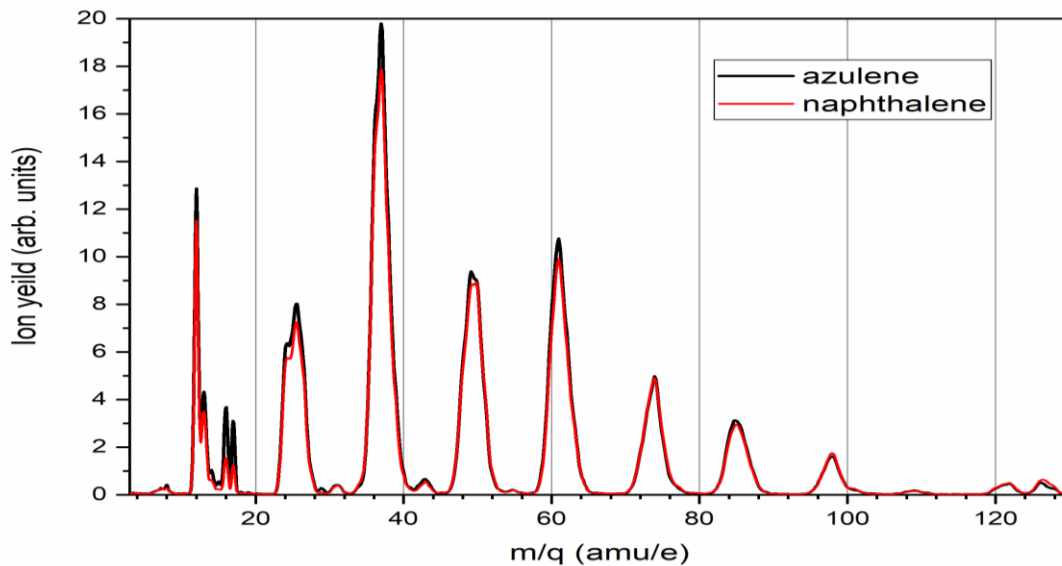


Figure 5-9: second hit mass spectra of azulene and naphthalene in $H^+$ coincidence.
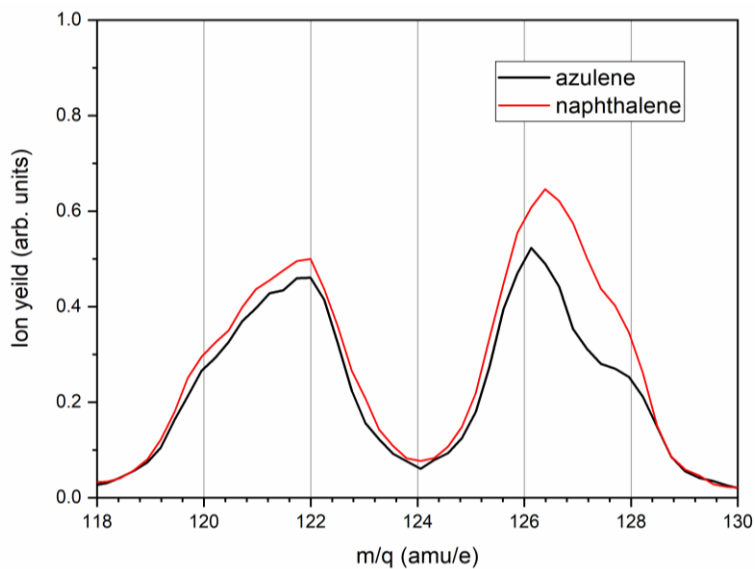


Figure 5-10: Signature of super-dehydrogenation of azulene and naphthalene. Total dehydrogenation can also be noted.

### 5.3.5.2    $C^+$, $CH^+$, $CH_2^+$ coincidence:

Apart from the absence of a $C_8^+$ ion peak, the second hit mass spectrum of $H^+$ and $C^+$ coincidences are identical (see figure 5.11). The $C^+$, $CH^+$ and $CH_2^+$ emissions show similar second hit mass spectra. The $C^+$ loss channel is clearly a multifragmentation channel because n=8 or 9 are practically absent in the second hit mass spectrum of $C^+$/ $CH^+$/ $CH_2^+$ channels. As in the case of $H^+$ channel, the $C_3^+$ fragment region is the most dominant one for the $C^+$ channel. The $C^+$ (and $CH^+$ and $CH_2^+$) coincidences are essentially the same multifragmentation events as for $H^+$ emission but in these events $H^+$ is not detected and hence the $C^+$ fragment is observed as first hit event instead.
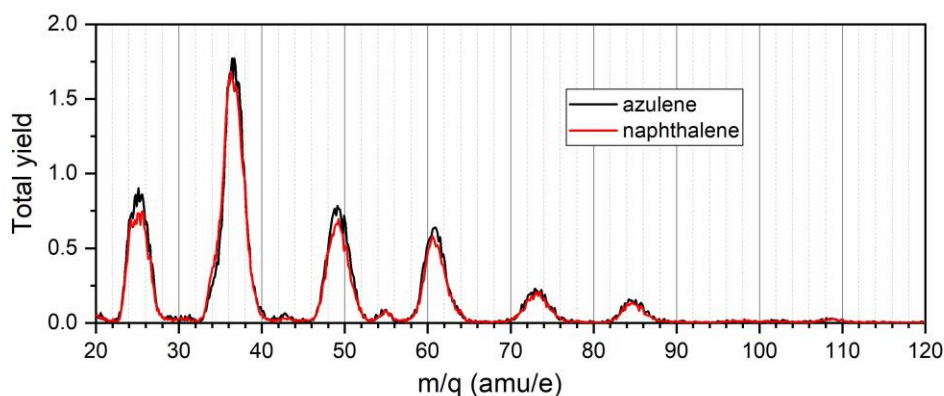


Figure 5-11: second hit mass spectra of azulene and naphthalene for $C^+$ coincidence.

The second and third hit coincidence spectra with $H^+$, $C^+$, $CH^+$ and $CH_2^+$ as first hit, are typical violent multi fragmentation channels of multiply charged intact parent ions. Such fragmentations are insensitive to the original structure and the propensity of a certain carbon cluster is decided by its binding energy and the ionization potential[71].

On the other hand, any channel which progresses through formation of a metastable intermediate is of interest in terms of the molecular dynamics. Prominent statistical neutral loss channels from mono and dications of PAHs in general and from naphthalene and azulene in particular have been centre of several investigations. The formation of $H_2$ and $C_2H_2$ from PAHs is of significance in several astronomical models. Especially, to reproduce the observed diffuse and unidentified interstellar bands emissions in the ISM. Moreover, the ring opening mechanisms in smaller PAHs are considered key to understanding the formation of larger PAHs as well as

heterocyclic aromatic organic molecules and ultimately the formation of biomolecules in the ISM. To this end the hydrogen abstraction acetylene addition (HACA) process has been in discussion for quite some time and considered as an important mechanism leading to growth of PAHs. But recent experimental results have demonstrated that such an abstraction is inefficient and slow in interstellar conditions, Hence, it fails to account for the formation timescale of PAHs predicted in astronomical models[67]. Along the same line, very recently, a new ring expansion and PAH growth process is found to be more plausible in the ISM[68]. This process involves the addition of a methyl group to a five membered ring of a PAH for converting it to a six membered ring PAH. Hence, we look at the second hit mass spectrum of $CH_3^+$ emission and compare it with $C^+$ coincidence.

### 5.3.5.3    $CH_3^+$ Coincidence:

A plot of second hit mass spectra in coincidence with the $CH_3^+$ channel is shown in figure 5.12. There is a clear difference between the second hit mass spectra of the $C^+$ and $CH_3^+$ channels. $C_7H_3^+$, $C_9H_5^+$ and $C_9H_5^{2+}$ are seen to be major second hit fragments of $CH_3^+$ loss. Though the mass spectra lack the required resolution to identify the exact number of H atoms contained in a given $C_7$ or $C_9$ fragment, the 2D diagram was helpful in finding the exact number of H atoms in these fragments. The mass spectrum below $m/q$=46 is heavily affected by acetone contamination. This was confirmed due to a correlated binary fragmentation pattern of acetone present in the 2D diagram. The difference between the second hit mass spectrum of azulene and naphthalene is plotted in figure 5.12. The differential yields of the $C_2^+$, $C_3^+$, $C_4^+$, $C_5^+$, $C_6^+$ and $C_8^+$ fragments are negligible for $CH_3^+$emission. It is discernible that $CH_3^+$ loss is primarily a statistical process, because major $CH_3^+$ loss channels were showing signatures of metastable decays. We also observe that the $CH_3^+$ loss channel is almost exclusive to loss of $H^+$. This can be seen in figure 5.13, wherein $C^+$, $CH^+$ and $CH_2^+$ are clearly visible but a few counts at $m/q$=15 is purely due to chance coincidence with $H^+$.
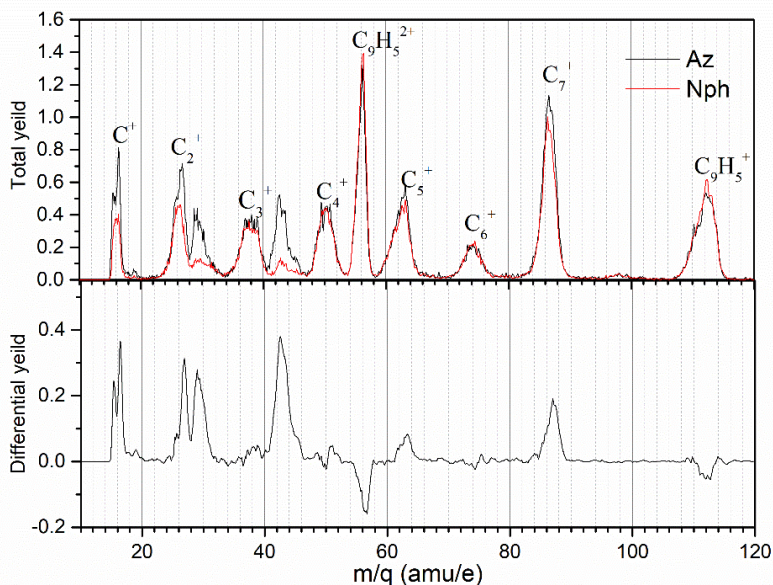
Figure 5-12: second hit mass spectra of azulene and naphthalene in coincidence with $CH_3^+$ is shown in the top and the differential fragment yield between the two targets for the same channel is shown in bottom.
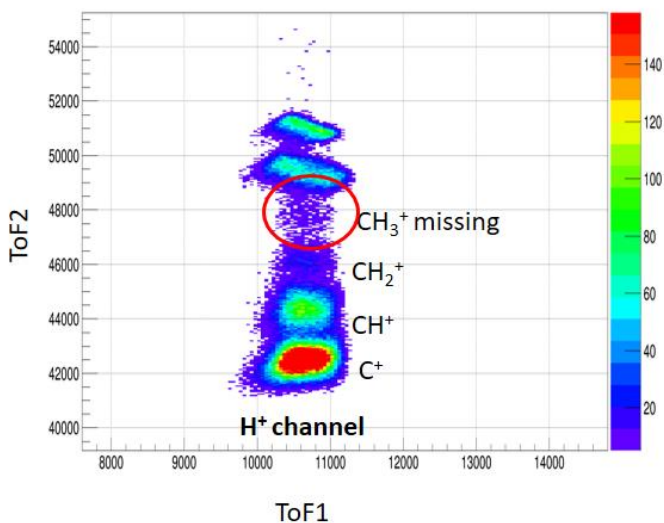


Figure 5-13: $H^+$ coincidence with $m/q = 12$ to 17 regions. It is noteworthy that $m/q =15$ region is filled with only chance coincidence.

The elimination of $CH_3^+$ from multiply charged naphthalene or azulene is indeed very intriguing, considering the parent ion structure. In this respect, a possible parent dication conformer was proposed by Kingston et al.[72]. as the originator of the $CH_3^+$ fragment. The corresponding structure is shown in table 5.1 (structure A). This was further investigated by

Leach *et al.*[70] to explain the $CH_3^+$ elimination from the naphthalene dication on the basis of the kinetic energy release measurements[59]. The experimental KER release reported by them was approximately 1 eV whereas the structure A would correspond to about 2 eV KER. Therefore, Leach *et al.* considered a linear geometry as a more probable intermediate structure over structure A. Our KER measurement for both naphthalene and azulene target for $CH_3^+$ - $C_9H_5^+$ channel was found to be 2.9 eV. This number matches very well with the value measured by Reitsma *et al.* more recently[73]. It suggests that the isomer independent conformer from which $CH_3^+$ elimination can occur, is possibly structure A as originally suggested by Kingston *et al.* But, when we

Table 5.1: Energy values ($\Delta E$) of $C_{10}H_8$ isomers in doubly and triply charge state w. r. t. the lowest-energy structure of naphthalene. Calculations are done in DFT method at 631G (d) basis.

| | $\Delta E$ for dication (eV) | $\Delta E$ for trication (eV) |
|---|---|---|
| Naphthalene | 0 | 0 |
| Azulene | 0.408 | 0.2992 |
| A | 3.0736 | 2.2032 |
| B | 1.9584 | 1.1424 |
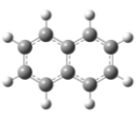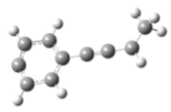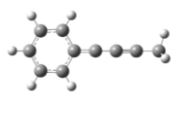
performed DFT calculations for other possible isomeric structures, it is observed that the dication structure A was about 3 eV higher in energy with respect to naphthalene$^{2+}$ while the structure B

shown in table 5.1 is found to be more favorable with a total energy of 2.0 eV more than naphthalene$^{2+}$. Hence, we propose that the elimination of $CH_3^+$ ion occurs via a common intermediate dication conformer B. The same structure is proposed as the possible intermediate trication species due to its low binding energy.

The radical difference between the $C^+$ and $CH_3^+$ coincidence data prompted us to investigate further dissociation of the residual fragment ion. The coincidence data between 2nd and 3rd hit of $C^+$ and $CH_3^+$ channels are shown in figure 5.14. The $C^+$ coincidence shows no specific correlations between 2nd and 3rd hit fragments.  But, in the case of the $CH_3^+$ channel, a clear momentum correlation can be seen in the dissociation pattern of the $C_9H_5^{2+}$ channels. The other dissociation channels as well as concerted decays were not seen for $CH_3^+$ emission. Three binary fission channels of $C_9H_5^{2+}$ with metastable decay features are observed in similar intensities in the 2nd to 3rd hit correlation diagram of $CH_3^+$ channel. These binary channels can be summarized as follow.

$$(5.2)$$
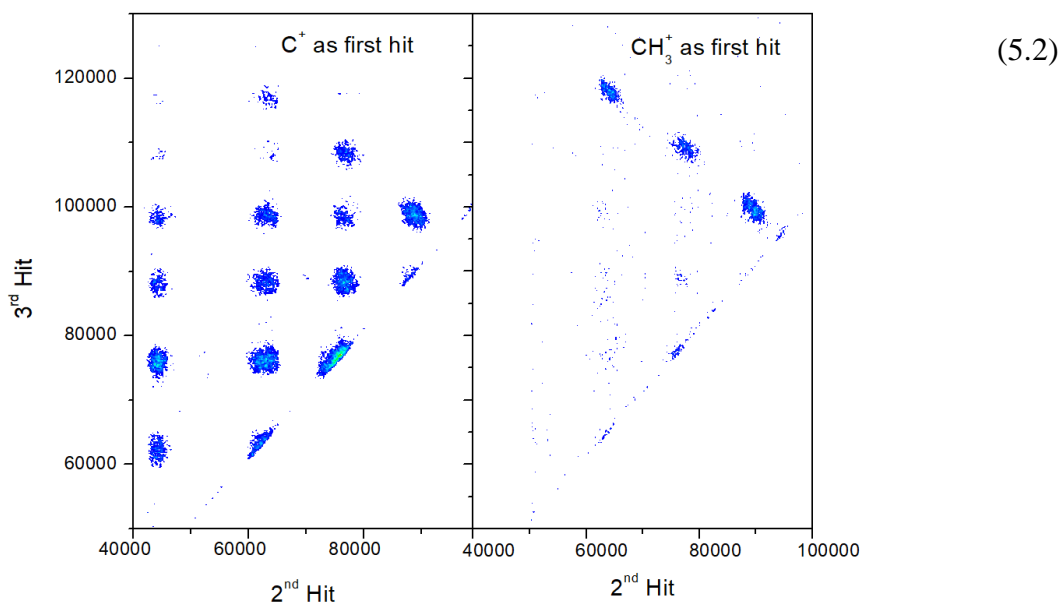


Figure 5-14: 2nd versus 3rd hit plots for $C^+$ coincidence (left) and $CH_3^+$ coincidence (right).

Structural conformation of partially hydrogenated $C_7$ and $C_9$ neutrals as well as ions are being investigated as possible carriers of diffuse infrared bands (DIB) in ISM[74]. Their formation and participation in expansion of PAHs by fusion reactions are of recent interests. For example,

Steglich *et al.*[74] have observed emission band of the $C_9H_5$ neutral radical and used quantum structure calculations to identify the most probable conformers of the same. Moreover, they were successful in obtaining a good match between the observed emission bands with the emissions recorded from two astronomical sources. In addition, several investigations have been conducted recently to understand the exact structure of these species. There are seven possible structures which are proposed for the $C_9H_5$ radical (neutral)[74]. We consider the same set of structures for mono and di cations. The $3^{rd}$ hit mass spectra in coincidence with $CH_3^+$ as first hit was very useful to identify the most probable structure. The relative ground state energy of seven $C_9H_5^+$ and $C_9H_5^{2+}$ fragments is calculated using DFT as implemented in Gaussian09 and is also listed in table 5.2. As per these calculations, the most stable isomer of $C_9H_5^{2+}$ will be structure A. It is supported by the third hit spectrum recorded in coincidence with $CH_3^+$. The conformers A and G can produce $C_2$-$C_7$, $C_3$-$C_6$ and $C_4$-$C_5$ fragments in almost identical intensities as observed in the third hit mass spectrum of $CH_3^+$ emission. But energetically, the most adequate isomers of $C_9H_5^{2+}$ will be structure A. Similarly, we have optimized these seven structures to identify stable isomer of $C_9H_5^+$. As per this calculation energetically stable isomer of $C_9H_5^+$ will be structure D.

Table 5.2: Energy values ($\Delta E$) of $C_9H_5^+$ and $C_9H_5^{2+}$ isomers w. r. t. lowest energy structure. Calculations are done in DFT method at 631G (d) basis.

| Structure | $\Delta E$ for monocation | $\Delta E$ for dication |
|---|---|---|
| A | 0.90003 | 0 |
| B | 1.11034 | 0.45396 |
| C | 1.3286 | 0.52081 |
| D | 0 | 0.49014 |
| E | 0.26752 | 0.01836 |
| F | 0.21943 | 1.16927 |
| G | 1.53503 | 0.19864 |
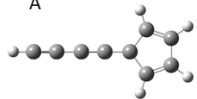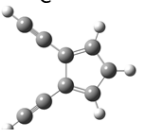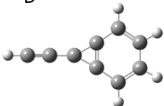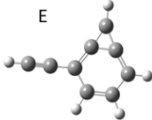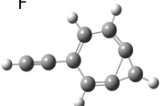
## 5.4    Summary

Swift charged particle induced single and double ionisation of naphthalene as well as azulene is found to be plasmon dominated. Such ionisation processes deposits high amounts of excess energy in the resultant cations, which can then be used to have considerable probability of high energy isomer formation. One such mechanism of $CH_3^+$ elimination is found to progress via a common isomer of naphthalene and azulene. The methyl ion elimination process, is observed to produce astronomically important clusters like $C_9H_5^+$, $C_9H_5^{++}$ and $C_7H_3^+$ by cascade of statistical dissociations. A new parent dication as well as trication isomer of naphthalene and azulene is proposed here with the help of DFT calculations which can eliminate $CH_3^+$. The $C_9H_5^+$ formed in dication decay of both the molecules was found to further eliminate $C_2H_2$ to form $C_7H_3^+$ whereas $C_9H_5^{2+}$ is found to undergo a binary fragmentation process with clear momentum correlation. The presence of $C_4^+$ fragment indicated possible $C_9H_5^{2+}$ structure with a long carbon chain. Various DFT optimized structural conformers were compared and the lowest energy dication structure of $C_9H_5^{2+}$ was indeed found to have a pentagon and long linear chain structure. This observation compares favorably with the experimental 3rd hit spectra in coincidence with $CH_3^+$ as first hit.

In addition to the decay cascade of $CH_3^+$ loss channel, a few other observations are also important to note. Firstly, we report observation of super-dehydrogenation of naphthalene as well as azulene molecules in a single collision with evidences of all the way up to complete dehydrogenation. Secondly, the $H^+$ elimination process was found to be totally exclusive of the $CH_3^+$ loss channel.

# CHAPTER 6. INTERNAL ENERGY CONTROLLED IONISATION OF AZULENE, NAPHTHALENE AND FLUORENE

## 6.1    Introduction

Any systematic measurement of statistical molecular dissociation demands a good control over the molecular internal energy. One of the possible methods to perform such measurements is to produce cations of PAHs by conventional techniques and then heat them by photo excitation using a tunable laser[31,75]. Experimentally, the ionization process itself brings out complications like determination of residual internal energy after ionization or cooling the molecular ion to a very low temperature in ion traps, formation of multiple conformers of the parent ion etc. In some rare cases explicit measurement of the internal energy distribution is carried out and this information is then used in modelling the decay curve[75–77]. Techniques like PEPICO, iPEPICO, tPEPICO etc. are often used in conjunction with the synchrotron radiation sources to identify dependence of internal energy ($E_{int}$) on a particular decay channel[25,78]. Since most PAHs have their ionization energy in the range of 7-8 eV and the appearance energy of low energy fragmentation channels is typically around 15 eV[57], these experiments are usually done with VUV photons. But such measurements require complex instrumentation, large facilities and are often very time consuming because of low operating count rate to avoid false coincidences. In VUV mass spectrometry, the internal energy distribution IED is too broad to account for, without tracking the energy of the photo electron. The charged particle excitation process is too broad to quantify the same way as photon excitation, though some attempts are made to track the energy

of the outgoing projectile as well as emitted electron, but again, the requirement of triple coincidence makes the measurements very difficult[79,80].

All the methods of highly excited cation production described above finally use an ion storage ring or ToF technique. In the former case, the identity of the decay channel is ambiguous and in the later technique the available time window for detectable decay is usually limited to the first few microseconds. A ToF mass spectrometer combined with an ion-trap can target a longer time scales compared to standard linear ToF arrangement, but observations at shorter time scales are disturbed by extraction time uncertainties[27]. For PAHs, the decay rate of H loss or $C_2H_2$ loss channels vary by several orders of magnitude for few eVs of shift in internal energy[27,28]. Thus, a spectrometer covering a continuous range of time scales from hundreds of nanoseconds (ns) to few millisecond will be most suitable to study isomerization effects upon dissociation channels.

As discussed in section 2.5 and section 3.2, wherein a very special experimental arrangement is prepared and validated to produce a narrow internal energy ensemble of fluorene cations. The surprising simplicity of the observed internal energy control in fluorene warranted a proper explanation and possible extension to other PAHs. The same methodology is further applied to two of the isomers, naphthalene and azulene to look for possible similarity in the excitation and internal heating mechanism. In this context, azulene was considered as one of the best targets, since its excited state dynamics has been investigated very thoroughly in the past[81–87]. It possesses very peculiar excited state dynamics which has been of interest for the last few decades[81]. It is a well-known example for non-conformation to Kasha's rule[81] because an excitation of azulene to any of it's high $S_n$ state settles in to the $S_2$ state due to rapid IC unlike the condition stated by Kasha's rule of relaxation to the $S_1$ state. The ionization potential of azulene is fairly low, about 7.44 eV, so that a photon tuned to excite $S_n$ (where n>1), will be able to ionize the molecule from any electronic state higher than and including $S_2$. Combined with the ultrafast IC of azulene from $S_n$ to $S_2$ and the electronic rigidity of PAHs, a possibility of producing PAH ions at higher and well-defined internal energies is opened. In this chapter, we demonstrate that if excited state dynamics of a molecule is known in detail, a single color nanosecond tunable laser may be sufficient to measure the dependence of internal energy on its dissociation channels.

## 6.2    Experimental measurements and analysis

The experiment was performed with an azulene target in an identical manner as discussed in section 2.5.2, but at several wavelengths in the UV region. One typical ToF spectrum measured using high resolution energy-ToF spectrometer at 235nm and $10^9$ W/cm$^2$ is shown in figure 6.1. $C_2H_2$ loss has a distorted ToF distributions as shown in figure 6.1. This arises from the fact that fragment ions after $C_2H_2$ loss, are produced within the extraction or acceleration region of the ToF spectrometer. The decay rate of the $C_2H_2$ loss channel can be estimated by simulating the observed ToF distribution in exponential decay in the extraction or acceleration field. The peak width of the H loss fragment ion produced in ER and AR is within the time resolution (10ns) of the spectrometer. Therefore, the H loss peak has a normal narrow distribution. The information about the H loss channel of azulene is only used in the present chapter, since the main focus here is to understand the role of excited state dynamics in determining the internal energy of the cation produced. In this context it is most suitable to consider loss of an atomic fragment rather than a molecular fragment which might bring up its own complexity. The fraction of parent and fragment yields with respect to total number of laser pulses (mass spectrum recorded for azulene at 235nm and $10^9$ W/cm$^2$ has 1.2% of fragment ions and 5.6% of parent ion) show that the lower laser intensity restrains the absorption to two to three photons.

In the present experimental set up, the intact azulene$^+$ spends about 400 ns in the extraction region and 200 ns in the acceleration region. The field free drift region is extended to about 780 mm length, corresponding to a drift time of about 13 μs. A daughter ion produced in the ER or AR will have kinetic energy (KE) between maximum possible KE (KE of fragment ion produced in the first few nanoseconds after laser pulse) and the fraction of KE proportional to its mass. A fragment ion produced in FD region will have the lowest KE among all the H loss product ions and the KE carried by such fragment ions will be proportional to its mass. Thus, the data obtained with time as well as KE spread would enable us the prediction of the decay time scale. One example of a ToF versus KE correlation plot is shown in figure 6.2. Population of H loss fragments is distributed as per their respective decay location. Qualitatively we can identify three possibilities for an internally hot parent ion which is about to lose H. If the H loss occurs in ER or AR region the resulting $m/q$=127 will be located at the full ToF of $m/q$=127 (channel no:

458400) and about full KE imparted by the extraction and acceleration voltages with channel no: 460 along the y-axis as
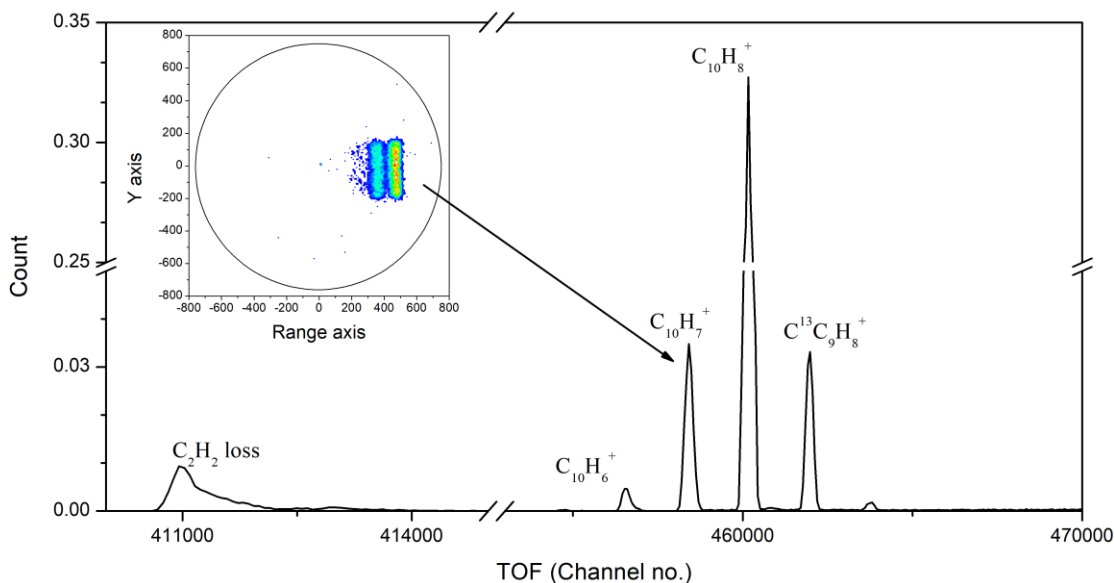


Figure 6-1: ToF spectrum of azulene recorded at 235nm and $10^9$ W/cm$^2$. The inset figure corresponds to the distribution of the H loss channel on the ion PSD. It separates low and high energy H loss peaks along the horizontal coordinate with a typical resolution of 7eV over 3keV.

shown in figure 6.2. This we call as "fast H loss" or "fast peak". If the decay occurs in the FD region, the decay population is concentrated about the same ToF as $m/q=127$ (channel no: 458502) but at $\approx0.8\%$ less KE compared to the fast peak (channel no: 350). This island is labelled as "slow H loss" or "slow peak" in the 2D graph. If the decay occurs in the PPA region, we will observe a belt connecting full energy parent peak to the slow H loss peak. There is some micro structure to the fast peak and the region connecting fast to slow peaks due to the decay dynamics in the ER and AR, but considering the small change in KE for single H loss, it is hard to quantitatively analyze this gap between fast and slow peak.

The rate constant of H loss decay is extracted from the 2D correlation diagram with the help of a *Monte Carlo* simulation. The details of this simulation and method of rate constant deduction from the experimental 2D data is given in sec 3.2 of chapter 3. A brief description is

added here. The dissociation rate constant is the only adjustable parameter in the simulation which fits the relative population on different peaks appearing in the 2D plot. If the fast H loss peak is only present in the 2D diagram, rate constants must be $k \geq 10^7 \, s^{-1}$. If H loss population is dominated on
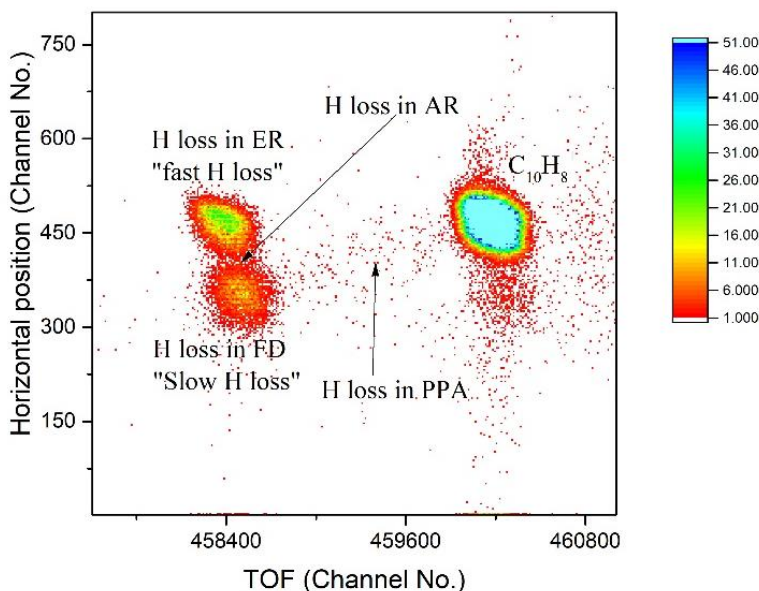


Figure 6-2: 2D diagram for ToF versus horizontal position (horizontal position linearly scale to the kinetic energy of the ion) of parent and H loss fragment ion measured at 235nm and $10^9 \, W/cm^2$. Various features in the 2D diagram are marked according to their corresponding decay locations

the fast and slow peaks, the corresponding decay rates will be between $10^7 s^{-1}$ and $5 \times 10^5 s^{-1}$. The belt corresponding to the decay inside PPA will be populated for decay rates between $5 \times 10^5 s^{-1}$ and $10^3 s^{-1}$ [See figure 3.11 in chapter 3]. In our experiment the H loss distribution is characterized by both fast and slow H loss peaks with negligible population in the belt for the wavelength range 235nm to 256nm. The ratio of slow to fast H loss yield measured in the experiment is reproduced in the simulation by assigning an appropriate decay rate. The ratio between slow and fast H loss yields obtained for each wavelength is discussed in the next section in the context of 3 or 4 photon absorption.

## 6.3    H loss decay of azulene via 3 or 4- photon absorption mechanism at 235-290nm

Since both naphthalene and azulene in cationic form are very well studied systems in terms of their internal energy dynamics, it is possible to obtain internal energy values for the observed H loss decays. The details of this estimation are evident in the later sections. These internal energy values plus the required ionization energy at 235 to 256 nm are such that the observed decay rates at these wavelengths are energetically possible via a 3-photon process. Indeed, the appearance energy of the H-loss fragment in a single VUV photon ionization experiment of azulene is around 14 eV, which corresponds to 3-photon absorption at 265 nm[57]. As we cross 256 nm to longer wavelengths the 3-photon induced H loss decay starts to slow down in such a way that the decay will not be completed within the time window available to the spectrometer. To illustrate this, the ratio of slow to fast H loss yield is plotted in figure 6.3(a). The ratio is systematically increasing in the wavelength region, 235-256nm as expected from 3-photon absorption with a decreasing internal energy of the cation. The 3-photon process in this wavelength range is separately confirmed by the laser intensity dependence of H loss fragment ion signal as shown in figure 6.3(b). The relative contribution of the 4-photon dominated H loss process is negligible at this wavelength region 235-256nm. But after 256 nm the ratio decreases very rapidly indicating
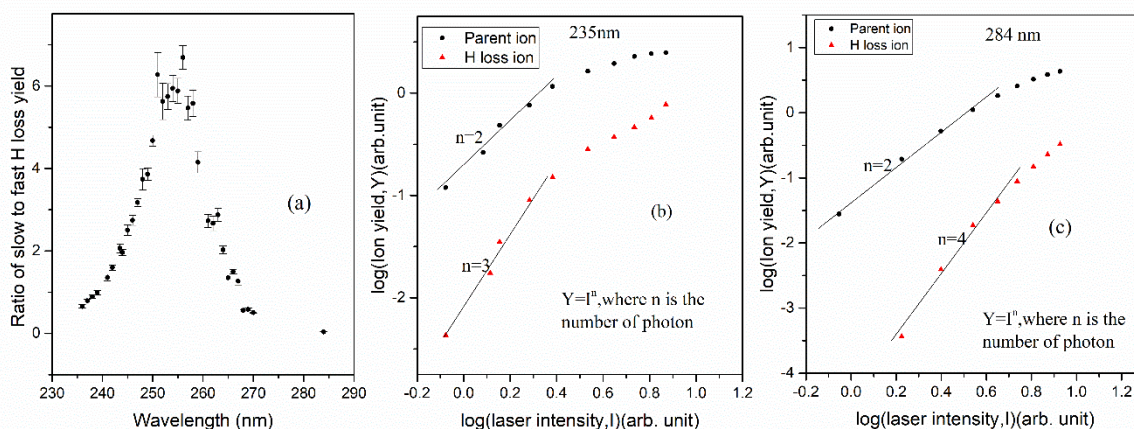


Figure 6-3: (a) Ratio of slow to fast H loss yield measured at a range of wavelength 235nm-284nm, intensity dependence of single ionization of $C_{10}H_8$ and H loss fragmentation yield (both slow and fast contribution) at (b) 235nm and (c) 284nm Solid lines are fits of the $C_{10}H_8^+$ and $C_{10}H_7^+$ data according to indicated power law.

an increase in the fast H-loss fraction. To explain this wavelength dependency, we invoke the contribution of the 4-photon absorption process for the decay observed beyond 256 nm. The extra energy added in the 4-photon process (about 4eV) produces a strong fast peak. The transition from 3 to 4-photon driven H loss yield is shown in figure 6.3 (b) & 6.3 (c). From 284nm onwards only fast H loss peak was observed in the mass spectrum as the 3-photon dominated decay was too slow to be observed in the available time window.

Kinetic energy distribution (in the horizontal position coordinates) of the H loss fragments, illustrating the evolution of slow and fast H loss peaks as we increase the wavelength (from 235nm to 290nm) is shown in figure 6.4. In fig 6.4 (c), the slow H loss peak has completely vanished at 290nm, indicating the disappearance of 3-photon dominated H loss decay in the time scale available to the spectrometer at longer wavelengths.
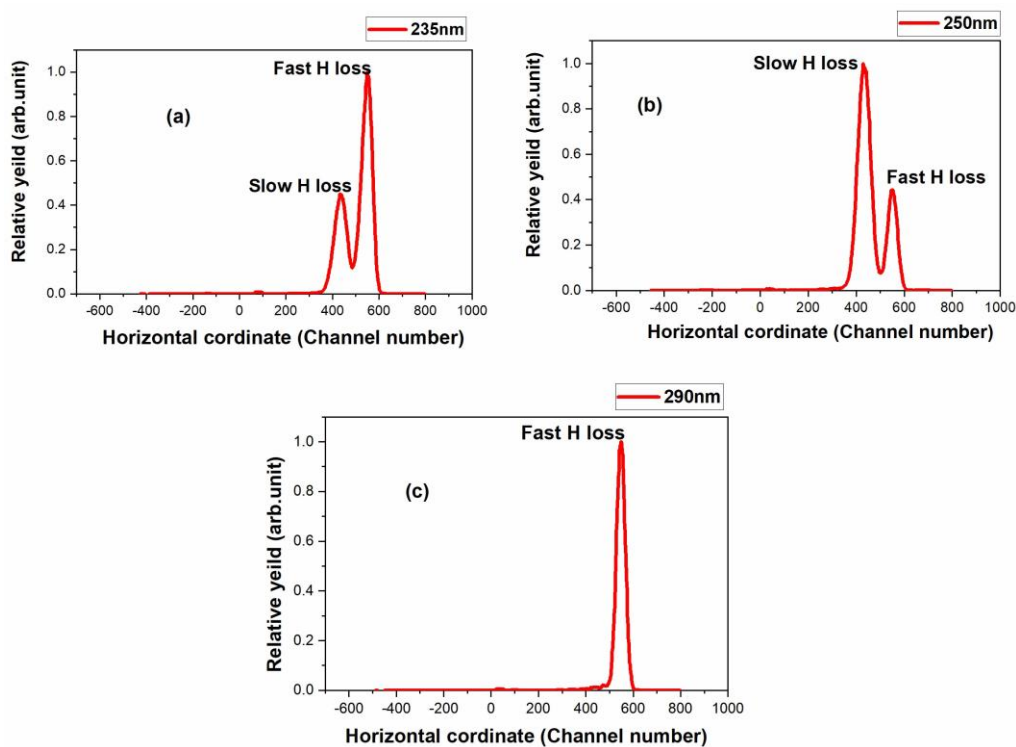


Figure 6-4: KE distribution of H loss fragments showing evolution of slow and fast H loss peak as a function of wavelength.

## 6.4 Production of narrow IED of azulene[+] via $S_2$ ionization and excitation mechanism

Let us now examine the 3-photon ionisation and excitation of azulene at 235-256nm. One colour 2-photon ionisation mechanism of the azulene molecule has already been investigated in detail using ps and femtosecond (fs) lasers by pump-probe techniques[84–87]. These experiments have identified electronic excited states of azulene and characterized their relaxation mechanism by time dependent probe photon ionization. P.M Weber *et al*[85] measured the photoelectron spectra of azulene obtained upon ionizing the molecule via the $S_3$ and $S_4$ states with a transform limited ps pulse. In this work, $S_2$ ionisation was identified for both the cases from the photoelectron energy spectra of both the cases. It was demonstrated in those experiments that vibrationally hot molecular ions were produced due to fast internal conversion from $S_n$ to $S_2$ (S denotes singlet electronic states of neutrals) and subsequent second photon ionization to $D_0$ (D denotes doublet states of the cations) while satisfying the propensity rule, $\Delta v \approx 0$ (where $v$ is the vibrational quantum number). V. Blanchet *et al*[86,87] have performed 1+1 photoionization experiments via $S_4$ states using a fs pulse with a wavelength centered at 266nm and 258nm and identified a significant contribution of the photoelectron signal arising from $S_4$ to $D_1$ ionization. In their experiment photoionization takes place on a time scale commensurate with internal conversion. It helped them to set an upper limit ($\approx$120fs) to the lifetime of $S_4$ and thus, the timescale of IC.

Thus, it is understood from the past results that the IC time scales from the $S_n$ to $S_2$ states are <120fs. In our experiment, with a ns pulse duration, we can safely assume that the $S_n$ to $S_2$ relaxation competes very efficiently with a direct ionisation from the $S_n$ state (see path (a) in figure 6.5) and is totally completed before ionisation from a vibrationally excited $S_2$ state takes place (path 6.5 (b) in figure 6.5). Further, $S_2$ to $D_0$ ionization satisfies the $\Delta v \approx 0$ rule (see path (b) in figure 6.5). Azulene[+] can be further excited by third photon and can relax back to ground electronic state $D_0$ by rapid IC. These extremely hot azulene[+] undergo IVR and relax by various statistical processes such as isomerisation and dissociation.

The $\Delta v \approx 0$ propensity rule of ionisation, allows to estimate the internal energy of azulene[+] after ionization and 3rd photon absorption. This internal energy is in the range of 6.98 to 6.12 eV for 235-256 nm. The H loss rate constants of azulene[+] measured by the present set-up for internal

energies proposed by the $S_2$ ionization scheme (path b) is given in table 6.1. It can be compared to the extensive calculations of isomerisation and dissociation rate constants of azulene[+] for a range of internal energies 5-12.5eV carried out by Dyakov *et al*[28].
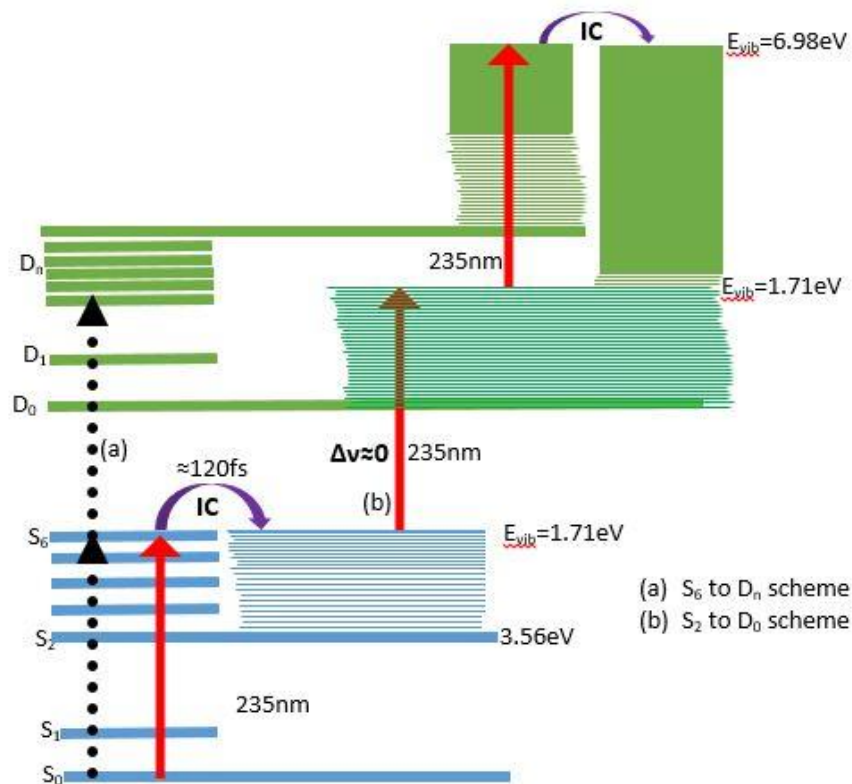


Figure 6-5: Schematics of $S_2$ to $D_0$ ionization at 235nm, in azulene the dotted black arrows show direct two photon ionsaition (path a) and the three set of continuous red arrows show the multipstep 3 photon ionaition-exacitation path (path b).

Table 6.1: (a) H loss rate constants measured in the present experiment for internal energies proposed by the $S_2$ ionization scheme is compared with (b) calculations of isomerization and H loss rate constants of azulene[+] by Dyakov *et al* for the relevant internal energies[28].

| Present experiment (a) | | | Calculation Dyakov *et al.* (b) | | | |
|---|---|---|---|---|---|---|
| Wavelength (nm) | $E_{int}$ (eV) of azulene[+] | Diss. Constant of H loss (s[-1]) | $E_{int}$ (eV) of azulene[+] | Direct H loss rate (s[-1]) | Isomer. rate (s[-1]) | Reverse isomer.rate (s[-1]) |

| 235 | 6.98 | $1.5 \times 10^6$ | 7.99 | $2.0 \times 10^5$ | $8.7 \times 10^7$ | $1.3 \times 10^7$ |
|-----|------|-------------------|------|-------------------|-------------------|-------------------|
| 256 | 6.12 | $2.3 \times 10^5$ | 6.42 | $2.8 \times 10^2$ | $2.8 \times 10^6$ | $2.3 \times 10^5$ |

As per the calculation carried out by Dyakov et al,[28] it is clear that azulene$^+$ to naphthalene$^+$ isomerisation is the dominant process for the expected internal energies. The most recent computations and experiments show that the transition barrier of isomerization of azulene$^+$ to naphthalene$^+$ lies below the low energy dissociation limits of the azulene ion[27,28]. W. Cui et al[31] have performed a time resolved photo dissociation experiment for the azulene$^+$ and naphthalene$^+$ ions and observed that the acetylene loss channels (which is another low energy parallel dissociation channel) of these isomeric ions are measured to have similar decay rates at a deficit of internal energy by about 0.8eV for azulene$^+$ (In this experiment $E_{int}$(azulene$^+$)=6.2eV and $E_{int}$ (naphthalene$^+$)=7eV). This is explained on the basis of fast conversion of azulene$^+$ to the lowest energy isomer naphthalene$^+$ prior to dissociation at the relevant internal energies. In a couple of experiments and high level computations the isomerization energy of azulene$^+$ to naphthalene$^+$ is independently predicted to be about 0.8eV[28,59]. As per calculations by Dyakov et al. [Ref 28, Table.3], isomerisation of cationic azulene is at least two orders of magnitude faster than its direct H loss for the internal energies expected from the 3-photon absorption scheme [See table 6.1]. In conclusion, for our experimental timescales (about tens of μs) isomerization is dominating so that it produces naphthalene cations at elevated internal energies by about 0.8eV compared to azulene$^+$. Therefore, it can safely be assumed that whatever H loss process observed for the first few tens of μs is mainly coming from the naphthalene$^+$ isomer. Hence, hereafter we consider the dissociation curve of cationic naphthalene for further discussions.

## 6.5    Comparison of internal energy with $S_2$ ionization scheme

Gotkis et al[25] have modelled the time resolved break down curve of the H loss fragment ion of naphthalene$^+$ using rate-energy constants obtained via RRK*M/Q*ET calculations for a range of internal energies 4-12eV. The H loss dissociation curve of naphthalene$^+$ proposed by Gotkis et al is studied along with other advanced calculations carried out by Dyakov et al and Solano and Mayor[88]. The present experiment only measures rate constants of H loss decay at 235-256nm. The rate-energy calculations carried out for naphthalene$^+$ by Dyakov et al. were used to convert

this information into corresponding internal energy with the help of necessary interpolation. Dissociation rate $k(E)$ and corresponding internal energy ($E_{int}$) identified from previous calculations is listed in table 6.2. As discussed before, we extend $S_2$ to $D_0$ ionization scheme as suggested by P.M Weber $et\ al$[84] to all the measured wavelengths as shown below to predict the internal energy of azulene$^+$ after successive absorption of 3-photons.

$$E_{S2\text{-}D0}\ (azulene^+)=[E(photon) - S_2(v=0)\ (3.56eV)]+E(photon) \qquad (6.1)$$

Where, $\Delta v \approx 0$ is allowed and $S_2$ is the second electronic excited state energy. Therefore, internal energy of the isomerized ion, naphthalene$^+$ will be

$$E_{S2\text{-}D0}\ (naphthalene^+) = E_{S2\text{-}D0}\ (azulene^+)+ E_{iso}\ (0.8eV) \qquad (6.2)$$

Where, $E_{iso}$ is the isomerisation energy.

Table 6.2: Dissociation rate constants measured in the present experiment are listed along with the corresponding internal energy, $E_{int}$ identified from the H loss dissociation curve of naphthalene$^+$. Internal energy predicted as per $S_2$ to $D_0$ ionization scheme is shown.

| Wavelength (nm) | Dissociation rate experimentally measured $k(E)$, (s$^{-1}$) | Estimated Internal energy ($E_{int}$) of naphthalene$^+$, (eV) | Estimated Internal energy via $E_{S2\text{-}D0}$ (naphthalene$^+$) (eV) |
|---|---|---|---|
| 235.0 | $1.50 \times 10^6$ | 7.97 | 7.80 |
| 236.0 | $1.46 \times 10^6$ | 7.96 | 7.74 |
| 237.0 | $1.45 \times 10^6$ | 7.96 | 7.70 |
| 238.0 | $1.20 \times 10^6$ | 7.89 | 7.66 |
| 239.0 | $1.00 \times 10^6$ | 7.82 | 7.62 |
| 240.0 | $9.00 \times 10^5$ | 7.78 | 7.58 |
| 241.0 | $8.80 \times 10^5$ | 7.78 | 7.52 |
| 242.0 | $8.00 \times 10^5$ | 7.74 | 7.48 |
| 243.0 | $6.50 \times 10^5$ | 7.67 | 7.44 |
| 243.5 | $6.50 \times 10^5$ | 7.66 | 7.42 |
| 245.0 | $5.60 \times 10^5$ | 7.61 | 7.36 |
| 246.0 | $5.00 \times 10^5$ | 7.58 | 7.32 |
| 248.0 | $4.00 \times 10^5$ | 7.50 | 7.24 |

| 250.0 | $3.30 \times 10^5$ | 7.43 | 7.16 |
| 252.0 | $3.00 \times 10^5$ | 7.40 | 7.08 |
| 254.0 | $2.72 \times 10^5$ | 7.37 | 7.00 |
| 256.0 | $2.30 \times 10^5$ | 7.32 | 6.92 |

$E_{int}$ identified in the experiment by comparing the measured rate constants with the calculations done by Dyakov *et al* is compared with the value predicted by $S_2$ to $D_0$ ionization schemes for 235-256nm as shown in figure 6.6. The average internal energy deduced from the present experiment is in qualitative agreement with the $S_2$ to $D_0$ ionization scheme for 235-256nm, though the estimates are systematically higher by about 0.25 eV compared to the values predicted by the $S_2$ to $D_0$ ionisation model.

The experimental $E_{int}$ values identified from earlier rate- energy results lie above the $E_{int}$ curve modelled via the $S_2$ to $D_0$ ionization scheme. If the rate-energy calculation is not precise enough, it can introduce a systematic error in the experimental $E_{int}$ values. At this juncture, a few other possible reasons can also be proposed for such higher internal energies. It is possible that various vibrational levels in the $S_2$ manifold are involved in the ionization scheme, Moreover, the higher the vibrational energy in the $S_2$ state, the more difficult it is to fulfill the $\Delta v \approx 0$ transition. Hence, other energetically allowed ionization transitions can gain significant intensity through a vibronic coupling between nearby electronic states. Similar ionization via the $S_1$ band is observed for naphthalene[89]. It may also be noted that for wavelength shorter than 250 nm the $D_1$ ionisation also becomes energetically feasible. Though, the $\Delta v \approx 0$ transition between $S_2$ and $D_1$ have never been experimentally observed, it is still offered as a possible contributing mechanism here only on the basis of energetics. If such propensity is assumed for the $S_2$ to $D_1$ transition then the resulting internal energy will be consistently higher by about 1.1 eV and cause much faster decay [electronic energy level of excited azulene$^+$ is taken from Table. 1, Ref. 86]. Estimates of $E_{int}$ under this assumption are plotted in figure 6.6 for reference. After all, it may be noted that the experiment was done using azulene vapour at room temperature and considering the total degrees of freedom, about 0.3 eV internal energy can already be there in the molecular gas.
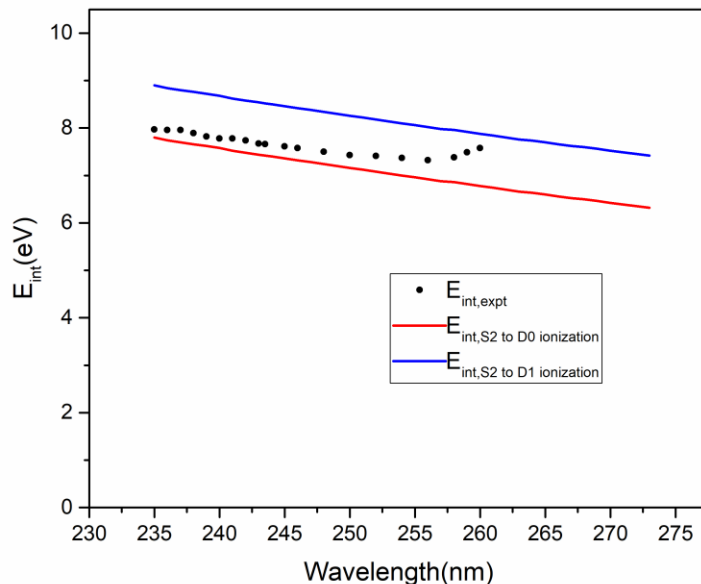
Figure 6-6 Internal energy of naphthalene$^+$ deduced from the experiment (black circles) for 235-260nm and predicted via $S_2$ to $D_0$ (red line) and $S_2$ to $D_1$ (blue line) ionization of *azulene$^+$* is plotted. $S_2$ ionization schemes serve as limits to the internal energies. Experimentally estimated internal energy follows the $S_2$ ionization scheme for wavelength<256nm. For wavelength>256nm, the experimentally deduced internal energy values are overestimated by the fact that in this region H loss decay is mainly driven by 4-photon process, it is an accordance with figure 6.3 (a).

## 6.6 Extension of data analysis and discussions

With the experience form the previous sections a further augmentation of the analysis was attempted. This was doen by including the tail region of the 2D correlation. Moreover this procedure was extended to tow more targets namely naphthalene and fluorene. ToF spectra of fluorene and azulene is shown in figure 6.7. The mass resolution is well beyond 1 in 3000 so as to clearly separate the various H, 2H/$H_2$ loss as well as isotopic peaks. The high energy resolution of the instrument makes sure that a 0.24% shift in the KE produces a clearly separated feature on the PSD. The ToF information is very limited and pertains to the dynamics in ER and AR only. A KE correlated ToF spectrum is a two dimensional correlation between the measured KE and ToF is much more illustrative for the decay at later times. A typical 2D spectrum of ToF versus

horizontal position of the naphthalene target is shown in figure 6.8. As explained in previous chapters, the horizontal position of an ion on the PSD is proportional to its kinetic energy. The parent peak is seen as a single island (region 1) with horizontal position corresponding to full kinetic energy. The possible origin of multiple H loss peaks are already discussed in the context of delayed dissociations in detail in sec 3.2.5 of chapter 3. For the purpose of clarity, it is restated briefly here. The H loss decay constant (k) of the parent ion must be at least $1000 \text{ s}^{-1}$ to show any discernible signal of H loss decay in our instrument leading to a feeble tail in the region 5 and a low intensity slow H loss peak (peak 3) in the 2D spectrum. H loss decay rates lies between $k=10^4 \text{s}^{-1}$ and $10^5 \text{s}^{-1}$ strongly populates slow H loss peak and tail region. The "fast H loss peak" (peak 2) becomes more visible for $k>10^5 \text{s}^{-1}$. The tail region 5 completely disappears for $k>3 \times 10^5$ $\text{s}^{-1}$. Slow and fast H loss peaks become comparable for $k=10^6 \text{s}^{-1}$. Beyond this H loss decay rate, the fast peak will dominate over the slow peak. Thus, every populated region in the 2D graph points to a narrow range of decay constants. The 2D landscape can become very complex if multiple or broad internal energy ensembles are prone to decay, because the decay rate varies very rapidly with a small change in the internal energy. Hence, if only selected regions are populated, it directly implies a relatively narrow range of decay constant and hence very narrow range of IED.
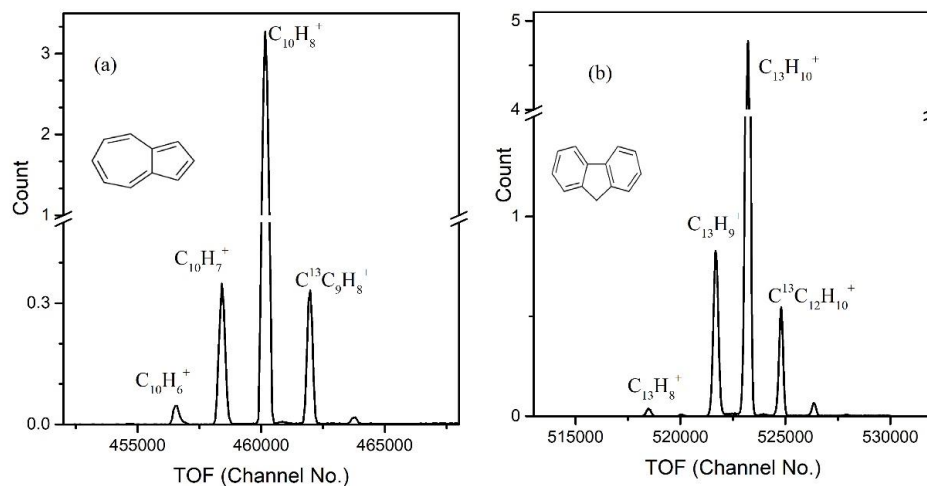


Figure 6-7: ToF spectrum of (a) azulene and (b) fluorene recorded at 263nm and 235nm with an intensity of $9 \times 10^9 \, \text{W/cm}^2$.
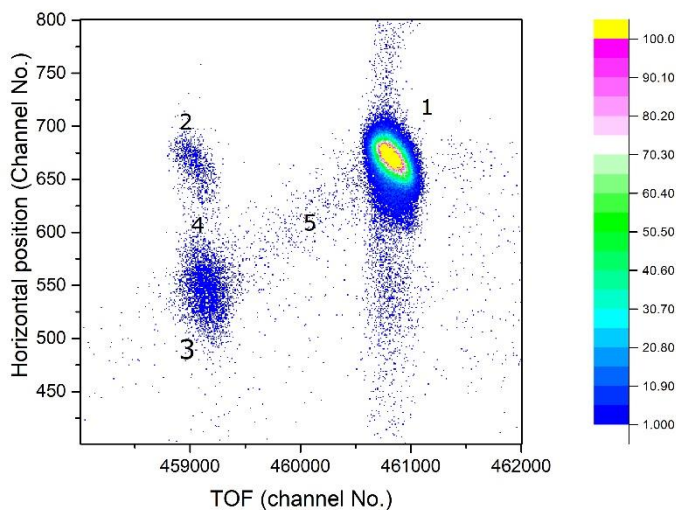
Figure 6-8 : 2D diagram for ToF vs horizontal position (horizontal position on y-axis, scale to the kinetic energy of the ion) of parent and H loss fragment ion of naphthalene measured at 225nm and $10^9$ W/cm$^2$. Naphthalene parent ion is marked as "1", Peak "2" corresponds to H loss decay in the ER, Peak "3" is decay inside drift tube, Region "4" is the decay in AR and decay inside PPA is marked as "5".

Here we have used two methods to estimate the H loss decay rate depending on the locations where the H loss fragment is populated in the 2D diagram and the UV excitation wavelength. Usually the ratio between the fast and slow H loss peak yields is reproduced in the simulation by assigning suitable rate constants of the decay. This type of analysis ("peak analysis") is employed for shorter wavelengths, because at such wavelengths the fast and slow H loss peaks will be normally populated because of the availability of high internal energy. If the H loss fragment population is shifted to the tail region, which usually occurs for longer wavelengths (due to the low internal energies), "tail analysis" becomes more useful. In this case, the relative yield of the tail region with respect to the slow H loss peak is reproduced in the simulation in order to identify the corresponding rate constant. The decay rate which gives best fit to the relative population of H loss fragments at the different regions of 2D diagram is compared to the previously published rate-energy curves of the H loss decay in order to identify the corresponding internal energies. Thus, internal energies of naphthalene, azulene and fluorene are obtained over a broad range of UV wavelengths. The minimum value of decay rate that can be measured using this technique is about k≈$10^3$ s$^{-1}$. Therefore, those UV wavelengths were used

in this experiment which can produce 3-photon assisted measurable H loss decay features in the 2D coincidence diagram.

## 6.7    Results and discussions

The three photon assisted H loss decay channel is measured for fluorene[+] for an excitation wavelength ranging from 253-293nm. Similar H loss decay is observed for naphthalene[+] and azulene[+] for a range of excitation wavelength 235-273nm and 225-238nm respectively. In a single VUV photo-ionisation experiment, the appearance energy of the H-loss fragment ion for a typical neutral PAH is around 15 eV[57], which corresponds to 3-photon absorption at 250 nm. The three photon process is separately verified by laser power dependence of the H loss ion signal for three of the PAH targets. At the longer wavelength region the H loss signal is still detectable in the fast H loss decay peak, because of the contamination from higher order photon process. The present electric field configuration of the spectrometer is not adequate to resolve such a rapid decay caused by higher energy depositions. Therefore, we restrict our measurement to resolvable microsecond decays, which is governed by three photon absorption.

The H loss channel is one of the lowest energy dissociation channels of PAHs. Fluorene[+] has the lowest H loss threshold of the systems reported here, with 2.6eV[30]. H loss thresholds of cationic azulene and its low energy isomer naphthalene is very high, about 5eV. Interestingly, isomerization barrier of these cationic pair lies below H loss dissociation limit and hence, it is expected that internally excited azulene[+] undergoes isomerization prior to the  dissociation and increases its internal energy by about 0.8eV[28].

## 6.8    Ionization and excitation scheme of PAHs by a single ns pulsed laser

It is rather clear from the measurements that for all three targets investigated, the decay constant cannot be broader than about one order of magnitude, else the 2D correlation graph would take a much different form. This in turn indicates that the parent ions are produced with an internal energy spread much less than 1eV.  A direct 3-photon absorption is possible but it will lead to a very broad internal energy distribution. Moreover, the present experiment is performed at very low intensities, hence, we invoke more appropriate scheme analogous to ladder switching mechanism, to explain the observed narrow IED. A multistep ionization and excitation scheme

is proposed, considering the excited state dynamics of PAHs to explain the three photon driven H-loss process for all the three targets during ns pulse duration. An excitation to the $S_n$ state by the first photon will be followed by IC to the lowest excited electronic state $S_1$ ($S_2$ in case of azulene). In the case of PAHs, it is known that the ionisation from the $S_1$ state satisfying $\Delta v \approx 0$ rule (propensity rule) will be caused by second photon absorption[85,90,91]. This will then be followed by third photon absorption by the cation and add internal energy to the ground cationic state of the molecule by the process of rapid IC in PAH cations. The propensity rule ensures that the photoelectron energy distribution can be very narrow[85]. Even if the ionisation process by the second photon proceeds via non-adiabatic mechanism, the structural rigidity of PAHs makes sure that the deviation from the propensity rule is minimal in nature ($\Delta v \approx 0, \pm 1$)[85,90–92].

For a given photon energy, the excited electronic states of the cations are accessible while preserving the vibrational quantum number. The exact distribution of intensity among the various cationic states is not only a function of photon energy but also structural similarity between the excited electronic state and respective cationic state of the molecule. Here we consider only energetics of the process in the absence of an actual measurement of such an influence of different excited electronic states of the cation. Thus, if multiple cationic states are possible to be involved in the ionization, then more than one group of IED will be produced. In case of fluorene two electronically excited states ($D_1$ and $D_2$) of the cation are energetically accessible for the studied wavelength range and the maximum spread of internal energy can be found to be at most 1.18 eV. This number can be brought further down if we can set the excitation wavelength appropriately to cover fewer, preferably single cationic state. In the present case the time window available to our setup limits the observation of such slow dissociations induced by longer excitation wavelengths. But it can be studied easily by employing similar scheme with an ion storage ring system. Incidentally we could exploit isomerization of internally excited azulene$^+$ to naphthalene$^+$ for the available energies, which helped to perform a common analysis to both of them. The elaborate details of H loss decay of azulene$^+$ caused by nanosecond multistep multiphoton absorption is given in chapter 6.

### 6.8.1    One colour multistep 1+1+1 absorption process: Naphthalene

In case of naphthalene, the 3-photon ionization and excitation scheme for the shortest wavelength, 225nm is described as follows.

$S_0 \xrightarrow{\text{225nm}} S_n \longrightarrow S_1 (v=0)+E_{vib} (1.55eV) \longrightarrow D_0 (v=0)+ E_{vib} (1.55eV)+1.33eV$

225nm & IC

$D_0 (v=0)+ E_{vib} (7.06eV)$

225nm, $\Delta v \approx 0$

$D_1 (v=0)+ E_{vib} (1.55eV)+0.63eV$

225nm & IC

$D_0 (v=0)+ E_{vib} (7.76eV)$
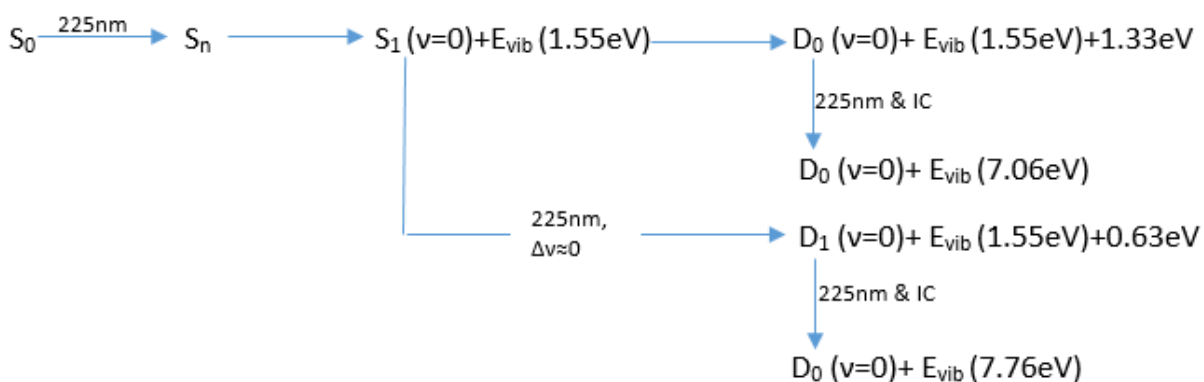
The first photon leads to $S_n$ excitation followed by rapid IC to the $S_1$ state at 3.96eV. Thus, the residual energy of 1.55eV is left in the vibrational modes of $S_1$. The second photon causes ionisation from $S_1$ to $D_0$ while preserving the vibration quantum number. Using adiabatic ionisation potential of 8.14eV, we deduce the energy of the outgoing electron to be 1.33 eV. Thus, the $S_1$ ionization leaves internal energy of 1.55eV in the parent ion. Some of these parent ions can be further excited by a third photon and relax by IC and thereby produce a hot cation of naphthalene at 7.06eV internal energy. The $D_1$ state of naphthalene is situated at 0.7eV above $D_0$[93]making it also energetically accessible for $S_1$ ionization over the whole range of wavelengths (225-238nm) investigated here for naphthalene. Thus, there should be two closely spaced groups of cations formed with IED centred at two internal energy values namely 7.06eV and 7.76eV in case of 225nm. The initial thermal distribution as well as deviation from $\Delta v \approx 0$ rule might cause some more broadening and mixing of the ensemble. The average internal energy deduced from peak analysis and tail analysis lies between the internal energies proposed by $S_1$ to the $D_0$ and $D_1$ ionization scheme except the $E_{int}$ deduced at 237nm from peak analysis. In case of naphthalene, it is observed that 3-photon induced H loss decay efficiently populates the tail region rather than the H loss peaks for wavelength>237nm. Therefore, the H loss rate constant is measured from tail analysis at 238nm. As can be seen from figure 6.9, internal energy estimates carried out by
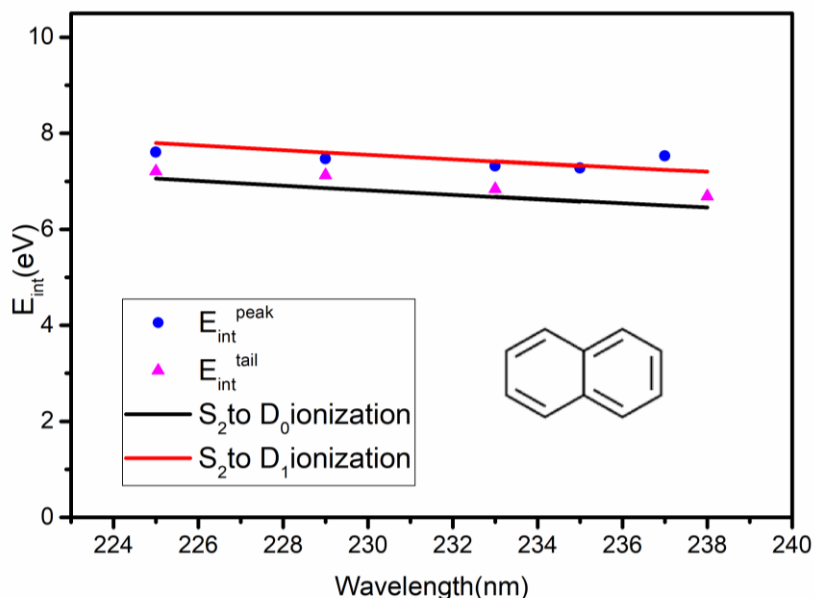
Figure 6-9 : Experimentally deduced internal energy is compared with multistep 3-photon ionization and excitation scheme for naphthalene for 225-238nm

peak and tail analysis are remarkably consistent with the $S_1$ to $D_0$ and $D_1$ ionization scheme for 225-238nm.

### 6.8.2    One colour multistep 1+1+1 absorption process: Azulene

Azulene$^+$ is a well-known counter example of Kasha's rule. Hence, the first photon excitation to the $S_n$ state quickly proceeds via IC to the $S_2$ state instead of the lowest electronically excited state, $S_1$. This is followed by ionisation to the $D_0$ state maintaining $\Delta v \approx 0$. Unlike the other two examples investigated here, azulene$^+$ is a very well-studied system and the ionisation process is characterized for the very narrow internal energy distribution employing time resolved pump-probe photoelectron spectroscopic experiments[85,86,90]. Though, the $D_1$ state of azulene is energetically accessible at the range of UV wavelength used, such ionisation channel is not observed experimentally[86]. In case of azulene, we have estimated internal energies for a wide range of wavelength (235-273nm) as shown in figure 6.10. The method of peak analysis is employed to deduce the internal energy for shorter wavelengths (235-256nm) and tail analysis is used for longer wavelength region (256-273nm). Unlike in the case of naphthalene $E_{int}$ estimates of azulene lies very close to the $S_2$ to $D_0$ ionization scheme. It supports the production of very

122

narrow internal energy distribution proposed by peculiar $S_2$ to $D_0$ ionization scheme of azulene. Internal energy expected from $S_2$ to $D_0$ and $D_1$ ionization scheme and further heating by third photon absorption and subsequent isomerization to naphthalene$^+$ at 235nm is shown in the schematics for 235nm.

$$S_0 \xrightarrow{235nm} S_n \xrightarrow{IC} S_2\,(v=0)+E_{vib}\,(1.71eV) \xrightarrow[\Delta v \approx 0]{235nm,} D_0\,(v=0)+E_{vib}\,(1.71eV)+1.44eV$$

235nm & IC

$$D_0\,(v=0)+E_{vib}\,(6.98eV+E_{iso})$$

$$\xrightarrow[\Delta v \approx 0]{235nm,} D_1\,(v=0)+E_{vib}\,(1.71eV)+0.33eV$$

235nm & IC

$$D_0\,(v=0)+E_{vib}\,(8.08eV+E_{iso})$$

Where $E_{iso}=0.8eV$.

The peak analysis provides an excellent match with the $E_{int}$ values predicted by the $S_2$ to $D_0$ ionization scheme upto 256 nm wavelength. Beyond this wavelength, the internal energy values



Figure 6-10: Experimentally deduced internal energy is compared with multistep 3-photon ionization and excitation scheme for azulene for 235-273nm.

start being overestimated due to 4 photon contamination. At this stage the tail analysis become more viable and provides usable information upto 273nm. It may be noted that tail analysis is

also prone to contamination from collision induced dissociation at the used level of background pressure which could explain the relatively small ($< 0.3$ eV) systematic underestimates as shown in figure 6.10. Never the less, the dominance of $S_2$ to $D_0$ ionization in the multistep multiphoton absorption of azulene is clearly established in these measurements.

### 6.8.3 One colour multistep 1+1+1 absorption process: Fluorene

Multistep 1+1+1 ionization and excitation scheme of fluorene is described for the shortest wavelength, 253 nm as shown below,
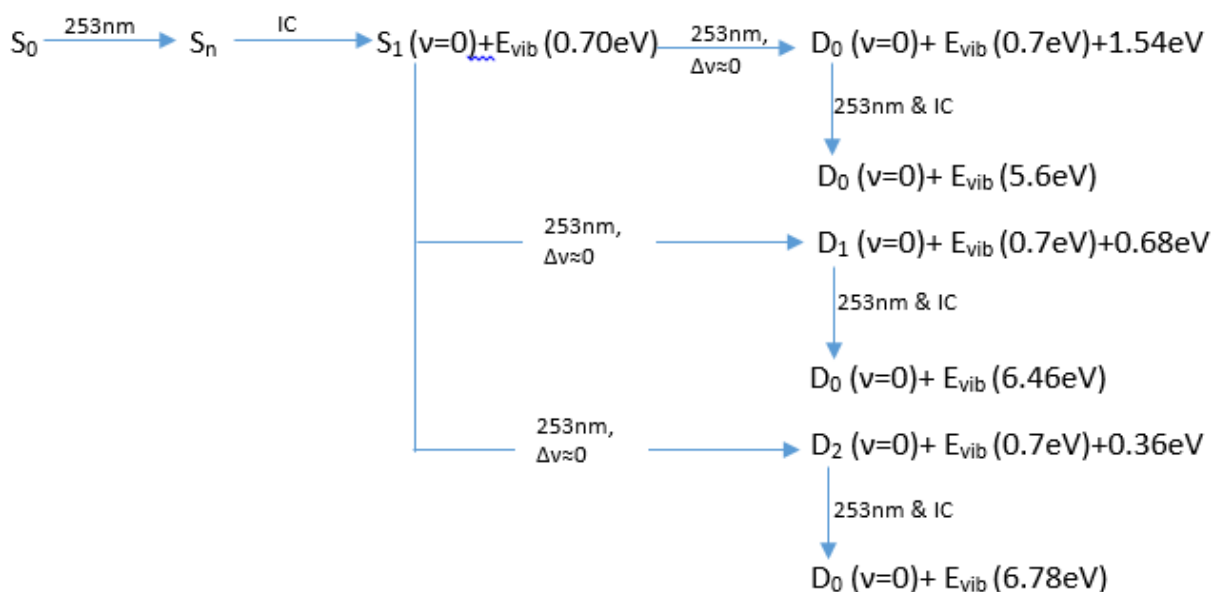


At 253nm, $S_1$ to $D_0$ ionization of fluorene leaves a residual of 0.7eV in the vibrational modes of fluorene parent ion, further excitation by third photon results in an internal energy of 5.6eV in fluorene$^+$. The $D_1$ and $D_2$ states of fluorene are situated at 0.86 and 1.18 eV above the $D_0$ state[94], and hence, they are also energetically available for $S_1$ ionization in case of 253nm. Thus, we expect three closely spaced groups of cations formed with IED centred at three internal energy values namely 5.6eV, 6.46eV and & 6.78eV. For fluorene, we have proposed the $S_1$ to $D_0$, $D_1$ and $D_2$ ionization scheme for a range of wavelength 253-293nm, since gap between D1 and $D_2$ is very small. The $E_{int}$ estimations carried out by peak analysis (for 253-273nm) suggests that the

ionization can be dominated by the $S_1$ to $D_2$ transition (see figure. 7.5). But internal energy deduced from tail analysis lies below $E_{int}$ curve proposed by the $D_0$ ionization scheme. Deviation of experimentally deduced internal energies from proposed ionization and excitation mechanism can be due to other effects like collision induced dissociation or internal excitation by $4^{th}$ photon. But, as demonstrated in the case of azulene, the contamination from four photon absorption would cause a systematic deviation in the result obtained from peak analysis, compared to the scheme prediction (see wavelength region between 251 and 256 nm in figure 6.10). In the case of fluorene, the peak analysis follows predictions of $D_2$ ionization very closely (See figure 6.11). On the other hand the tail analysis is affected by collision induced dissociation. This effect is there for other examples as well. But in the case of fluorene we expect that it can be more severe due to its low H loss barrier and relatively larger collision cross section.
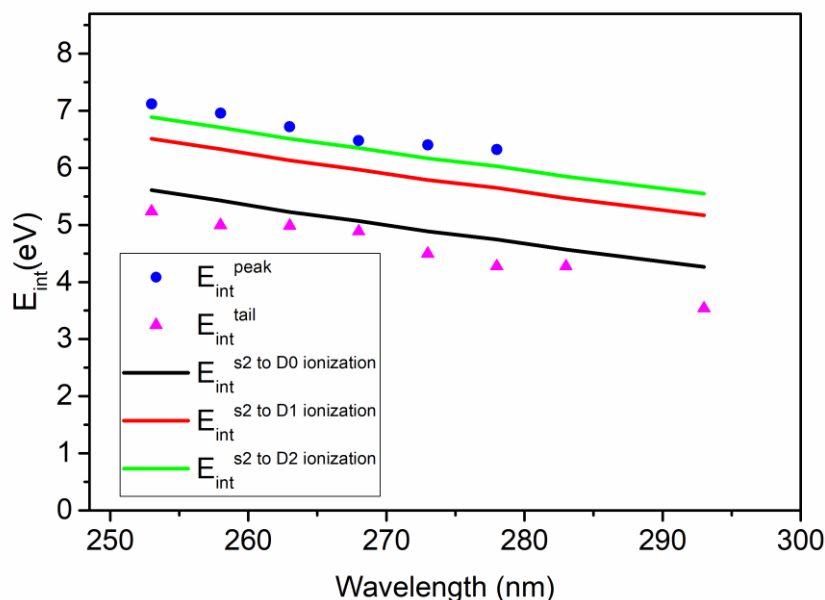


Figure 6-11: Experimentally deduced internal energy is compared with multistep 3-photon ionization and excitation scheme for fluorene for 253-293nm.

In conclusion, the fluorene cation formation is observed to favour $D_1$ or $D_2$ transition from the $S_1$ state. Though the observed internal energy values are very close to the $D_2$ scheme, there may be an effect of initial thermal energy in the vicinity of 0.3 eV and the energy difference between the

125

$D_1$ and $D_2$ cationic state is also about 0.3eV. The fluorene transition probabilities between the $S_1$ to $D_0$, $D_1$ and $D_2$ needs to be investigated independently and verified.

## 6.9    Summary

Internal energy dynamics of molecules under energetic radiation excitation is a very complex phenomenon in general. No study of this nature is complete, without correlated measurement of photoelectron energy. Even for single photon excitation or ionisation the residual internal energy depends on IC, IVR, fluorescence and photoelectron kinetic energy etc. Thus, quantification of internal energy after electronic excitation is a very complex task. On the other hand, understanding of the role of PAHs in astronomical and biological domain requires a detailed measurement of the decay rate as a function of internal energy. We demonstrate here that due to very specific excited state properties of PAHs, it is possible to employ a very simple multi-step multiphoton absorption scheme to obtain a relatively narrow IED. Three simple PAHs are used as targets namely, naphthalene, azulene and fluorene for a very wide range of UV wavelength (225-293nm).

The structural details and transition probabilities notwithstanding, we considered all possible excited electronic states of the cation, in all the three cases studied. Fluorene covered the greatest number of cationic states with $D_0$, $D_1$ and $D_2$ being energetically allowed to reach by the second photon from $S_1$ state at the studied wavelength range. It appears that $S_1$ to $D_1$ or $D_2$ ionization transition is favored over $S_1$ to $D_0$ ionization in case of fluorene. In case of azulene $D_0$ and $D_1$ states are energetically accessible from $S_2$ state for the studied wavelength range. Azulene is a well-studied system and $D_1$ ionisation channel of azulene is not spectroscopically observed before. Consistent with this, we also note that $S_2$ to $D_0$ ionization is the dominant channel and a minor excess energy could come from initial thermal energy in the target molecule. The final evidence of the validity of this approach comes from naphthalene wherein, $D_0$ and $D_1$ states are known to be accessed by second photon from $S_1$ state. The expected bimodal IED can be seen to be present in our observations as well. Thus, not only the predicted internal energies are compared with values deduced from experiment, the details like contribution from multiple cationic states could also be identified to an extent. This method can be very easily employed to tune the internal energy of $PAH^+$ down to hundreds of meV accuracies.

# CHAPTER 7. FUTURE SCOPES

The work presented here has highlighted the importance of various physical properties of PAHs, for example the role of plasmon excitation in isomerization process, the effects of isomerization and internal energy to the population distribution of ISM. These aspects are not systematically explored in the past, though they have been studied sporadically in different PAH examples. A systematic effect of this onto various applications require further investigations. Different techniques developed as part of this research can help in expediting such investigations and hence generate database for a generalized survey of afore mentioned effects.

The selection rules and other complications due to photoionization processes prohibits us to investigate multiplasmon excitation by conventional UV or VUV photoexcitations. But charged particle excitation is a good way to study multiplasmon resonances in PAHs. If we can do a triple coincidence experiment with charged particle excitation, we can target secondary effects of multiplasmon resonances in PAHs. Moreover, the effects of electron capture are not investigated in the context of statistical dissociations in PAHs. Therefore, multicoincidence experiments are very relevant in such investigations. It is well known that PAHs undergo large amount isomerization, this can strongly be coupled with charged particle interactions. This needs to be interrogated in detail. The same study has to be expanded to heterocyclic ring and can finally be reached to the response of biomolecules in charged particle excitations.

When it comes to understanding the behavior of molecules against high energy radiations, we need to vary the excitation energy and look for possible molecular damages. It is conventionally carried out by photon impact experiments. A standard pump probe experiment has to be extended to many of these molecules for a good understanding of multiphoton excitations and ionizations of PAHs particularly about their propensity rules of ionizations. Moreover, the techniques we have introduced here to produce cold molecular ions, needs to be coupled with storage rings. For standard storage ring experiments, PAH cations at known and narrow IEDs can be very easily produced by 2-photon multistep excitations without doing any complicated ion trap cooling. We can directly inject them into an ion storage ring and excite them

by IR photons. If it can be realized, PAH investigations become truly table top, because many of the compact ion storage devices usually work with complicated ion sources and traps.

The energy correlated ToF technique developed as part of this work is not exploited to its full potential. It is only applied to the H loss channel of PAHs. Though it is understood that sequential and concerted H loss can be very easily differentiated with this technique, this needs to be applied appropriately to study 2H or $H_2$ loss processes of PAHs. It is foreseen that other important statistical dissociation channels such as HCN loss, $C_2H_2$ loss can also be studied with this energy correlated ToF coincidence techniques. Deuterated PAHs are other potential candidates, which can give more pronounced information about the molecular dynamics of PAHs. It can be targeted with this high resolution technique. Another core capability of this instrument is the ion-neutral coincidence, which can be employed to understand conformations of the molecule from which neutral elimination has happened. If kinetic energy distributions of fragment ions in coincidence with position correlated detection of neutrals can be targeted, we can explore ground or excited state potential energy surfaces of larger molecules. It will be a powerful tool in the field of molecular physics. This information is very crucial to understand PAH dynamics in the astronomical context. But the geometric and electric field configurations of the setup need to be refined in future to target such sensitive measurements to extract vital information regarding dynamics of larger species.

# APPENDIX A. MC SIMULATION FOR MOLECULAR DECAY INSIDE SPECTROMETER

```cpp
#include<iostream>
#include<cmath>
#include<ctime>
#include<cstdlib>
#include<fstream>
#include <iomanip>
int main(){
using namespace std;
ofstream file1;
file1.open("n");
ofstream file2;
file2.open("t");
ofstream file3;
file3.open("r");
long double
aem2,T,tof,s,m,fe,e,fa,E,ae,am2,te,u,aa,ta,v,te1,pr,er,te2,g,Rp,m2,b,v1,t1,t2,y,R,theta,vy,vxy,ppa,ppaa,ze,za,zd,ue,ran,dd,volt1,volt2,vtemp;
int q,j,p;
g=3* pow (10,-3);  // thickness of acceleration plate
m=128*1.67* pow(10,-27); // mass of parent ion
m2=102*1.67* pow(10,-27);  // mass of fragment ion
e=1.60*pow(10,-19);  //charge
volt1=3000;  //voltage on the first plate of ER
volt2=2350;   //voltage on the first plate of AR
fe=(volt1-volt2)/0.007;  //electric field in ER
fa=volt2/0.007;  //electric field in AR
int n=100000; //no. of particles
ae=e*fe/m;
aa=e*fa/m;
am2=e*fa/m2;
aem2=e*fe/m2;
dd=138* pow (10,-3);  // width of PPA
ppa=e*1590/(m*dd);  //acceleration of parent ion due to PPA field
ppaa=e*1590/(m2*dd);  //acceleration of fragment ion due to PPA field
srand((unsigned)time(NULL));
for(int i=1;i<=n;i=i+1){
tof=0;
long double scale=RAND_MAX+1.0;
long double base=rand()/scale;
```

```
long double fine=rand()/scale;
long double u1=base+fine/scale;
base=rand()/scale;
fine=rand()/scale;
long double u2=base+fine/scale;
long double x=5.3+0.025*sqrt(-2.0*log2(u1))*cos(2*M_PI*u2); // defined to assign position
uncertainty of laser interaction using Gaussian distribution
long double s=x*pow(10,-3);
base=rand()/scale;
fine=rand()/scale;
long double u3=base+fine/scale;
base=rand()/scale;
fine=rand()/scale;
long double u4=base+fine/scale;
long double u0=150*sqrt(-2.0*log2(u3))*cos(2*M_PI*u4); // defined to assign directional
spread of velocity due to thermal effect
long double z=0;
long double u,t;
long double xpos=0;
long double y=2.0;
long double td=0;
long double tof1;
long double k=2.0e6;  //decay rate
long double dt=1e-11; //time step
long double pr=k*dt;
q=0;
j=0;
p=0;
int w=1;
for(t=0;y>=-1e-10;t=t+dt){
base=rand()/scale;
fine=rand()/scale;
ran=base+fine/scale;
if (z<=s){
u=u0+ae*t;
z=u0*t+0.5*ae*t*t;
if (z>s)
ze=z;}
else if((z>s)&&(z<(s+g))){
q++;
z=ze+u*q*dt;
if (z>s+g){
ze=z;
ue=u;}}
else if((z>=(s+g))&&(z<=(s+10*pow(10,-3)))){ j++;
u=ue+aa*j*dt;
```

```
z=ze+ue*j*dt+0.5*aa*j*j*dt*dt;}
else if((z>=(x+10)*pow(10,-3))&& (z<(790+x)*pow(10,-3))){
z=z+u*dt;}
else if (z>0.79+s){
td=w*dt;
y=0.707*u*td-0.5*ppa*td*td;
xpos=0.707*u*td;
R=xpos;
tof=t;
w++;}
if(ran<pr) // decay is checked {
if(z<=s)  // find ToF & range analytically, if particle is dissociating inside ER{
long double b=z/s;
long double v1=sqrt((2.0/m2)*((0.5*m*u0*u0+b*e*fe*s)*(m2/m)+(1-b)*e*fe*s));
long double t2=(v1-u)/aem2;
long double t3=g/v1;
long double vm2=sqrt(v1*v1+2*am2*7*pow(10,-3));
long double t4=(vm2-v1)/am2;
R=(vm2*vm2)/ppaa;
tof=t+t2+t3+t4+(0.78+R*1.414)/vm2;
file2<<i<<" "<<t<<" "<<tof*pow(10,6)<<" "<<z*pow(10,3)<<" "<<R<<" "<<endl;
break;}
if((z>s)&&(z<(s+3*pow(10,-3))))  // find ToF & range analytically, if particle is dissociating in
the ER plate{
E=(0.5*m*u0*u0+e*fe*s)*(m2/m)+e*volt2;
t2=(s+g-z)/u;
te=t+t2;
long double vm2=sqrt(u*u+2*am2*0.007);;
long double t3=(vm2-u)/am2;
R=(vm2*vm2)/ppaa;
tof=te+t3+(0.78+R*1.414)/vm2;
file2<<i<<" "<<t<<" "<<tof*pow(10,6)<<" "<<z*pow(10,3)<<" "<<R<<" "<<endl;
break;}
if((z>=(s+g))&&(z<=(s+10*pow(10,-3))))    //find ToF & range analytically, if particle is
dissociating inside AR{
b=(z-(s+g))*pow(10,3)/7.0;
long double v2=sqrt((2.0/m2)*((0.5*m*u0*u0+e*fe*s+volt2*b*e)*(m2/m)+(1-b)*e*volt2));
long double ta2=(v2-u)/am2;
R=(v2*v2)/ppaa;
tof=t+ta2+(0.78+R*1.414)/v2;
E=(e*fe*s+volt2*b*e)*(m2/m)+(1-b)*e*volt2;
file2<<i<<" "<<t<<" "<<tof*pow(10,6)<<" "<<z*pow(10,3)<<" "<<R<<" "<<endl;
break;}
if((z>=(x+10)*pow(10,-3))&& (z<(790+x)*pow(10,-3))) // find ToF & range analytically, if
particle is dissociating inside FD tube{
E=(e*fe*s+e*volt2)*(m2/m);
```

```
R=(u*u)/ppaa;
tof=t+(((790+x)*pow(10,-3)-z)+R*1.414)/u;
file2<<i<<" "<<t<<" "<<tof*pow(10,6)<<" "<<z*pow(10,3)<<" "<<R<<" "<<endl;
break;}
if (z>=(790+x)*pow(10,-3)) {// analytical calculation to find ToF & range analytically, if particle
is dissociating inside PPA
long double E0=m*u*u*0.5;
long double thalf=u/(1.414*ppa);
long double vxy2=2*(E0-m*ppa*y)/m;
long double vx=u/1.414;
long double vy2=vxy2-vx*vx;
vy=sqrt(vy2);
vxy=sqrt(vy*vy+vx*vx);
if (td>thalf)
vy=-vy;
theta=atan(vy/vx); // angle of projection of the particle to PPA
long double dis=sqrt(vxy*vxy*sin(theta)*sin(theta)+2*ppaa*y);
long double l=vxy*sin(theta);
long double diff=(l-dis)/ppaa;
long double add=(l+dis)/ppaa;
long double Td=td+diff;
long double Rd=0.707*u*Td;
long double Ta=td+add;
long double Ra=0.707*u*Ta;
if((Td>td)&&(Rd<0.523)&&(Rd>0)){
T=Td;
R=Rd;}
if((Ta>td)&&(Ra<0.523)&&(Ra>0)){
T=Ta;
R=Ra;}
tof=(t-td)+T; // final ToF of ion
file2<<i<<" "<<t<<" "<<tof*pow(10,6)<<" "<<z*pow(10,3)<<" "<<R<<" "<<endl;
break;}}}
base=rand()/scale;
fine=rand()/scale;
long double u5=base+fine/scale;
long double Range=R*1000-0.5+u5; // assigning uncertainty in range due to the finite size of
entrance slit of PPA
//long double Range=R*1000;
file1<<i<<" "<<tof*pow(10,6)<<" "<<Range<<" "<<u0<<" "<<x<<endl;}
file1.close();
file3.close();
file2.close();
return 0;}
```

# REFERENCES

1.  Leger A, Puget JL. Identification of the "unidentified IR emisson fetaures of interstelar dus? *Astron Astrophys*. 1984;137:L5-L8.

2.  Allamandola LJ, Tielens AGGM, Barker JR. Polycyclic aromatic hydrocarbons and the unidentified infrared emission bands - Auto exhaust along the Milky Way. *Astrophys J*. 1985;290:L25.

3.  Léger A, D'Hendecourt L, Defourneau D. Physics of IR emission by interstellar PAH molecules. *Astron Astrophys*. 1989;216:148-164.

4.  Berne O, Tielens AGGM. Formation of buckminsterfullerene (C60) in interstellar space. *Proc Natl Acad Sci*. 2012;109(2):401-406. doi:10.1073/pnas.1114207108

5.  Pollak E, Schlier C. Theory of unimolecular dissociation of small metastable molecules and ions as exemplified by H3+. *Acc Chem Res*. 1989;22:223-229. doi:10.1021/ar00162a005

6.  Safvan CP, Mathur D. On the determination of the lifetime of metastable doubly charged molecules by ion translational energy spectrometry: CO2+. *J Phys B At Mol Opt Phys*.

1993;26(22):L793-L798. doi:10.1088/0953-4075/26/22/004

7. Safvan CP, Mathur D. Lifetime measurements by ion translational energy spectrometry: metastable SH2+ ions. *J Phys B At Mol Opt Phys*. 1994;27(15). doi:10.1088/0953-4075/27/15/007

8. Rajput J, De S, Roy A, Safvan CP. Kinetic energy distributions and signature of target excitation in N2 fragmentation on collisions with Ar9+ ions. *Phys Rev A - At Mol Opt Phys*. 2006;74(3):1-7. doi:10.1103/PhysRevA.74.032701

9. Blanchet V, Lochbrunner S, Schmitt M, et al. Towards disentangling coupled electronic-vibrational dynamics in ultrafast non-adiabatic processes. *Faraday Discuss*. 2000;115:33-48.

10. Hückel E. Quantentheoretische Beitr~ge zum Problem der aromatischen und unges~ttigten Verbindungen. HI. *Z Phys*. Published online 1932:628–648.

11. Parr RG, Yang W. Density functional theory of atoms and molecules; Oxford University Press: New York. *Int J Quantum Chem*. Published online 1989.

12. M. J. Frisch, G. W. Trucks, H. B. Schlegel GES, M. A. Robb, J. R. Cheeseman, G. Scalmani, V. Barone BM, G. A. Petersson, H. Nakatsuji, M. Caricato, X. Li HPH, et al. Gaussian 09, Revision D.01; Gaussian, Inc.: Wallingford, CT, 2009. Published online 2009.

13. Robin MB. Higher Excited States of Polyatomic Molecules, (Academic Press, 1974);1:35-40.

14. Kaplan IG. Giant resonances in atoms, atomic clusters, fullerenes, condensed media, and nuclei. *Zeitschrift fur Phys D-Atoms Mol Clust*. 1997;40:375–380.

15. Baldwin GC, Klaiber GS. Photo-fission in heavy elements. *Phys Rev*. 1947;71:3–10. doi:10.1103/PhysRev.71.3

16. Zeppenfeld K. Anisotropic plasmon behaviour in graphite. *Phys Lett A*. 1967;25.4:335-336. doi:10.1016/0375-9601(67)90683-4

17. Bertsch GF, Bulgac A, Tomnek D, Wang Y. Collective plasmon excitations in C60 clusters. *Phys Rev Lett*. 1991;67:2690-2693. doi:10.1103/PhysRevLett.67.2690

18. Hertel I V., Steger H, De Vries J, et al. Giant plasmon excitation in free C60 and C70 molecules studied by photoionization. *Phys Rev Lett*. 1992;68:784. doi:10.1103/PhysRevLett.68.784

19. Hunsche S, Starczewski T, Huillier A, et al. Ionization and Fragmentation of C60 via Multiphoton-Multiplasmon Excitation. *Phys Rev Lett*. 1996;77:1-4.

20. Cheng S, Berry HG, Dunford RW, et al. Ionization and fragmentation of C60 by highly charged, high-energy xenon ions. *Phys Rev A - At Mol Opt Phys*. 1996;54(4):3182-3194. doi:10.1103/PhysRevA.54.3182

21. Kadhane U, Kelkar A, Misra D, Kumar A, Tribedi LC. Effect of giant plasmon excitations in single and double ionization of C60 in fast heavy-ion collisions. *Phys Rev A - At Mol Opt Phys*. 2007;75(4):1-4. doi:10.1103/PhysRevA.75.041201

22. Ling Y, Lifshitz C. Plasmon excitation in polycyclic aromatic hydrocarbons studied by

photoionization. *Chem Phys Lett*. 1996;257(5-6):587-591. doi:10.1016/0009-2614(96)00592-1

23. Mishra PM, Avaldi L, Bolognesi P, Prince KC, Richter R, Kadhane UR. Valence shell photoelectron spectroscopy of pyrene and fluorene: Photon energy dependence in the far-ultraviolet region. *J Phys Chem A*. 2014;118(17):3128-3135. doi:10.1021/jp502445d

24. Léger A, Boissel P, Desert FX, d'Hendecourt L. Phto-thermo-dissociation I- A general mechanism for destroying molecules. *Astron Astrophys*. 1989;213:351-359.

25. West B, Joblin C, Blanchet V, Bodi A, Sztáray B, Mayer PM. On the dissociation of the naphthalene radical cation: New iPEPICO and tandem mass spectrometry results. *J Phys Chem A*. 2012;116(45):10999-11007. doi:10.1021/jp3091705

26. Jolibois F, Klotz A, Gadéa FX, Joblin C. Hydrogen dissociation of naphthalene cations: a theoretical study. *Astron Astrophys*. 2005;444:629-634.

27. Gotkis Y, Oleinikova M, Naor M, Lifshitz C. Time-dependent mass spectra and breakdown graphs. 17. Naphthalene and phenanthrene. *J Phys Chem*. 1993;97(47):12282-12290. doi:10.1021/j100149a031

28. Dyakov YA, Ni CK, Lin SH, Lee YT, Mebel AM. Ab initio and RRKM study of photodissociation of azulene cation. *Phys Chem Chem Phys*. 2006;8(12):1404-1415. doi:10.1039/b516437k

29. Van-Oanh NT, Désesquelles P, Douin S, Bréchignac P. Photofragmentation of the fluorene cation: I. new experimental procedure using sequential multiphoton absorption. *J Phys*

*Chem A*. 2006;110(17):5592-5598. doi:10.1021/jp057164s

30.     Van-Oanh NT, Désesquelles P, Bréchignac P. Photofragmentation of the fluorene cation: II. Determination of the H-loss energy-dependent rate constant. *J Phys Chem A*. 2006;110(17):5599-5606. doi:10.1021/jp057168x

31.     Cui W, Hadas B, Cao B, Lifshitz C. Time-Resolved Photodissociation (TRPD) of the Naphthalene and Azulene Cations in an Ion Trap/Reflectron. *J Phys Chem A*. 2000;104(27). doi:10.1021/jp0022813

32.     Ullrich J, Moshammer R, Dörner R, et al. Recoil-ion momentum spectroscopy. *J Phys B At Mol Opt Phys*. 1997;30:2917.

33.     Dörner R, Mergel V, Jagutzki O, et al. Cold target recoil ion momentum spectroscopy: a 'momentum microscope'to view atomic collision dynamics. *Phys Rep*. 2000;330:95-192.

34.     Wiley WC, McLaren IH. Time-of-flight mass spectrometer with improved resolution. *Rev Sci Instrum*. 1955;26(12):1150-1157. doi:10.1063/1.1715212

35.     Neusser HJ. Multi-photon mass spectrometery and unimolecular ion decay. *Int J Mass Spectrom Ion Process*. 1987;79:141-181.

36.     Leprè V, Lucas B, Barat M, et al. Comprehensive characterization of the photodissociation pathways of protonated tryptophan. *J Chem Phys*. 2007;127(13). doi:10.1063/1.2770458

37.     Lepère V, Lucas B, Barat M, et al. Characterization of neutral fragments issued from the photodissociation of protonated tryptophane. *Phys Chem Chem Phys*. 2007;9(39):5330-5334. doi:10.1039/b708814k

38. Harrower GA. Measurement of electron energies by deflection in a uniform electric field. *Rev Sci Instrum*. 1955;26(9):850-854. doi:10.1063/1.1715326

39. Farnell CC, Farnell CC, Farnell SC, Williams JD. *Electrostatic Analyzers with Application to Electric Propulsion Testing Proceedings of the 33rd International Electric Propulsion Conference. 2013;1-48.*

40. DLD2 (June 2014). Molecular Photonics Group. http://www.chem.queensu. ca/people/faculty/Stolow/Research/Facilities.html.

41. DLD1 (June 2014). Microchannel plate (MCP) detectors. http://www.atom. uni-frankfurt.de/research/coltrims/mcp/.

42. David J. Griffiths. *Griffiths, D. J. (1962).Introduction to Electrodynamics New Jersey: Prentice Hall.*

43. De S, Ghosh PN, Roy A, Safvan CP. A setup for probing ion-molecule collision dynamics. *Nucl Instruments Methods Phys Res Sect B Beam Interact with Mater Atoms*. 2006;243(2):435-441. doi:10.1016/j.nimb.2005.09.004

44. Kumar A, Rajput J, Sairam T, Jana MR, Nair L, Safvan CP. Setup for measuring angular anisotropies in slow ion-molecule collisions. *Int J Mass Spectrom*. 2014;374:44-48. doi:10.1016/j.ijms.2014.09.018

45. Geller R. *Electron Cyclotron Resonance Ion Sources and ECR Plasmas.*; 2018. doi:10.1201/9780203758663

46. Laserdatasheet().http://www.ekspla.com/wp-content/uploads/2013/06/nt242p-

seriesnanosecond-tunable-dpss-lasers.pdf.

47. Mishra PM, Rajput J, Safvan CP, Vig S, Kadhane U. Electron emission and electron transfer processes in proton-naphthalene collisions at intermediate velocities. *Phys Rev A - At Mol Opt Phys*. 2013;88(5). doi:10.1103/PhysRevA.88.052707

48. Mishra PM, Rajput J, Safvan CP, Vig S, Kadhane U. Velocity dependence of fragmentation yields in proton-naphthalene collision and comparison with electronic energy loss calculation. *J Phys B At Mol Opt Phys*. 2014;47(8):085202 (9pp). doi:10.1088/0953-4075/47/8/085202

49. Goffe V. Cross sections for ionization of water vapor by 7-4000-keV protons. *Phys Rev A*. 1985;31(1):1-3.

50. Krems M, Zirbel J, Thomason M, DuBois RD. Channel electron multiplier and channelplate efficiencies for detecting positive ions. *Rev Sci Instrum*. 2005;76(9):093305. doi:10.1063/1.2052052

51. West B, Rodriguez Castillo S, Sit A, et al. Unimolecular reaction energies for polycyclic aromatic hydrocarbon ions. *Phys Chem Chem Phys*. 2018;20(10):7195-7205. doi:10.1039/c7cp07369k

52. Mishra PM, Kadhane U. Monte Carlo simulation of electronic energy loss for proton impact on nucleobases. *Nucl Instruments Methods Phys Res Sect B Beam Interact with Mater Atoms*. 2014;336:12-18. doi:10.1016/j.nimb.2014.06.007

53. Kabachnik NM, Kondratyev VN, Roller-Lutz Z, Lutz HO. Multiple ionization of atoms

and molecules in collisions with fast ions: Ion-atom collisions. *Phys Rev A - At Mol Opt Phys*. 1997;56(4):2848-2854. doi:10.1103/PhysRevA.56.2848

54. Wolff W, Luna H, Sigaud L, Tavares AC, Montenegro EC. Absolute total and partial dissociative cross sections of pyrimidine at electron and proton intermediate impact velocities. *J Chem Phys*. 2015;140(October 2013):064309. doi:10.1063/1.4864322

55. Postma J, Bari S, Hoekstra R, Tielens AGGM. Ionization and fragmentation of anthracene upon interaction with kev protons and α particles. *Astrophys J*. 2010;708:435-444. doi:10.1088/0004-637X/708/1/435

56. Tsuchida H, Itoh A, Nakai Y, Miyabe K, Imanishi N. Cross sections for ionization and fragmentation of C60 by fast H+ impact. *J Phys B At Mol Opt Phys*. 1998;31(24):5383-5391. doi:10.1088/0953-4075/31/24/019

57. Jochims HW, Riihl E, Baumg H, Tobita S, Leach S. VUV peaks in absorption spectra and photoion yield curves of polycyclic aromatic hydrocarbons and related compounds. 1997;168:35-53.

58. Koster G, Martin JML, Lifshitz C. Energetics of the naphthalene/azulene monocation isomerization: Density functional and coupled cluster calculations. *J Chem Soc Perkin Trans 2*. 1999;(11):2383-2387. doi:10.1039/a904129j

59. Jochims HW, Rasekh H, Rühl E, Baumgärtel H, Leach S. The photofragmentation of naphthalene and azulene monocations in the energy range 7-22 eV. *Chem Phys*. 1992;168(1):159-184. doi:10.1016/0301-0104(92)80118-F

60. Scott LT, Kirms MA. Azulene Thermal Rearrangements.13C-Labeling Studies of Automerization and Isomerization to Naphthalene. *J Am Chem Soc*. 1981;103:5875-5879. doi:10.1021/ja00409a042

61. Michael J. S. Dewar, Kenneth M. Merz J. Potential Energy Surface: The Azulene-to-Naphthalene Rearrangement. *J Am Chem Soc*. 1986;(108):5142-5145.

62. Tobita S, Leach S, Jochims HW, Rühl E, Illenberger E, Baumgärtel H. Single-and double-ionization potentials of polycyclic aromatic hydrocarbons and fullerenes by photon and electron impact. *Can J Phys*. 1994;72:1060-1069.

63. Ling Y, Lifshitz C. Time-dependent mass spectra and breakdown graphs. 21. C14H10 isomers. *J Phys Chem A*. 1998;102(4):708-716. doi:10.1021/jp973167w

64. Jackson JD. *Classical Electrodynamics*. Wiley, New York; 1975.

65. Holm AIS, Johansson HAB, Cederquist H, Zettergren H. Dissociation and multiple ionization energies for five polycyclic aromatic hydrocarbon molecules. *J Chem Phys*. 2011;134(4). doi:10.1063/1.3541252

66. Alagia M, Candori P, Falcinelli S, et al. Dissociative double photoionization of benzene molecules in the 26-33 eV energy range. *Phys Chem Chem Phys*. 2011;13(18):8245-8250. doi:10.1039/c0cp02678f

67. Mebel AM, Landera A, Kaiser RI. Formation Mechanisms of Naphthalene and Indene: From the Interstellar Medium to Combustion Flames. *J Phys Chem A*. 2017;121(5):901-926. doi:10.1021/acs.jpca.6b09735

68. Zhao L, Kaiser RI, Lu W, et al. Molecular mass growth through ring expansion in polycyclic aromatic hydrocarbons via radical–radical reactions. *Nat Commun*. 2019;10(1):1-7. doi:10.1038/s41467-019-11652-5

69. Laskin J, Lifshitz C. Kinetic energy release distributions in mass spectrometry. *J Mass Spectrom*. 2001;36(5):459-478. doi:10.1002/jms.164

70. Leach S, Eland JHD, Price SD. Formation and dissociation of dications of naphthalene, azulene, and related heterocyclic compounds. *J Phys Chem*. 1989;93(22):7575-7583. doi:10.1021/j100359a013

71. Martínez JI, Alonso JA. Hydrogen quenches the size effects in carbon clusters. *Phys Chem Chem Phys*. 2019;211:10402-10410. doi:10.1039/c9cp01114e

72. Kingston RG, Guilhaus M, Brenton AG, Beynon JH. Multiple ionization, charge separation and charge stripping reactions involving polycyclic aromatic compounds. *Org Mass Spectrom*. 1985;20(6):406-412. doi:10.1002/oms.1210200605

73. Reitsma G, Zettergren H, Boschman L, Bodewits E, Hoekstra R, Schlathölter T. Ion-polycyclic aromatic hydrocarbon collisions: Kinetic energy releases for specific fragmentation channels. *J Phys B At Mol Opt Phys*. 2013;46(24). doi:10.1088/0953-4075/46/24/245201

74. Steglich M, Maity S, Maier JP. Visible Absorptions of Potential Diffuse Ism Hydrocarbons: C9H9 and C9H5 Radicals. *Astrophys J*. 2016;830(2):145. doi:10.3847/0004-637x/830/2/145

75. Ortega C, Kono N, Ji M, et al. Dissociation rate, fluorescence and Infrared radiative cooling rates of Naphthalene studied in electrostatic storage Miniring. *J Phys Conf Ser*. 2015;635(3). doi:10.1088/1742-6596/635/3/032051

76. Kadhane U, Andersen JU, Bonderup E, et al. Near-infrared photoabsorption by dianions in a storage ring. *J Chem Phys*. 2007;014301:1-8. doi:10.1063/1.3149775

77. Hansen K, Andersen JU, Hvelplund P, Møller SP, Pedersen U V., Petrunin V V. Observation of a 1/t Decay Law for Hot Clusters and Molecules in a Storage Ring. *Phys Rev Lett*. 2001;87(12):1-4. doi:10.1103/PhysRevLett.87.123401

78. Bouwman J, Sztáray B, Oomens J, Hemberger P, Bodi A. Dissociative photoionization of quinoline and isoquinoline. *J Phys Chem A*. 2015;119:1127-1136. doi:10.1021/jp5121993

79. Chen L, Brédy R, Bernard J, Montagne G, Allouche AR, Martin S. Fragmentation of singly charged adenine induced by neutral fluorine beam impact at 3 keV. *J Chem Phys*. 2011;135(11):114309. doi:10.1063/1.3621713

80. Martin S, Chen L, Denis A, Bredy R, Bernard J. Excitation and fragmentation of C 60 r+(r= 3–9) in Xe 3 0+− C 60 collisions. *Phys Rev A*. 2000;62:1-5.

81. KASHA M. Characterization of electronic transitions in complex molecules. *Discuss Faraday Soc*. 1950;9:14.

82. Fujii M, Ebata T, Naohiko M, Ito M. Electronic spectra of jet cooled azulene. *Chem Phys*. 1983;77:191-200.

83. Damm M, Deckert F, Hippler H, Troe J. Isomerization and colllsional deactivation of

highly vlbrationally excited azulene molecules after UV excltatlon at 248 and 193 nm. *J Phys Chem*. 1991;95:2005-2009.

84. Kuthirummal N, Weber PM. Structure sensitive photoionization via Rydberg levels. *J Mol Struct*. 2006;787(1-3):163-166. doi:10.1016/j.molstruc.2005.10.043

85. Weber PM, Thantu N. Photoionization via transient states. A coherent probe of molecular eigenstates. *Chem Phys Lett*. 1992;197(6):556-561. doi:10.1016/0009-2614(92)85815-R

86. Blanchet V, Raffael K, Turri G, et al. Time-dependent photoionization of azulene: Competition between ionization and relaxation in highly excited states. *J Chem Phys*. 2008;128(16):164318. doi:10.1063/1.2913167

87. Piecuch P, Hansen JA, Staedter D, Faure S, Blanchet V. Communication: Existence of the doubly excited state that mediates the photoionization of azulene. *J Chem Phys*. 2013;138(20):201102. doi:10.1063/1.4808014

88. Solano EA, Mayer PM. A complete map of the ion chemistry of the naphthalene radical cation ? DFT and RRKM modeling of a complex potential energy surface. *J Chem Phys*. 2015;143:104305. doi:10.1063/1.4930000

89. Cockett MCR, Ozeki H, Okuyama K, Kimura K. Vibronic coupling in the ground cationic state of naphthalene: A laser threshold photoelectron [zero kinetic energy (ZEKE)-photoelectron] spectroscopic study. *J Chem Phys*. 1993;98(10):7763-7772. doi:10.1063/1.464584

90. Tanaka D, Sato S, Kimura K. ZEKE electron spectroscopy of azulene and azulene – argon.

*Chem Phys*. 1998;239(June):437-445.

91.  Smith JM, Lakshminarayan C, Knee JL. Picosecond measurements of vibrational dynamics using pump-probe laser photoelectron spectroscopy. *J Chem Phys*. 1990;93(6):4475-4476. doi:10.1063/1.458731

92.  Zhang J, Han F, Pei L, Kong W, Li A. Far-Infrared Spectroscopy of Cationic Polycyclic Aromatic Hydrocarbons: Zero Kinetic Energy Photoelectron Spectroscopy of Pentacene Vaporized from Laser Desorption. *Astrophys J*. 2010;715:485-492. doi:10.1088/0004-637X/715/1/485

93.  Poveda JC, Guerrero A, Álvarez I, Cisneros C. Journal of Photochemistry and Photobiology A : Chemistry Multiphoton ionization and dissociation of naphthalene at 266 , 355 , and 532 nm. *"Journal Photochem Photobiol A Chem*. 2010;215(2-3):140-146. doi:10.1016/j.jphotochem.2010.07.031

94.  Szczepanski J, Banisaukas J, Vala M, et al. Vibrational and Electronic Spectroscopy of the Fluorene Cation. *J Phys Chem*. 2002;106:63-73.

# LIST OF PUBLICATIONS

1. **Vinitha. M. V**., et al. "Plasmon excitation and subsequent isomerization dynamics in naphthalene and azulene under fast proton interaction." J. Chem. Phys. 149, 194303 (2018).

2. **Vinitha. M. V.,** et al. "High resolution energy-time of flight spectrometer: Dehydrogenation of fluorene cation as case study", Rev. Sci. Instrum. 90, 103304 (2019).

3. **Vinitha. M. V.,** et al. "Isomerization and dehydrogenation of highly vibrationally excited azulene$^+$ produced via $S_2$ vibrational manifold", Chem .Phys. Lett. 745**,** 137250 (2020).

4. **Vinitha. M. V.,** et al. "Production of PAH cations with narrow internal energy distribution using single nanosecond pulsed laser", accepted for publications Eur. Phys. J. D.

5. **Vinitha. M. V.,** et al. "plasmon assisted isomerization in naphthalene and azulene", Journal of Physics: Conference Series, 1412, 152063 (2020).

6. **Vinitha. M. V.** and U. Kadhane. "Energy selective ToF spectrometer to study low energy dissociation channels of PAHs", Journal of Physics: Conference Series, 1412 (21), 212001 (2020)

7. P. K. Najeeb, T. Sairam, **M. V. Vinitha**, A. Kala, S. Vig, P. Bhatt, C. P. Safvan, U. kadhane, "Exploring metastable decay dynamics of polycyclic aromatic nitrogen containing hydrocarbons upon HCN evaporation" Journal of Physics: Conference Series, 875, 122004 (2017)

8. **Vinitha. M. V.,** et al. "Formation of carbon cluster ions by elimination of $H^+$ or $CH_n^+$ from multiply charged naphthalene and azulene ions", under review, Mol.Astrophys.